

# **Avalanche Photodiodes for the CATSAT Gamma-ray Burst Mission**

by

**David William Fletcher-Holmes**

Thesis submitted to the University of Leicester for the degree of Doctor of Philosophy.

October 2000

X-ray Astronomy Group  
Department of Physics and Astronomy  
University of Leicester

UMI Number: U485517

All rights reserved

INFORMATION TO ALL USERS

The quality of this reproduction is dependent upon the quality of the copy submitted.

In the unlikely event that the author did not send a complete manuscript and there are missing pages, these will be noted. Also, if material had to be removed, a note will indicate the deletion.



UMI U485517

Published by ProQuest LLC 2013. Copyright in the Dissertation held by the Author.  
Microform Edition © ProQuest LLC.

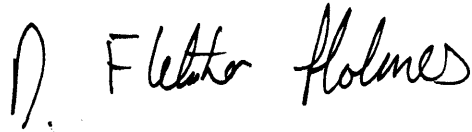
All rights reserved. This work is protected against  
unauthorized copying under Title 17, United States Code.



ProQuest LLC  
789 East Eisenhower Parkway  
P.O. Box 1346  
Ann Arbor, MI 48106-1346

# Declaration

I hereby declare that no part of this thesis has been submitted to this or any other University as part of the requirements for a higher degree. The work described here was conducted by the undersigned except for the contributions of colleagues indicated in the text.

A handwritten signature in black ink, reading "D. Fletcher Holmes". The signature is written in a cursive style with a large initial "D" and a period.

David W. Fletcher-Holmes

October 2000

# **Dedication**

To Alan, Mary, Graham, Tillie, Bill, Emily & Cyril  
all of whose handwriting may be found herein

# **Acknowledgements**

I would like to acknowledge the assistance and guidance of my supervisor, Martin Barstow, and the technical skill of my immediate superior Chris Whitford. Further thanks go to Alan Wells for helpful discussion and David Watson for a wealth of day to day support. Thanks also to Stan Cowley for timely moral support.

Much other input was provided by (in no order): Tony Abbey, Adam Keay, Alex Short, Jason Page, Harold Chapman, David Vernon, John Spragg, Jim Pearson, Steve Sembay, Dick Farrell and Mike Denby.

I would like to thank all my friends in the Space Research Centre and the Dept. of Physics in Leicester and in Morse Hall and Babcock Hall in New Hampshire for their company, good humour, coffer-time anecdotes and PC gaming.

I should especially like to thank all those who have been my housemates in Leicester these past seven years: you have made all the difference.

I acknowledge the financial support of the CATSAT programme.

**David W Fletcher-Holmes**

## **Avalanche Photodiodes for the CATSAT Gamma-ray Burst Mission**

### **Abstract**

This thesis firstly describes efforts to characterise large-area, high-gain, Avalanche Photodiodes (APDs), manufactured by Radiation Monitoring Devices (RMD) inc. of Massachusetts. These are relatively new devices in the field of X-ray spectroscopy and the research presented here attempts to increase our understanding of their behaviour as X-ray detectors and their underlying internal physical processes. Models are suggested for Quantum Detection Efficiency and for Photopeak Fraction in these devices. Measurements of these properties as a function of energy constrain the models, revealing new information about the internal structure of APDs and providing powerful predictive tools for detector response. The intrinsic silicon dead layer of a typical device is found to be 2  $\mu\text{m}$  thick, whilst the sensing layer is 21  $\mu\text{m}$  thick.

Secondly, this thesis provides detailed accounts of how the new tools mentioned above have been utilised to characterise an ensemble of APDs and how that characterisation has been used to simulate the behaviour of an APD-based astrophysical instrument: CATSAT's Soft X-ray Spectrometer (SXR). This work includes simulated SXR observations of the diffuse soft X-ray background, the crab nebula and CATSAT's target objects: Gamma-ray Bursts. The results of these simulations are presented, leading to an analysis of CATSAT's ability to meet its scientific objectives. It is estimated that the SXR will observe approximately 7 bursts per year above the five-sigma significance level. In approximately half of these cases, it should be possible to discriminate between the hypothesis that there is an absorbing hydrogen column of density  $1 \times 10^{22} \text{ cm}^{-2}$  and the hypothesis that there is no column.

# Contents

<b>Chapter 1: Gamma-ray Bursts</b>	<b>1</b>
1.1 From Vela to Compton	2
1.2 From Compton to SAX	5
1.3 The Current Situation	10
 <b>Chapter 2: CATSAT and the Soft X-ray Spectrometer</b>	 <b>14</b>
2.1 CATSAT's Evolution	15
2.2 Scientific Payload	18
2.2.1 The Soft X-ray Spectrometer	18
2.2.2 The Directional Gamma-ray Spectrometer	23
2.2.3 The Hard X-ray Spectrometer	24
2.2.4 The X-ray Albedo Polarimeter	24
2.3 Mission	25
 <b>Chapter 3: The Avalanche Photodiode</b>	 <b>26</b>
3.1 The APD as a Semiconductor Device	27
3.1.1 Internal Structure	27
3.1.2 Storage and Handling	28
3.2 The APD as an X-ray Detector	28
3.2.1 Basic Detector Mechanisms	28
3.2.2 Signal Multiplication and McIntyre Theory	30
3.3 X-ray Calibration Equipment	35
3.3.1 Vacuum and Cooling	35
3.3.2 X-ray Sources	37
3.3.3 Gas Proportional Counter Reference Detector	39
3.4 APD Aluminising	39

## Contents

3.5 The Detection Efficiency of APDs	44
3.6 The "Shelf" in APD Pulse Height Distributions	49
3.7 Asymmetric peaks in APD Pulse Height Distributions	56
<b>Chapter 4: Calibration and Assembly</b>	<b>61</b>
4.1 APD Screening	61
4.2 APD Grouping	62
4.3 Aluminising and Assembly	64
4.4 Calibration	64
4.4.1 Asymmetry and Calibration	64
<b>Chapter 5: Calibration Results</b>	<b>77</b>
<b>Chapter 6: SXR Performance</b>	<b>98</b>
6.1 Response Matrices	98
6.2 Simulation of X-ray Background	99
6.3 A Simulated Observation of the Crab Nebula	101
6.4 Simulated Observations of Gamma-Ray Bursts	103
6.5 Fitting Models to Simulated Observations of Gamma-ray Bursts	106
<b>Chapter 7: Conclusions</b>	<b>110</b>
7.1 New Knowledge about APDs	110
7.2 The Likely Performance of the SXR Instrument	112
<b>Bibliography</b>	<b>113-122</b>
<b>Appendix A: Calibration Procedures for SXR Panels</b>	<b>(19 pages)</b>

## 1.1 From Vela to Compton

In the late 1960s, the US government launched the Vela (Spanish for "Vanguard") satellites to confirm Soviet compliance with the nuclear test ban treaty of 1963. These satellites carried

# Chapter 1

detectors sensitive to the energy range 0.2 MeV to 1 MeV. Alexander Levan and others (1973) searched the data from these satellites for high-energy emission from supernovae (Colgate 1982), but instead found distinct pulses of intense Gamma-ray flux unassociated with known SN. A natural explanation was suggested from the difference in arrival times at each of the satellites. After ruling out terrestrial atmospheric origins for these

# Gamma-ray Bursts

bursts in a famous paper "Observations of Gamma-ray Bursts of Cosmic Origin" (Eichler et al. 1973).

The 20 bursts Vela observed all had durations between 0.02 and 0.26 seconds. Some

Few astronomical phenomena can claim to be as enigmatic or intriguing as Gamma-ray Bursts (GRBs). The 30 year long study of this field has been filled with controversy and surprises. This chapter charts the history of the study of GRBs culminating with a review of the current "standard" models.

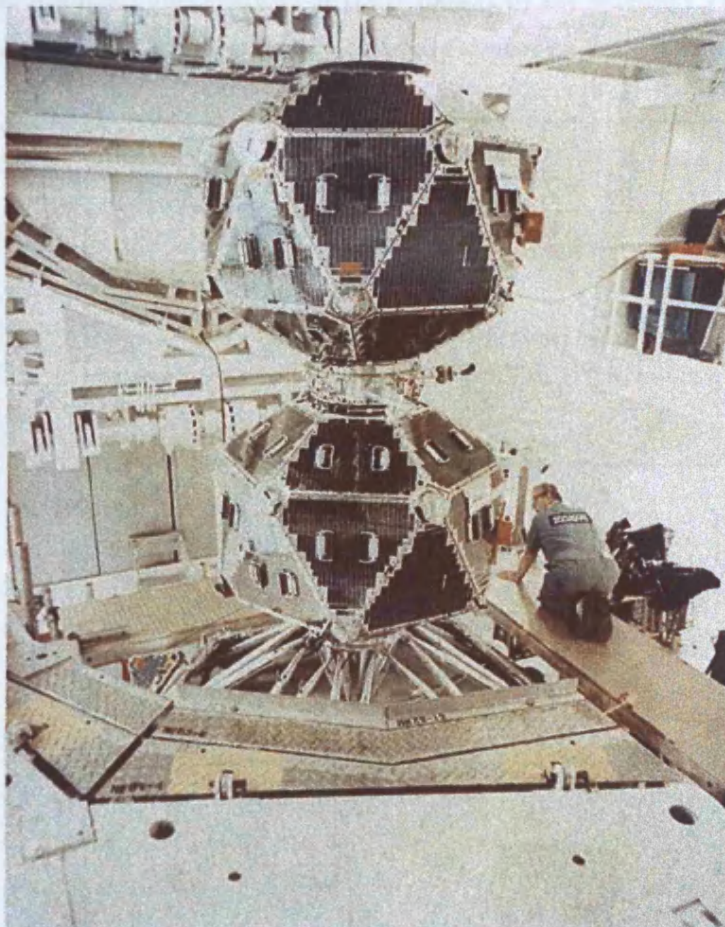


Figure 1.1: Vela 5B

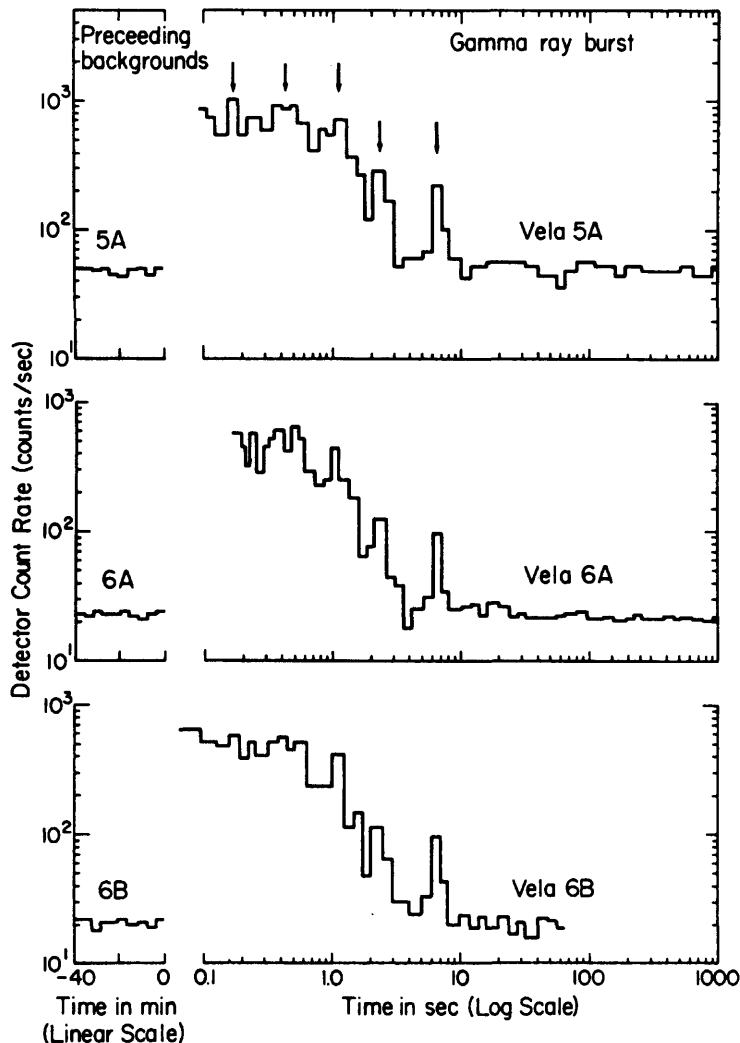


## 1.1 From Vela to Compton

In the late 1960's the US government launched the Vela (Spanish for "Watchman") satellites to confirm Soviet compliance with the nuclear test ban treaty of 1963. These satellites carried scintillation detectors sensitive to the energy range 0.2 MeV to 1 MeV. Klebesadel, Strong and Olsen (1973) searched the data from these instruments for high-energy emission from supernovae (Colgate 1968), but instead found sixteen occurrences of intense Gamma-ray flux uncorrelated with known SN. Positional information was calculated from the difference in arrival times at each of the satellites. After ruling out terrestrial/lunar/solar origins for these events, they published their results in the now famous paper "Observations of Gamma-ray Bursts of Cosmic Origin" (Klebesadel et al. 1973).

The 16 bursts Vela observed all had durations between one second and thirty seconds. Some bursts showed a time structure with several peaks whilst others did not. The Vela instruments were crude by modern standards and offered no spectral resolution. Observations of the burst of August 22<sup>nd</sup> 1970 are shown below in figure 1.2, as an example.

**Figure 1.2: Simultaneous observations of GRB 700822 by the satellites Vela 5A, Vela 6A and Vela 6B. Background counting rates are shown on the left of the charts.**



The astrophysical community was energised by this new phenomenon and a great variety of theoretical models were produced as possible explanations. In his review, Ruderman (1975) identified many sub-classes: supernovae shocks (Bisnovatyi-Kogan et al. 1974; Colgate 1974), neutron star formation (Ramaty et al. 1973), starquakes and other "glitches" (Bisnovatyi-Kogan et al. 1974; Pacini et al. 1974; Pringle et al. 1974), neutron stars in close binaries (Lamb et al. 1973), black holes in binaries (Strong et al. ; Lamb et al. 1973), novae (Hoyle et al. 1974), white holes (Narlikar et al. 1974), flares on "normal" stars (Anzer et al. 1974; Brecher et al. 1974), flares on white dwarfs (Stekker et al. 1973; Channugam 1974), flares on neutron stars (Coppi et al. 1973; Pacini et al. 1974), flares in close binaries (Lamb et al. 1973), nuclear explosions on white dwarfs (Hoyle et al. 1974), comets on neutron stars (Harwit et al. 1973), Jupiter (Apparo 1973), antimatter on conventional stars (Sofia et al. 1974), relativistic dust (Grindlay et al. 1974), instabilities near rotating charged black holes (Ruffini 1975), instabilities in pulsar magnetospheres (Coppi et al. 1973) and "ghouls" (Zwicky 1974). All of these models were based on observations of GRBs made by instruments not specifically designed for GRB astronomy, the so-called "first generation". These observations were crude and provided few constraints for theorists.

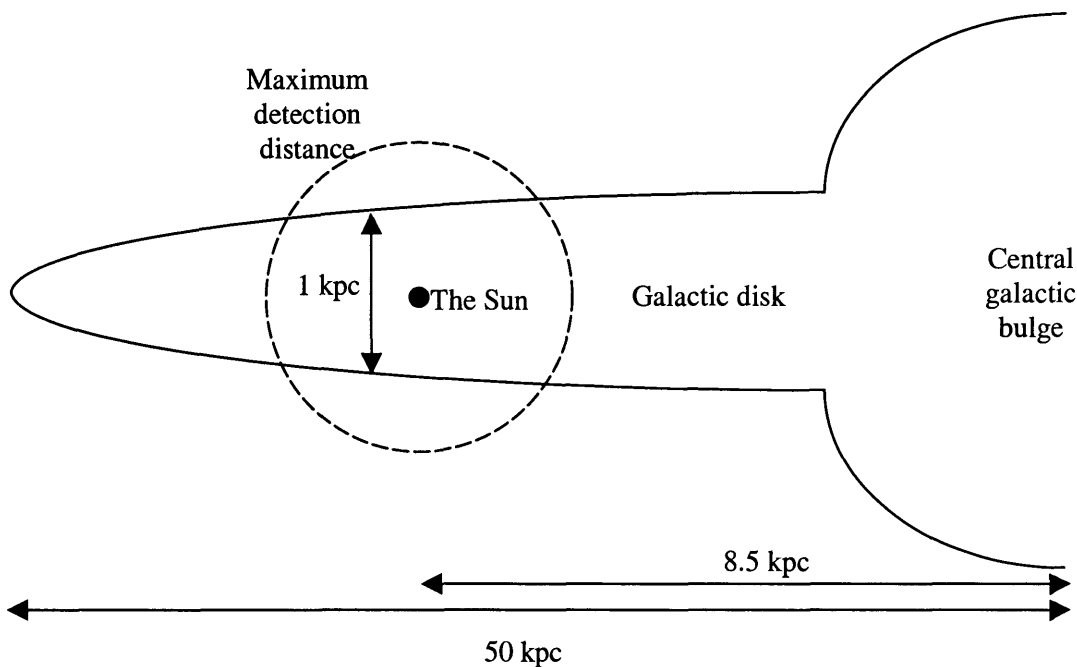
The first dedicated GRB instrumentation was flown on board the Helios 2 satellite in 1976. This was followed by instrumentation on the Pioneer Venus Orbiter (PVO), ISEE-3, Venera 11 & 12 and Prognost 7 in 1978 and SMM in 1980. These instruments were the "second generation" (Hurley 1980). Detection rates for GRBs went up, as did the quality of the data, yielding several important results:

1. Many, though not all, events showed complex time structure even on the smallest time-scales available. Many investigators used this to determine a characteristic source dimension,  $d$ , where  $d \leq c\Delta t$ ,  $c$  is the speed of light and  $t$  is the characteristic timescale of the features in the burst. This would indicate a very compact source (Harding 1991).
2. Burst spectra could generally be described by a powerlaw model, with indices between -1 and -3 and a steepening around 200 keV.
3. An analysis of the burst intensity distribution (the so-called logN-logS curve) showed a relative lack of faint events (Hurley 1983). This could possibly be explained as an instrumental effect, as evidence for a galactic disk population of objects sampled beyond their scale height (Vedrenne 1981) or as evidence of a cosmological population of objects, sampled beyond the distance for which the universe may be considered to be Euclidean.
4. Burst locations appeared to be isotropically distributed on the sky, with no evidence of concentrations in the directions of the galactic centre, the galactic plane or M31.

5. Several satellites (ISEE-3, Venera-11-14, PVO) occasionally observed emission lines, around 420 keV, which could be interpreted as electron-positron annihilation lines with red-shifts appropriate to a galactic neutron star origin (Verter 1982). However, SMM failed to observe any such lines (Lamb 1988).
6. Venera-11 & 12, SMM, HEAO-1 and Ginga occasionally observed what appeared to be cyclotron absorption lines below 65 keV (Cline 1981; Murakami et al. 1988), which would also be consistent with a highly magnetised ( $>10^{12}$  Gauss) neutron star (Lamb 1984).

Points 1, 3, 5, and 6 were taken collectively to indicate that Gamma-ray Bursts originated on a galactic disk population of highly magnetised neutron stars. This became known as the Terra-Gauss Neutron Star paradigm or TGNS. Cosmological distance scales were excluded principally because the energy requirements of such a distribution seemed impossible to meet. The confidence of the astrophysical community became very great (Woosley 1984) and many models based on the TGNS were developed (Hurley 1989). However, there were some problems. The dearth of faint GRBs was taken to indicate that GRB progenitors inhabited the galactic disk and that the available instruments were probing the population beyond its scale height (see figure 1.3).

**Figure 1.3: The consequences of a galactic disk population of GRB progenitors.**



But if this was the case, then the spatial distribution of Gamma-ray Bursts would be expected to be anisotropic: there would be a tendency for bursts to lie in the disk of the galaxy. At first, the evidence for isotropy was statistically questionable, but as more GRBs were located, the evidence became more and more compelling. In order to explain the observed isotropy, the distance scale of GRBs had to be extended, first to a thick disk (Vedrenne et al. 1983), then to a halo (Cline 1983) and finally to an extended halo (Hurley 1989).

In order to discriminate between these models, it was necessary to design a new instrument, an instrument with greater sensitivity to faint bursts and with a large field of view (Higdon et al. 1990). These attributes would allow isotropy to be tested not only for the set of all GRBs, but also for faint bursts in particular. Furthermore, a more sensitive instrument would reveal whether or not the observed dearth of faint bursts was simply a reflection of failings in earlier experiments.

## 1.2 From Compton to SAX

The Compton Gamma-ray Observatory (CGRO) was launched by the space shuttle Atlantis on the 5<sup>th</sup> of April 1991. CGRO was the second of NASA's great observatories. The four instruments that made up the scientific payload were the Burst and Transient Source Experiment (BATSE), the Oriented Scintillation Spectrometer Experiment (OSSE), the Imaging Compton Telescope (COMPTEL) and the Energetic Gamma Ray Experiment Telescope (EGRET) (Bunner 1999). The properties of these instruments are summarised in table 1 and their locations on the CGRO spacecraft are shown in figure 1.4.

**Table 1: The principle instruments on CGRO and their characteristics**

Instrument	Description	Observations
BATSE	8 x NaI/PMT combination covering whole sky. Energy range: 20keV to 600 keV.	GRB all sky monitor
OSSE	4 x NaI/PMT combination. Energy range: 50 keV to 10 MeV.	Nuclear lines in solar flares. Radioactive decay in SNR. $e^-p^+$ annihilation signature in galactic centre.
COMPTEL	A layer of NaI/PMT instruments below a layer of NE 213A/PMT instruments. Energy range: 1MeV to 30 MeV.	AGN, SNR & molecular clouds
EGRET	Multi-level, thin plate, gas filled spark chamber & NaI/PMT. Energy range: 20 MeV to 30 GeV	Pulsars, SNRs, AGN & quasars

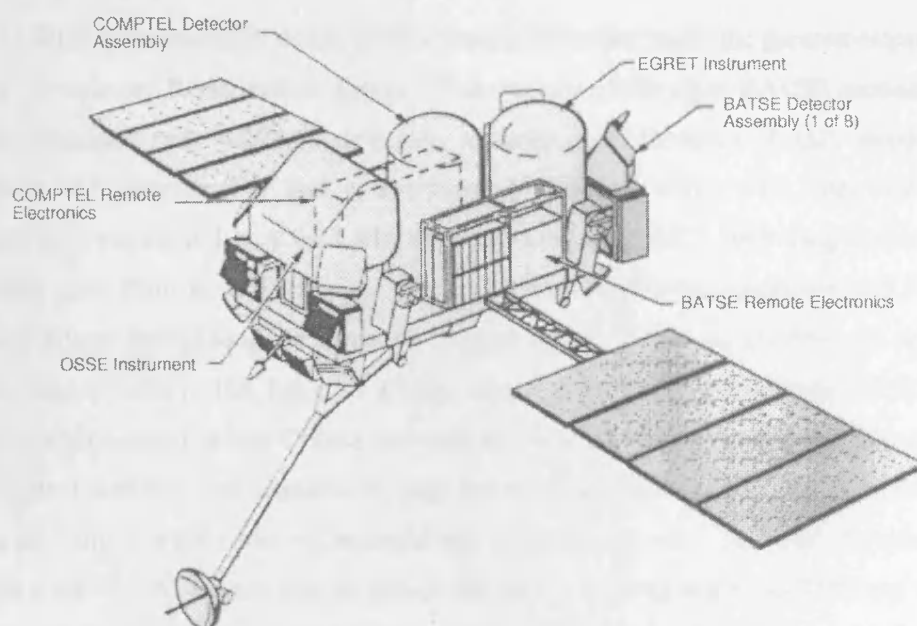


**Figure 1.4: The Compton Gamma-Ray Observatory (CGRO)**

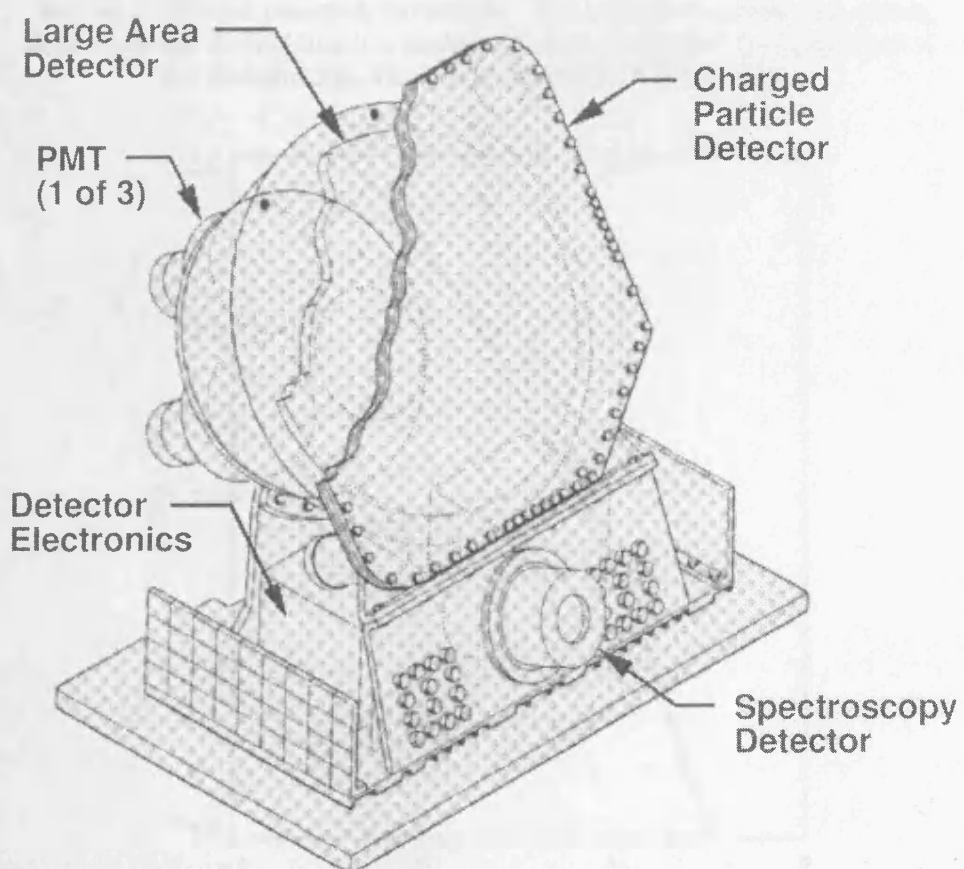


**Figure 1.5: A single BATSE module**

Of all CGRO's instruments, it was BATSE (Horack 1991) that made the greatest impact in the field of Gamma-ray Burst studies. Figure 1.5 shows one of the eight BATSE modules. Each module contained two NaI/PMT detectors: a Large Area Detector (LAD), designed for sensitivity and directionality and a Spectroscopy Detector (SD), with improved energy coverage and resolution. It was the LADs that were used as CGRO's GRB trigger instruments. The count rate from each LAD was monitored for statistically significant ( $>5.5$  sigma) increases above background on three timescales: 64ms, 256ms & 1024ms. At least two modules had to achieve this limit for a burst trigger to occur. Approximately 3000 BATSE burst triggers occurred before CGRO was shut down in 2000. When a burst trigger occurred BATSE went into fast data acquisition mode and remained there for as long as 105 minutes. During this time a wide variety of spectral and temporal data were gathered (Bunner 1999). CGRO's BATSE LADs were able to detect and locate approximately one GRB per day. As the statistics increased it became apparent that the observed distribution of bursts was still isotropic and that there was still a dearth of faint bursts (Hartmann 1994). Figure 1.6 shows a BATSE logN-logS plot and figure 1.7 shows a sky map of burst locations.

**Figure 1.6: The integral-number-peak-flux relation for 1103 BATSE GRBs.  $N$  is the number of bursts whose peak flux  $S_{\text{peak}}$  between 50 and 300 keV on a 1024 ms timescale exceeds  $S_1$ . The solid curve shows the actual data while the dashed line is a backward extrapolation of the bright end of the distribution. There is a clear lack of faint bursts.**

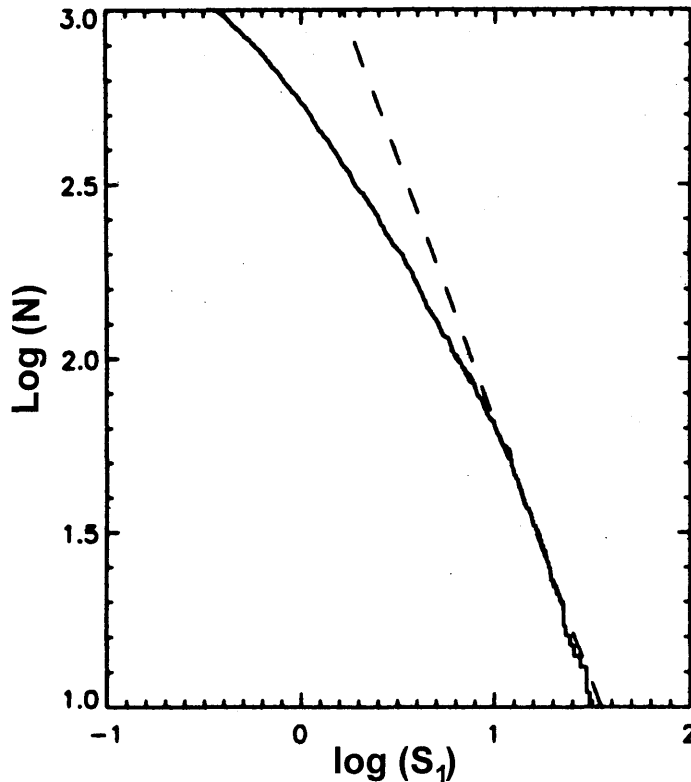
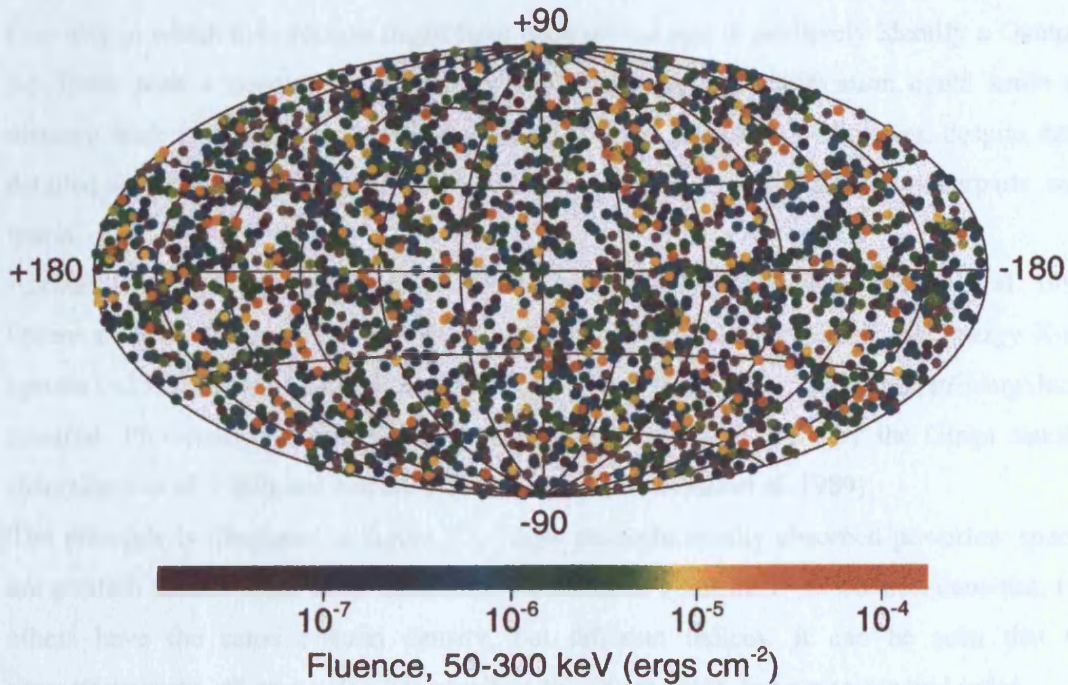




**Figure 1.7:** A sky map showing the locations of 2704 BATSE GRBs in galactic coordinates. The distribution is consistent with dipole and quadrupole moments of zero indicating isotropy. Notice that even the faint (ie; distant) events are evenly distributed.



Initially this meant the abandonment of galactic disk models (Paczynski 1993), but as more bursts occurred and the evidence for isotropy became more stringent, even the halo model had to be abandoned, leaving only the extended halo model and cosmological model (Hurley 1993; Woosley 1995). The cosmological model predicted the lack of faint bursts and also the isotropic distribution, but had always been unpopular as bursts occurring at that distance would need tremendous energy to produce the observed fluxes, even with the assistance of beaming. Therefore, most theorists continued to work with the extended halo distribution. However, continuing demonstration of isotropy by BATSE forced the model to extend to ever-larger scale heights, so as to hide effects caused by our offset from the galactic centre. This posed two problems: firstly no known population of objects had such a distribution and secondly if the scale heights became too large one would expect to see a concentration of bursts in the direction of M31, something that was not present in the data (Fishman 1995). Greater and greater statistical evidence continually reduced the narrow allowable region of scale heights (Hartmann 1996) to the extent that the mood began to change and many working in the field were forced to admit that the halo model seemed increasingly contrived (Fishman et al. 1995; Mitrofanov 1995). This led to renewed interest in cosmological models (Hartmann et al. 1995).

The TGNS model was in crisis and was dealt another blow when, like SMM, CGRO failed to observe any of the high energy emission lines that ISEE-3, Venera-11-14, PVO had reported and which had been attributed to electron-positron annihilation in the presence of a neutron star (Fishman 1996).

One way in which the problem might have been solved was to positively identify a Gamma-ray Burst with a counterpart in another wavelength. Such identification could settle the distance scale issue and also reveal the nature of GRB progenitors. However, despite many detailed searches of GRB error boxes in many wavelength regimes, no counterparts were found.

Another way to determine the distance scale to GRBs was suggested (Owens et al. 1993; Owens et al. 1995; Owens et al. 1995; Teegarden 1998): to observe their low energy X-ray spectra ( $<2$  keV) and look for photoelectric absorption by intervening interstellar/intergalactic material. Previously the lowest energy observations of bursts were by the Ginga satellite (Murakami et al. 1989) and extended down to 2 keV (Yoshida et al. 1989).

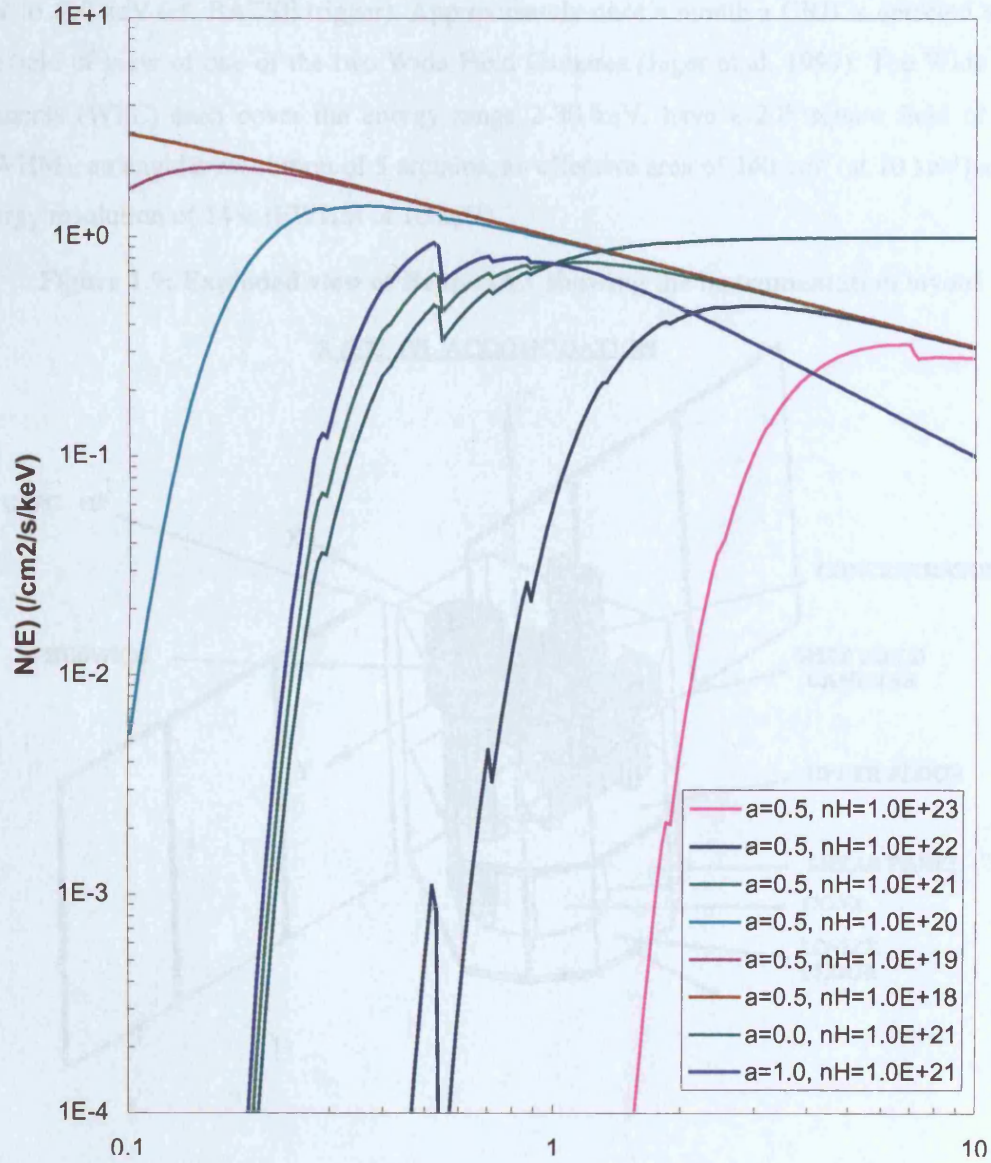
The principle is illustrated in figure 1.8. Eight photoelectrically absorbed powerlaw spectra are plotted: Six have the same index and normalisation, but different column densities, two others have the same column density, but different indices. It can be seen that the characteristic cut-off energy is quite sensitive to column depth, but not to spectral index.

Having suggested this diagnostic, Owens and Schaefer proposed a satellite mission called *RULER*. *RULER*'s principal instrument, the all sky monitor, would have been a PIP & CCD combination with a total field of view of  $3\pi$  sr. This proposal was unsuccessful, but connections between Owens, Leicester University and the University of New Hampshire (USA) led to a second opportunity for the soft X-ray spectroscopy method. UNH submitted a successful proposal (Forrest et al. 1994) to USRA for a small, dedicated, student led satellite named the Co-operative Astrophysics and Technology SATellite (CATSAT), to be run under the auspices of the STudent Explorer Demonstration Initiative (STEDI). CATSAT's principle instrument, the Soft X-ray spectrometer (SXR) is an array of Avalanche Photodiodes (APDs) with a field of view of approximately  $2\pi$  steradians and a low energy threshold around 600 eV. The wide view and low threshold were specified to enable CATSAT to see as many bursts as possible and to look for extinction in their low energy spectra.

However, CATSAT's launch has been delayed from 1997 to 2002 and a lot has happened in the mean time...



**Figure 1.8: The effect of column density on burst spectra at low energies.**  
Increasing column density strongly affects the cut-off energy, while the intrinsic spectral slope does not.

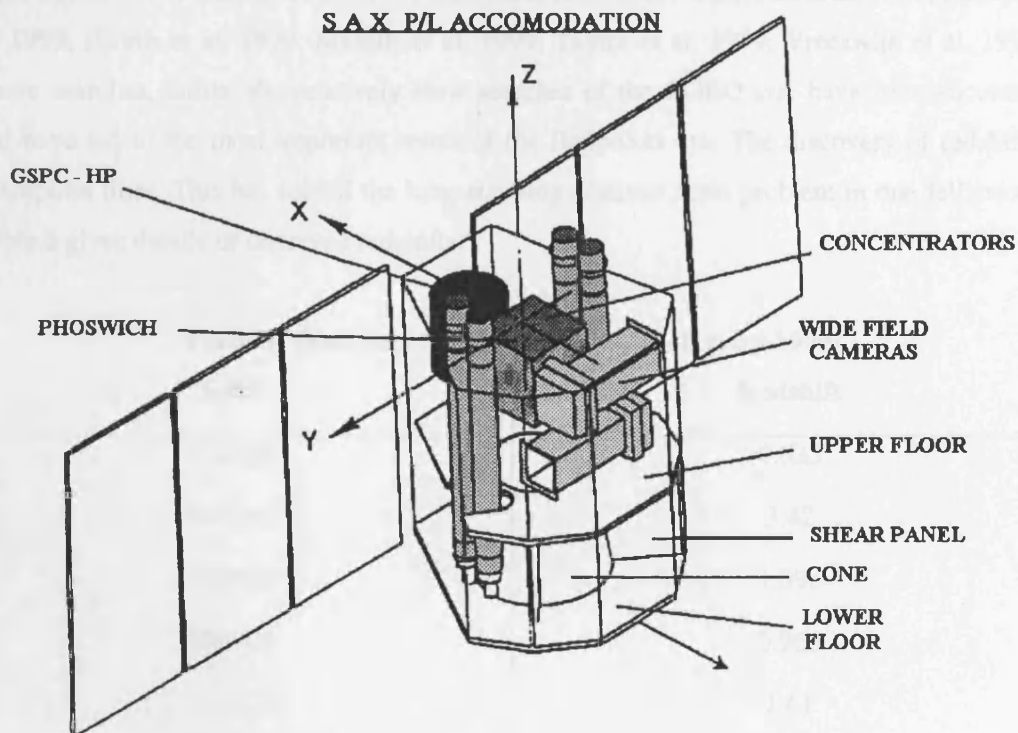


### 1.3 The current situation

In April 1996, the Italian-Dutch satellite BeppoSax was launched (Boella et al. 1997). This mission has brought about a revolution in our ability to observe GRBs by providing fast, precise locations, allowing observations of the burst site at other wavelengths. As a result, fading counterparts have at long last been observed in the soft x-ray, optical, infra-red and radio regimes.

The payload configuration of the SAX satellite is illustrated below in figure 1.9. The trigger for GRBs (Costa et al. 1998) is provided by the lateral anti-coincidence shields of the Phoswich Detection System (PDS) (Frontera et al. 1996). These cover an energy range of 60 keV to 600 keV (cf. BATSE trigger). Approximately once a month a GRB is detected within the field of view of one of the two Wide Field Cameras (Jager et al. 1997). The Wide Field Cameras (WFC) each cover the energy range 2-30 keV, have a  $20^\circ$  square field of view (FWHM), an angular resolution of 5 arcmins, an effective area of  $140 \text{ cm}^2$  (at 10 keV) and an energy resolution of 14% (FWHM at 10 keV).

**Figure 1.9: Exploded view of BeppoSAX showing the instrumentation layout**



For bursts taking place within the view of the WFCs it has been possible to make soft x-ray observations of unprecedented quality, following the time evolution of the burst through the initial phase and into afterglow (Frontera et al. 1999). Following the WFC observations, SAX's more sensitive Low Energy Concentrator Spectrometer (LECS) (Parmar 1996) and Medium Energy Concentrator Spectrometer (MECS) (Citterio et al. 1985; Conti et al. 1994; Boella et al. 1996) instruments may be slewed on target. Table 2 below describes these instruments. The LECS and MECS instruments have been able to follow many GRB X-ray afterglows days into their evolution (Antonelli et al. 1999; Costa 1999; Nicastro et al. 1999; Piro et al. 1999).

**Table 2: The properties of the LECS & MECS instruments on BeppoSAX**

<b>Instrument</b>	<b>Energy (keV)</b>	<b>Field of View (° FWHM)</b>	<b>Ang Res (arcmin)</b>	<b>Area (cm<sup>2</sup>)</b>	<b>Energy Res @ 5 keV (% FWHM)</b>
<b>LECS</b>	0.1-10	0.5	3.5 @ 250 eV	22 @ 250 eV	8.8
<b>MECS</b>	1.3-10	0.5	1.3 @ 6 keV	150 @ 6 keV	8.8

Furthermore, the rapid, accurate locations the WFCs provide allow ground based instruments to be trained on the site, allowing rapid counterpart searches at other wavelengths (Castro-Tirado et al. 1999; Galama et al. 1999; Gorosabel et al. 1999; Guarnieri et al. 1999; Hanlon et al. 1999; Hjorth et al. 1999; Masetti et al. 1999; Taylor et al. 1999; Vreeswijk et al. 1999). These searches, unlike the relatively slow searches of the CGRO era, have been successful and have led to the most important result of the BeppoSax era: The discovery of redshifted absorption lines. This has solved the long-standing distance scale problem in one fell swoop. Table 3 gives details of observed redshifts.

**Table 3: Observed Afterglow Redshifts (Hurley 1999)**

<b>GRB</b>	<b>Redshift</b>
970508	0.835
971214	3.42
980613	1.096
980703	0.966
990123	1.61

These observations clearly demonstrate that GRBs are a cosmological phenomenon and are not located in any extended galactic halo. This being the case, GRBs must radiate between  $10^{51}$  and  $10^{54}$  ergs, if they radiate isotropically, a truly extreme event by any standards.

The first problem that now faces GRB theorists is to provide an energy source (Rees 1999). The two most popular models today are the neutron star merger scenario (Narayan et al. 1992) and the "failed supernova", "hypernova" or "collapsar" model (Woosley 1993). Both of these scenarios rely on the creation of a black hole surrounded by a stellar mass accretion disk. The second problem is to explain how this event produces the observed Gamma-Ray Burst. The generally accepted solution is the "fireball shock model" (Rees et al. 1992; Meszaros et al. 1993) which predicts that a beamed, highly relativistic jet leaves the burst site.

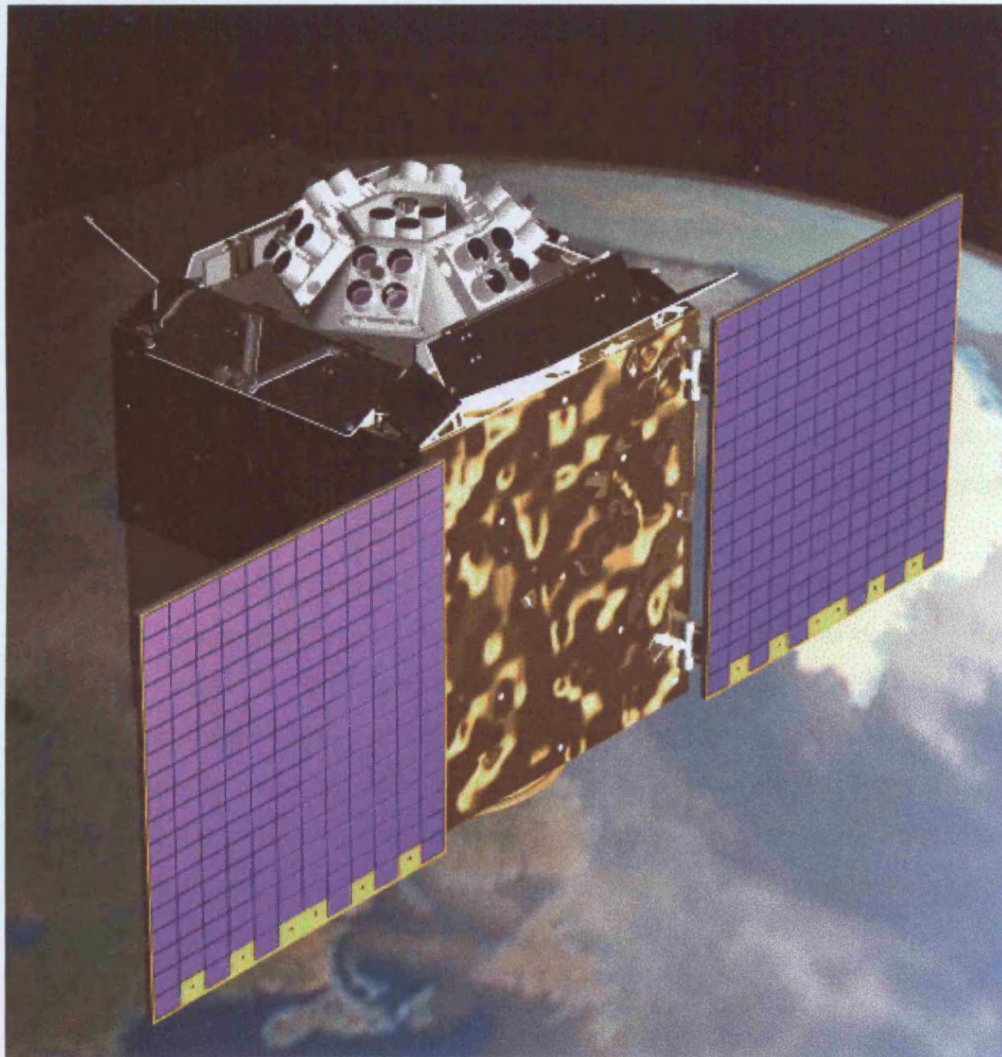
Different parts of the jet are travelling at different speeds and as these waves overtake each other "internal shocks" take place that produce synchrotron radiation. This explains the spectra of bursts and their complex time histories. The third problem is to show how the recently observed afterglow is produced and again, the fireball shock model provides an explanation: that the jet eventually impinges upon a stationary external medium causing an "external shock" resulting in synchrotron emission. This model has had some success in predicting the spectral shape and temporal decay of observed afterglows in the Gamma-ray, X-ray, optical and radio regimes. Several excellent reviews of all of these scenarios and models and their consequences and predictions have recently appeared (Meszaros 2000; Rees 2000).



## Chapter 2

# CATSAT and the Soft X-ray Spectrometer

Figure 2.1: The CATSAT satellite



## 2.1 CATSAT's evolution

CATSAT was a joint proposal between three institutions led by the University of New Hampshire (UNH), with principal investigator Dr David J. Forrest. UNH has responsibility for overall project management as well as several sub-systems including the onboard computer and power distribution. The second partner, Utah based Weber State University (WSU), was mostly involved in spacecraft structure, power and attitude control. Leicester University's main contribution was planned to be the soft X-ray instrument on-board CATSAT.

In 1994, CATSAT's **original** scientific goals were:

Primary goals

- **To provide the first determination of the distance scale to Gamma-Ray Bursts.**  
As discussed in chapter one, Owens & Schaefer had suggested that observations of the soft X-ray spectra of GRBs would reveal absorption by intervening hydrogen. If the hydrogen column depth could be determined, one could infer the distance to the GRB source. This would require bright bursts. Using a Monte-Carlo simulation, Owens and Sembay estimated that approximately 15 sufficiently strong ( $30\sigma$ ) events could be detected by CATSAT's baseline configuration annually. Even this small set of measurements could have solved what was at the time the most important problem in GRB studies.
- **To provide high signal to noise spectral measurements at energies from 500 eV to a few MeV.** In order to determine the spectral cut-off caused by intervening hydrogen, it is necessary to measure the spectral slope of the burst at higher energies. This necessitates a wide band mission. Moreover, such wide-band data had never been recorded before, making it a desirable goal in its own right.
- **To provide the first measurements of the polarisation of burst emission.**  
In 1994, burst spectra could equally well be matched by several competing models of burst emission. One difference between the models, however, was the type and extent of polarisation they predicted. For example, gyro-synchrotron emission was the preferred mechanism in the TGNS paradigm and this would produce elliptically polarised radiation. Rees' blast wave model predicted linear polarisation. Thus it was hoped that polarimetry might constrain the GRB emission mechanism and thereby progenitor model.
- **To search for cyclotron features in burst spectra at low energies.**  
According to the TGNS paradigm, which was still popular in 1994, cyclotron line features should be present in GRB spectra. GINGA did observe cyclotron features in

some burst spectra (Murakami et al. 1988) at energies around 20 keV, in contradiction to results from the much larger BATSE data set, which contained no such detections. However, these lines lie at the lower limit of BATSE's energy range. By observing bursts across a similar energy range to that of GINGA, it was hoped that CATSAT could confirm the existence or otherwise of these features.

- **To look for X-ray precursors and afterglows from GRB locations.**

GINGA observed low energy GRB precursors and tails from some bursts (Yoshida et al. 1989). These appeared to have a blackbody origin with a temperature in the region 1-2 keV. This was at the lower limit of Ginga's energy range, but well within the range of CATSAT.

Secondary goals

- **To act as an all-sky monitor for other transient phenomena (eg: Soft Gamma repeaters).**

CATSAT's role as a GRB monitor made it an ideal platform for monitoring other transient X-ray phenomena such as the SGR class of events.

- **To monitor solar flare activity throughout solar maximum.**

The planned launch date of January 1997 would have enabled CATSAT to observe the start of the 23<sup>rd</sup> solar maximum. With their strong background in solar physics (resulting in part from their success in the SMM mission), the UNH group was keen to use CATSAT as a solar flare monitor.

- **To measure solar flare polarisation above 30 keV.**

By observing the polarisation of solar flares at higher energies, where non-thermal mechanisms dominate, it was hoped that CATSAT would constrain the geometry of flare particle acceleration.

Unfortunately, CATSAT has undergone a significant launch delay: from Jan 1997 to July 2002. There are two principle reasons for the delay of CATSAT. The first is that problems with the proposed Pegasus XL launch vehicle have led NASA to cancel planned launches with this vehicle and seek alternatives. The second problem has been the failure of Weber State University to design an adequate spacecraft structure and the subsequent termination of their participation in the CATSAT programme. The production of the spacecraft structure and control software has been carried out by UNH, whilst the solar panels and attitude control software have been constructed at Leicester University. This extra workload has slowed the programme significantly.

During this time, other missions have performed a great deal of the science CATSAT set out to achieve. As described in chapter 1, BeppoSAX has been a tremendous success. The question of the distance scale of Gamma Ray Bursts is now largely settled and observations of GRBs have been made in many regions of the spectrum including the soft X-ray. Furthermore, CATSAT's other unique diagnostic tool, the GRB polarimeter (XAP), has had to be removed to save mass. As a result of these difficulties, the original CATSAT mission goals have had to be revised. CATSAT's new mission goals are:

- **To improve and enlarge the set of observations of GRBs in the soft X-ray regime begun by GINGA.**
- **To use HI absorption measurements to increase the number of GRBs for which distances are known.**
- **To provide high S/N spectral measurements at energies from a few MeV down to 500 eV.**
- **To look for X-ray precursors and observe early afterglows from GRB locations.**

As explained in chapter one, in the current era of Gamma-ray Bursts studies, there are two principle progenitor theories: the supernova and the neutron star merger. Supernovae are expected to take place at the end of the rather short lives of very massive stars. During their lives these objects will not have travelled far from their origins in stellar nurseries. This leads to the conclusion that supernovae would occur in dusty, gaseous environments. Neutron star binaries, on the other hand, are expected to have very great velocity, relative to their origins, and to have very long lifetimes. The eventual merger of a binary, then, would be expected to take place far from their stellar nursery, in a much "cleaner" environment. This provides a way to distinguish between the two models experimentally: by examining GRB spectra for photoelectric absorption in the soft X-ray band, a task for which CATSAT is well equipped. For this reason, a completely new mission goal has been suggested for CATSAT (Vestrand et al. ):

- **To look for soft X-ray absorption of GRB spectra as an indicator of the progenitor type.**



## 2.2 Scientific payload

The principle properties of the CATSAT instruments are shown below in table 2.1.

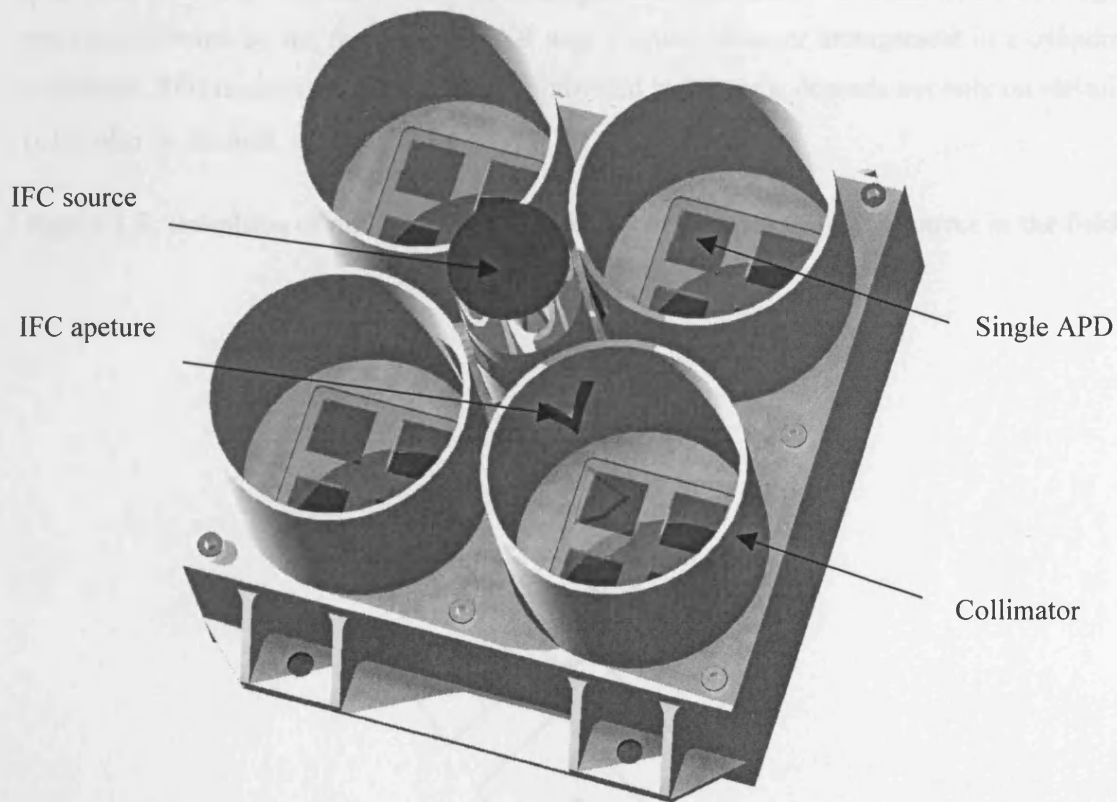
**Table 2.1: CATSAT's scientific payload**

Instrument	Energy Range (keV)	Detector technology	Purpose
SXR	0.5 → 20	7×16 passively cooled array of Avalanche Photodiodes (Si)	Observe GRB at low energy to measure spectral absorption
HXR	15 → 300	4× scintillator/PMT (CaF <sub>2</sub> (Eu))	Observe bursts over wide energy range.
DGS	250 → 5 000	3× scintillator/PMT (NaI)	Observe bursts over wide energy range. Trigger for other instruments
XAP (removed)	15 → 300	9× scintillator/PMT (NaI)	Observe X-ray albedo structure to measure polarisation

### 2.2.1 The Soft X-ray Spectrometer

The primary instrument on CATSAT is the Soft X-ray Spectrometer or SXR, which will measure the low energy spectra of bursts in order to determine their distance scale. In order to observe the effect of interstellar absorption below 2 keV, a detector with a low energy threshold (<500eV) is required, and so the baseline detection technology for the SXR is silicon based. The fact that GRBs are located randomly on the sky dictates that a GRB monitor instrument like the SXR should have a large field of view in order to maximise chances of seeing a burst. Therefore, the baseline for the SXR is an outward looking array of detectors with a field of view of approximately  $2\pi$  steradians. The detector needs no imaging capability to gather the required data. Burst locations will be determined by other instruments onboard CATSAT, and so the SXR is freed from providing good localisations.

At the time of the proposal, two possible detector technologies were considered for use in the SXR: Passivated Implanted Planar Silicon (PIPS) detectors and Avalanche Photodiodes (APDs). APDs have the advantage of high internal gain (around 100) and higher operating temperature (-40°C as opposed to -110°C). PIPS detectors on the other hand offer an in-built light filter (APDs require an external light filter) and a lower operating bias. The choice between the two technologies had to be made before the 1995 Universities Space research Association (USRA) on-site review, by which time the evaluation of the PIPS devices was still incomplete, so the more thoroughly studied APDs were chosen.

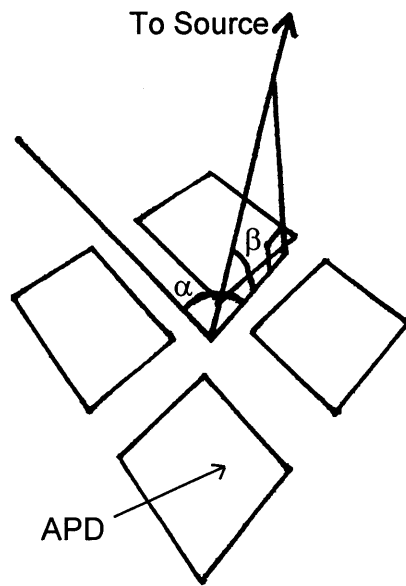
**Figure 2.2 A single SXR panel, comprising four collimated groups of four APDs**

The SXR is an array of seven flat panels of detectors, each panel containing four collimated groups of four APDs. Figure 2.2 shows a single complete SXR panel. Mounted in the centre of the panel is an Americium X-ray source monitored by a small scintillation counter. This source illuminates all 16 diodes in a panel with X-rays at  $\approx 14$  keV. X-ray detections in an APD that occur simultaneously with an  $^{241}\text{Am}$  decay detection in the scintillation counter are tagged as "calibration events". Since the energy of these X-rays is known, it will be possible to continually monitor and adjust the gains of all the diodes individually and automatically once CATSAT is in orbit. The collimators have a diameter of 46 mm and a length of 45.5 mm, so that the aperture subtends a solid angle of 0.803 sr at the centre of the group of APDs. The purpose of the collimators is to reduce the incident flux from the diffuse soft X-ray background. The four groups of APDs on a panel all observe the same part of the sky.

If a source illuminating an SXR panel from overhead moves off-axis, the collimator will start to cast a shadow over some of the detecting area. As the source moves further and further towards the horizon (decreasing elevation,  $\beta$ , in figure 2.3), the shadow becomes longer and the illuminated area decreases. Furthermore, the intensity of the illumination is reduced as the rays

are no longer normally incident. At some value of  $\beta$  around  $45^\circ$ , the shadow will cover all of the area of all four APDs and the source will no longer be visible at all. The situation is made slightly more complicated by the fact that the SXR uses a square detector arrangement in a cylindrical collimator. This means that the illumination provided by a source depends not only on elevation,  $\beta$ , but also on azimuth,  $\alpha$  (figure 2.3).

**Figure 2.3: Definition of alpha and beta, the azimuth and elevation of a source in the field of view simulations.**



A Fortran computer program has been written which divides the sensitive area of a panel into discrete surface elements, or "pixels". It is important to stress that these pixels are simply used as elements of the detection area and are not meant to imply any imaging properties. Given a source location, the program determines whether or not each pixel in turn can see the source, by calculating the location of the intercept of a line to the source with the plane of the collimator's aperture. By summing the area of all pixels that can see the source and then multiplying by a factor of  $\sin(\beta)$  (to allow for non-normal incidence), the program calculates the equivalent illuminated area, or detecting area, of the panel in that direction.

**Figure 2.4: Detecting area of a single SXR panel as a function of source location (all angles are in degrees)**

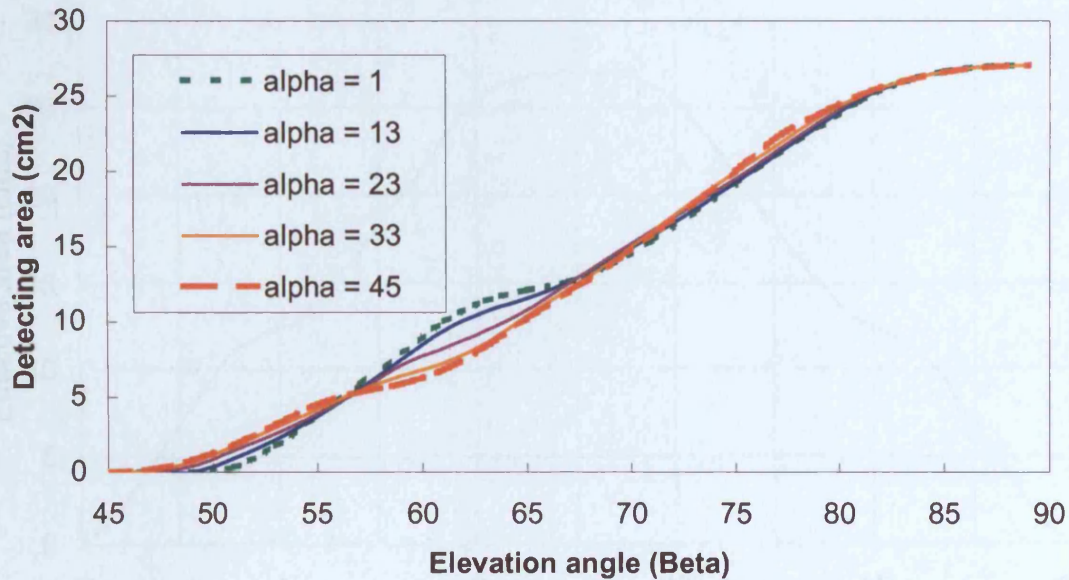
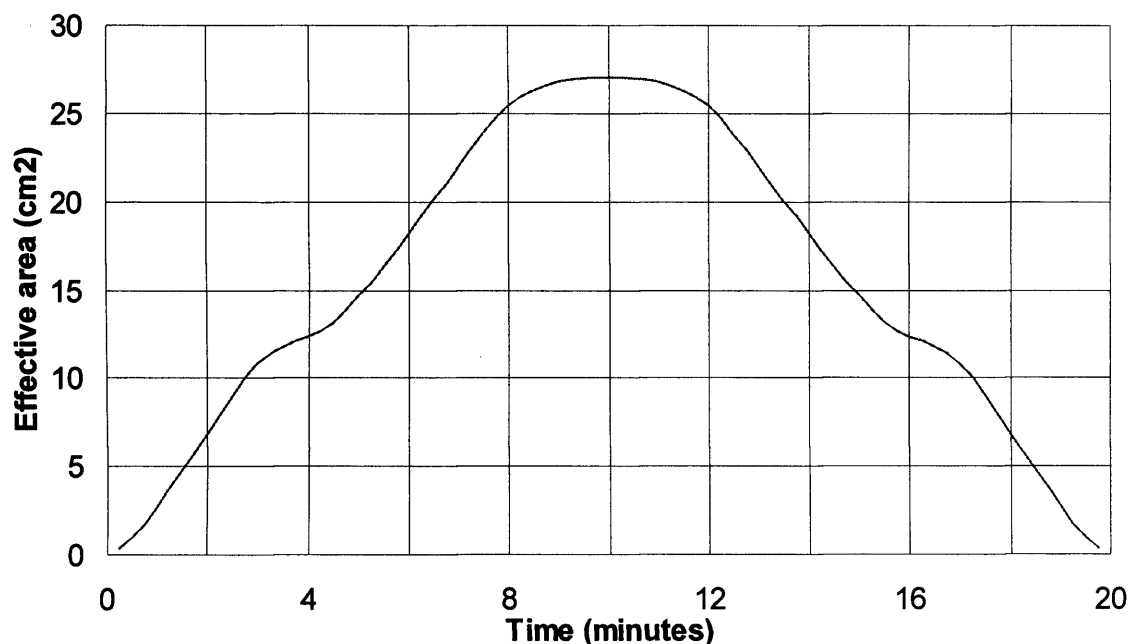


Figure 2.4 shows the variation of detecting area with elevation for a range of values of  $\alpha$ . Because of the symmetry of the problem, it is only necessary to consider  $\alpha$  between  $0^\circ$  and  $45^\circ$  and  $\beta$  between  $0^\circ$  and  $90^\circ$ . Since the detectors are in a square arrangement at the base of a cylindrical collimator, the source becomes visible sooner for  $\alpha=45^\circ$  than for  $\alpha=1^\circ$ , as the corner of the detector group is illuminated. However, by  $\beta=60^\circ$ , the situation is reversed and  $\alpha=45^\circ$  is less favourable than  $\alpha=1^\circ$ . This is because the receding shadow has uncovered more "dead" area between APDs for  $\alpha=45^\circ$  than for  $\alpha=1^\circ$ . Near normal incidence,  $\alpha$  becomes unimportant and the curves are very close.

The slew rate of CATSAT is approximately  $360^\circ/90 \text{ mins} = 4^\circ$  per minute. Figure 2.5 shows the effective area of a panel as a function of time for a source passing directly overhead at  $4^\circ$  per minute. In this scenario,  $\alpha=1^\circ$ . The source remains in field for nearly 20 minutes, but for much of that time it illuminates less than the full area of the panel.

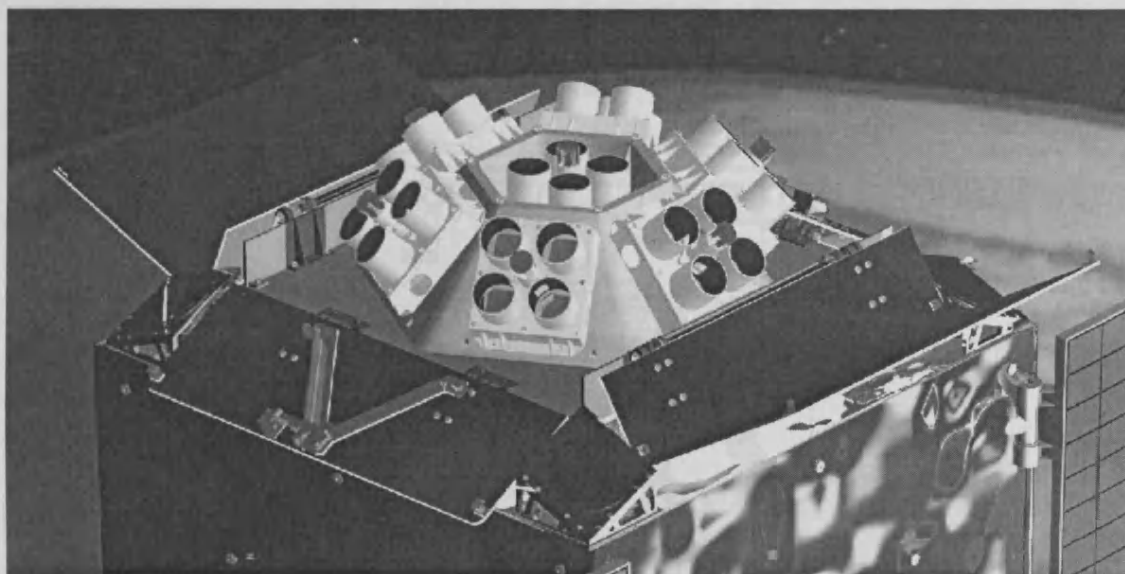
**Figure 2.5: Detecting area of a single SXR panel as a function of time as a source passes directly overhead ( $\alpha=1^\circ$ )**



The "grasp" of a detector is the integral of detecting area over solid angle. This integral has been performed numerically for a single SXR module: The approach outlined above was used to calculate the effective area presented to each of >10 000 elements of the entire sky, so that the total grasp was the sum of the products of solid angle and effective area. The grasp is  $15.4 \text{ cm}^2 \text{ sr}$ . Previously, this had been estimated more crudely:  $0.803 \text{ sr field of view} \times 16 \text{ diodes per SXR panel} \times 1.69 \text{ cm}^2 \text{ per diode} = 21.7 \text{ cm}^2 \text{ sr}$ .

Figure 2.6 shows the fully deployed SXR on top of CATSAT. The seven panels have fields of view which overlap, giving a total uninterrupted SXR field of view of approximately  $2\pi$  steradians. The orbit and orientation of CATSAT should ensure that the SXR is never directly pointed at the sun. When opened, the doors act as sunshields so that sunlight cannot be incident on the SXR. This is important because any stray light would increase the noise threshold of the APDs. Furthermore, solar heating would raise the temperature of the APDs above the required  $-40^\circ\text{C}$ .

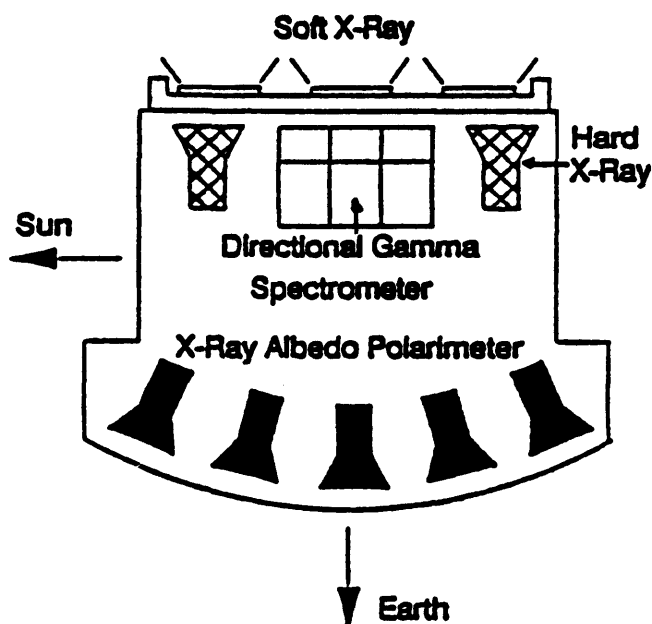
**Figure 2.6: The SXR mounted on top of CATSAT with the doors open**



### *2.2.2 The Directional Gamma-ray Spectrometer*

The second instrument planned for CATSAT is the Directional Gamma-Ray Spectrometer (DGS). It has an energy range of 150 keV to 10 MeV and consists of three identical scintillator/photomultiplier tube (PMT) assemblies. These are located side by side just beneath the SXR (see figure 2.7). The scintillating material is Sodium Iodide crystal. Despite being located within the spacecraft structure, the DGS is expected to have a nearly isotropic response, since at the photon energies to which the DGS is sensitive the spacecraft structure is transparent. The three assemblies will provide mutual shielding which will make it possible to extract directional information about a burst from the relative count rates. Monte-Carlo simulations suggest that a directional accuracy of around  $10^\circ$  is likely. The DGS will provide the burst trigger for CATSAT's other instruments. In the event of a trigger, data recording from the 3 instruments will change over from normal mode (continuous recording in 16 second time bins) to burst mode (continuous recording in 1 second bins) and remain in that mode for 256 seconds before returning to normal mode.

**Figure 2.7: A schematic of the instrument layout on board CATSAT**



### *2.2.3 The Hard X-ray Spectrometer*

CATSAT's third instrument is the Hard X-ray spectrometer or HXR. The HXR covers the energy range between the SXR and the DGS. This instrument consists of four outward looking scintillator/PMT assemblies, one mounted on each of CATSAT's top corners. The energy range of this device is 15 to 300 keV and the scintillating material is  $\text{CaF}_2(\text{Eu})$ .

### *2.2.4 The X-ray Albedo Polarimeter*

The final planned instrument was the X-ray Albedo Polarimeter (XAP). Conventional instruments for measuring the polarisation of X-rays use an internal scattering medium. Such devices suffer from a low field of view and a small effective area, making GRB detection unlikely. CATSAT's XAP system was to have used Earth's atmosphere as an external scattering medium. An array of nine scintillator/PMT assemblies would have pointed down towards Earth, each viewing a different  $40^\circ$  segment of the visible atmosphere surface. The relative angular intensity of the backscattered emission as recorded by the XAP, together with information about the spectral shape and arrival direction of the burst from CATSAT's other instruments, could have powerfully constrained the emission polarisation of the burst. Monte-Carlo simulations suggested that the XAP system could measure the polarisation fraction down to 50% in six bursts annually. The energy range of the XAP system was to be 15 to 300 keV and the scintillation medium selected



was Sodium Iodide. Unfortunately, the XAP system has been removed from CATSAT to save mass.

## 2.3 Mission

CATSAT was accepted by the Universities Space research Association (USRA) as a fully funded flight mission in September 1996, following which a total budget of 10 million US dollars was approved to include design, fabrication, testing and launch. After launch, funding is secure for a one-year nominal mission lifetime with an additional year possible.

Of CATSAT's three flight instruments, only the SXR has any pointing restrictions: that the SXR should not point to the Sun or the Earth. This requirement is most easily met by selecting a polar orbit over the dawn/dusk terminator. Furthermore, this orbit allows the solar panels to remain constantly in the sun, simplifying CATSAT's power requirements. CATSAT's attitude control system will maintain permanent illumination of the solar panels as well as keeping the Sun and Earth out of the field of view of the SXR. The orbit that has been negotiated with CATSAT's partner payload, ICESAT, is circular, with an altitude of 590 km (period approximately 90 minutes) and an inclination of  $\approx 97^\circ$ . This orbit causes CATSAT to pass over each pole once per orbit and through the South Atlantic Anomaly (SAA) once in 8 of every 16 orbits. During these periods, CATSAT will be exposed to high levels of charged particle radiation and it will not be possible to gather data from the science instruments. This will result in a total mission average observing efficiency of around 60%. Ground station passes will occur around 06:00 and 18:00 local time. With one ground station in UNH and one in Leicester, station passes will occur around 06:00, 11:00, 18:00 & 23:00 GMT daily.

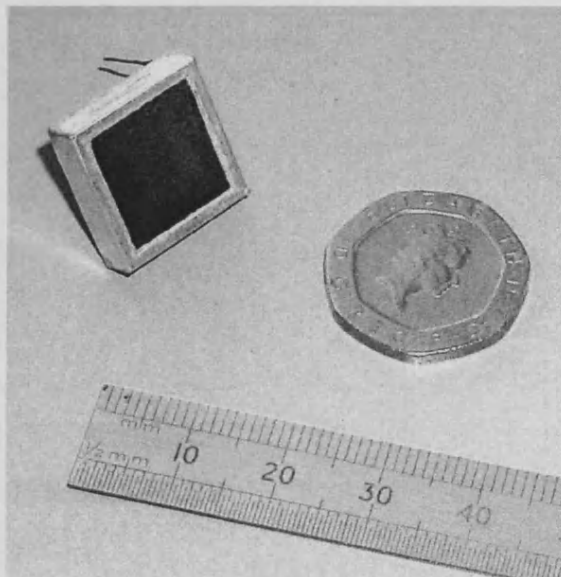


## Chapter 3

# The Avalanche Photodiode

Avalanche photodiodes have now been in existence for some 34 years (Locker et al. 1966). Until recently, these devices were very small, having an active area of only a few square millimetres, and were used for the detection of optical photons (in fibre optics etc...). APDs were first used in X-ray detection as an alternative to photomultiplier tubes in scintillation detectors (Entine et al. 1983; Reiff et al. 1983; Squillante et al. 1985; Farrell et al. 1990). Ten years ago, however, researchers at Radiation Monitoring Devices inc. realised that the APD could be used to detect soft X-rays by direct exposure (Squillante et al. 1986; Farrell et al. 1991). In order to make practical soft X-ray detectors, it has been necessary to produce devices with a much greater active area than was previously used. In 1994 the largest devices available had an area of  $1.69 \text{ cm}^2$  and were manufactured by RMD. It is these large area, high gain avalanche photodiodes that will be used on CATSAT. One such device is shown in figure 3.1

**Figure 3.1: A large area, high gain APD of the type used on CATSAT**



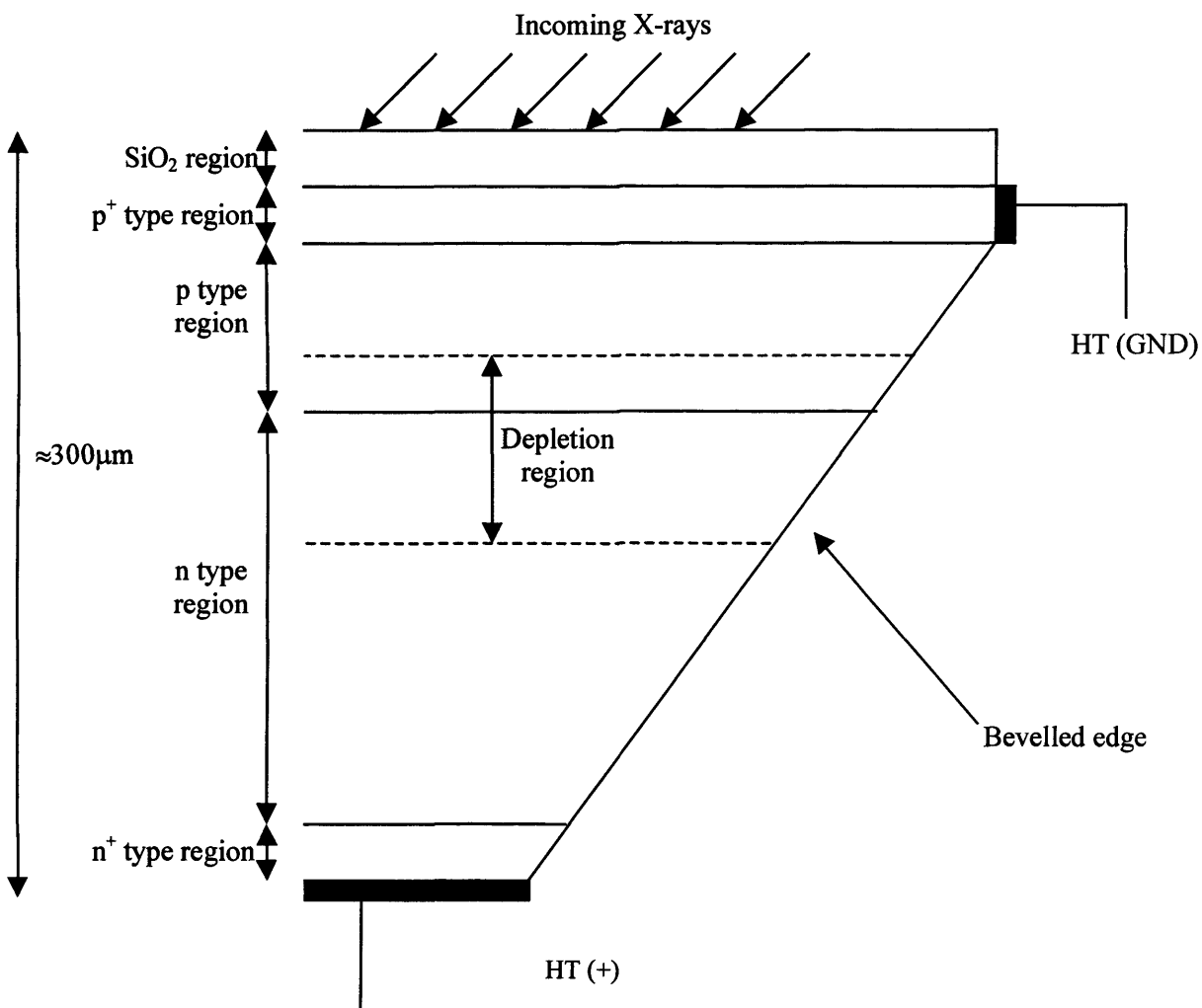
In this chapter the properties and use of APDs will be introduced. Section 3.1 will describe the APD as a semiconductor device. Section 3.2 introduces the APD as a detector of soft X-rays. The Experimental setup used in gathering data from APDs will be described in section 3.3. Section 3.4 will discuss the application of a thin layer of Aluminium onto the front surface of APDs to prevent detection of unwanted optical photons. Section 3.5 outlines what has been learned about APD detection efficiency. Section 3.6 describes the nature and origin of a shelf in APD pulse height distributions. Finally, section 3.7 explains the origin of peak asymmetry in APDs.

### 3.1 The APD as a semiconductor device

#### 3.1.1 Internal Structure

The APD is a basic, silicon based p-n junction device. All diodes will resist reverse bias, allowing no current to pass, up to a point called the breakdown potential. Above this potential the junction becomes conducting.

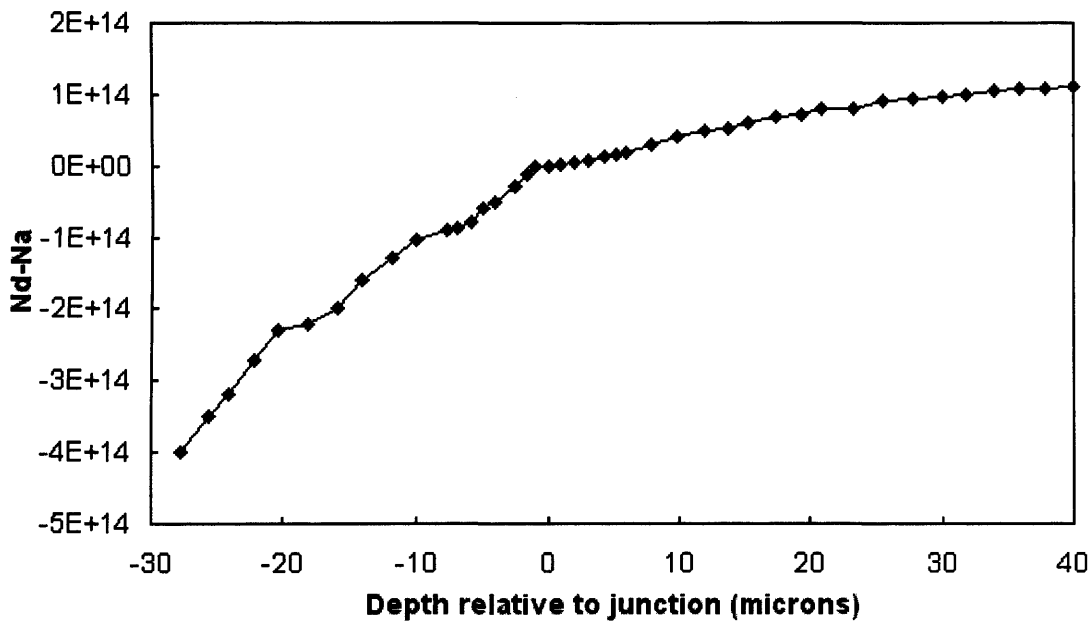
**Figure 3.2: A schematic cross section of the edge of an APD**



APDs are designed to have an exceptionally high breakdown potential ( $\approx 1600$  V). The doping profile in our APDs is produced by diffusion. The edges of the device are bevelled to prevent surface breakdown. Figure 3.2 shows a schematic diagram of an APD.

The theoretical and measured doping profiles for a typical large area, high gain APD manufactured by RMD have been published by Farrell (Farrell et al. 1994) and Redus (Redus et al. 1996). Figure 3.3 shows their measurements;  $N_d$  is the doping concentration of donor ions and  $N_a$  is the doping concentration of acceptor ions.

**Figure 3.3: An APD doping profile, measured by Farrell et al (1994)**



### 3.1.2 Storage and Handling

APDs are extremely sensitive to moisture and have to be stored in a dry nitrogen atmosphere. Exposure to moisture leads to a failure mode whereby the diode becomes progressively more noisy under operation until the noise threshold obscures interesting X-ray data. The mechanism behind this form of damage is not understood. At Leicester and UNH diodes are stored and handled in nitrogen-filled glove boxes and exposed to air as little as possible.

## 3.2 The APD as an X-ray detector

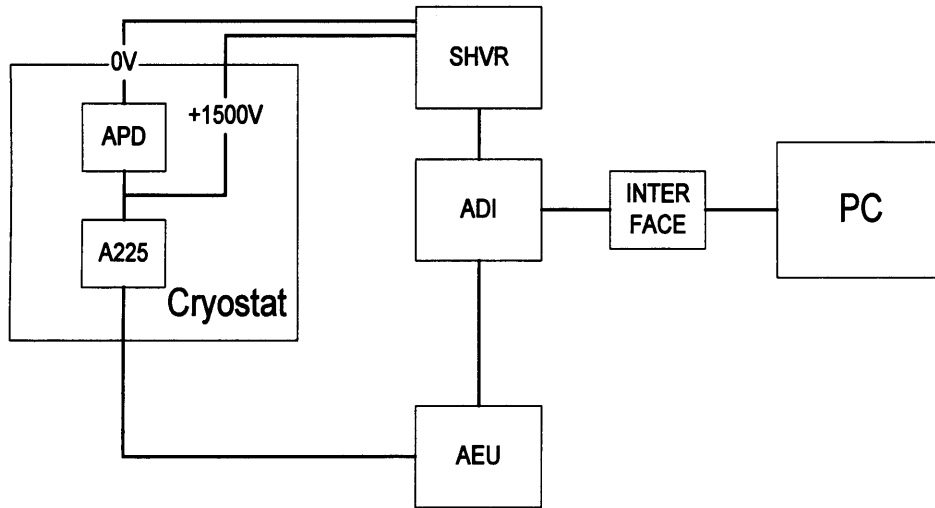
### 3.2.1 Basic mechanisms

As with other kinds of silicon based X-ray detector, X-rays interact with APDs by the photoelectric effect producing an energetic primary photoelectron which then gives up its energy by liberating a cloud of secondary photoelectrons. These secondary photoelectrons have little energy and are usually created near the site of the initial X-ray interaction. On average, the total number of electrons created as a result of one X-ray of energy  $E$  is given by:

$$n = \frac{E(\text{eV})}{3.62} \quad \text{Eq 3.1}$$

The depth at which the X-ray is absorbed is the primary factor in determining what happens to the photoelectrons. Ideally, they all pass through the diode from the front to the back, experiencing uniform gain as they pass through the avalanche region. The amplified signal is then collected at the back of the device and passed on to the electronics which are illustrated schematically in figure 3.4.

**Figure 3.4: A schematic diagram of the detector electronics**



At Leicester APDs are used with a PC running purpose written software which is able to control the biases on 16 APDs individually and process their individual output spectra. The PC is connected to the flight electronics modules via a simple interface box. The first flight system in the chain is the Analogue to Digital Interface (ADI). This unit accepts digital commands to set the voltages on the APDs and passes those commands on to the Series High Voltage Regulator (SHVR). The SHVR applies the required biases to up to 16 APDs at a time (for simplicity, only one is shown in figure 3.4). Charge pulses leaving the APD are detected by a A225 charge sensitive pre-amplifier chip manufactured by Amptek. This converts the charge to a voltage pulse which is sent out of the cryostat to the Analogue Electronics Unit (AEU). The AEU accepts pulses from up to 16 A225s at once (for simplicity, only one is shown in figure 3.4). The AEU acts as a shaping amplifier and also as a low-level thresholder. The output pulses from the AEU are passed to the ADI which digitises the pulse

heights and sends results to the interface box and the PC. The Software on the PC then produces a histogram of the pulse heights for the user. The ADI, SHVR, AEU and Amptek chips are all genuine flight components. When these systems are installed aboard CATSAT, the PC interface will be replaced by a Digital Electronics Unit (DEU) to record pulse heights and interface to the rest of the spacecraft.

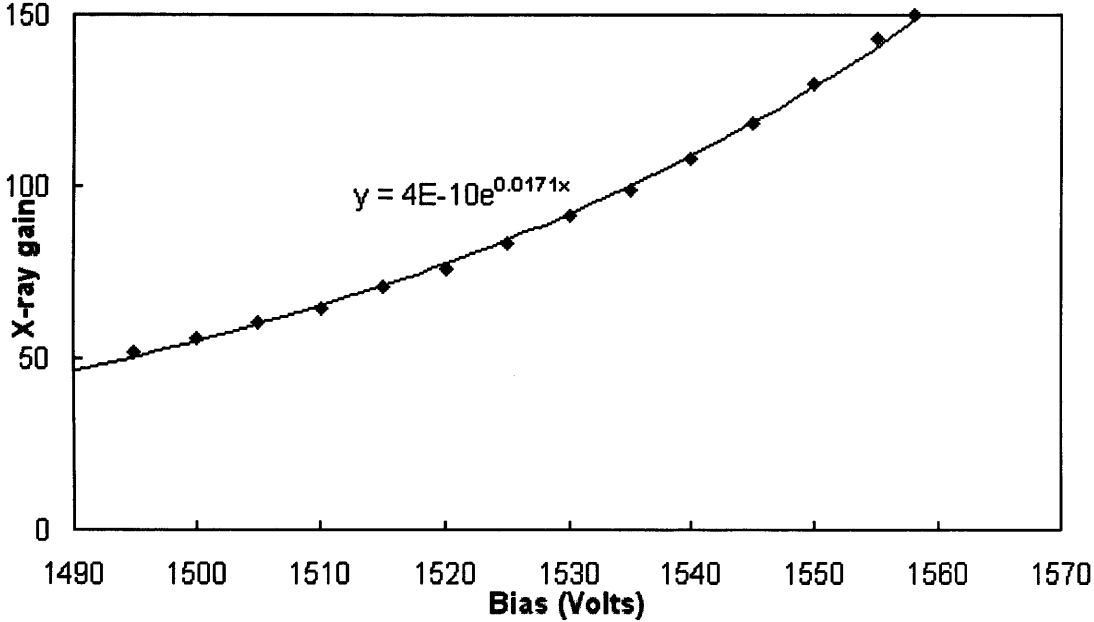
Like all silicon based X-ray detectors, APDs have lower noise thresholds at lower temperatures. An operational temperature of  $-40^{\circ}\text{C}$  has been selected for the CATSAT SXR, as a compromise between improvements in detector properties and risk of thermal damage to ancillary electronics. At these temperatures the noise from an APD is approximately 2500 e<sup>-</sup> rms.

#### *3.2.2 Signal multiplication and McIntyre theory*

Avalanche gain is the property of an APD that distinguishes it from other kinds of silicon based detector. Around the p-n junction of a diode with no voltage applied to it, there exists a narrow region where charge carriers (electrons and holes) have re-combined with one another (the depletion region). This region, in contrast to its surroundings, is very resistive. If a reverse bias is applied to the device the depletion region becomes thicker. Because of its electrical resistance, most of the applied bias falls across the depletion region, creating a region of strong field. As the bias is increased still further, the depletion region thickens and the field within it becomes stronger. The enhanced field accelerates any electrons entering this region from the top of the diode. If the field becomes sufficiently strong, the electrons can gain enough kinetic energy to liberate more electron hole pairs by impact ionisation. These new charge carriers are accelerated and may cause further ionisations leading to a useful output signal. This is the process of avalanche gain. The section of the depletion region where the field is sufficiently strong to cause multiplication is called the avalanche region. The number of electrons leaving the avalanche region divided by the number that entered defines the electron gain of the diode,  $G$ . Avalanche gain also applies to any holes entering the avalanche region from the lower part of the device. However, the effective mass of holes is much greater than that of electrons, leading to a much lower impact ionisation probability (given the same field strength). Therefore, hole gain,  $H$ , is much lower than electron gain. This means that holes injected into the lower part of the APD travelling upwards do not cause create a useful output signal.

Adjusting the applied reverse bias controls the gain of an APD. Gain is very sensitive to bias, as shown in figure 3.5.

**Figure 3.5: APD gain as a function of bias. A 4% increase in bias results in a 200% increase in gain.**



A gain of 100 produces a signal that can easily be processed by CATSAT's electronics and so has been selected as the operational gain for our APDs, but most diodes could go considerably higher. However, gain may not rise indefinitely. If  $n$  electrons enter the avalanche layer from the top, the number of electrons leaving the avalanche layer at the bottom is  $Gn$ . The number of electrons created in this process is  $Gn - n$  and this is equal to the number of holes that were also created. Assuming that these  $(G-1)n$  holes are created at the bottom of the avalanche layer, they migrate upward through the avalanche layer seeing a gain  $H$ , resulting in  $H(G-1)n$  holes at the top of the diode. The number of holes created in this process is  $H(G-1)n - (G-1)n$  and this is equal to the number of electrons that were also created. If these  $(H-1)(G-1)n$  electrons are equal or greater in number than the  $n$  electrons that originally started the process, then the process continues indefinitely or spirals out of control. This is avalanche breakdown. In order to operate APDs as X-ray detectors it is necessary to satisfy the condition:

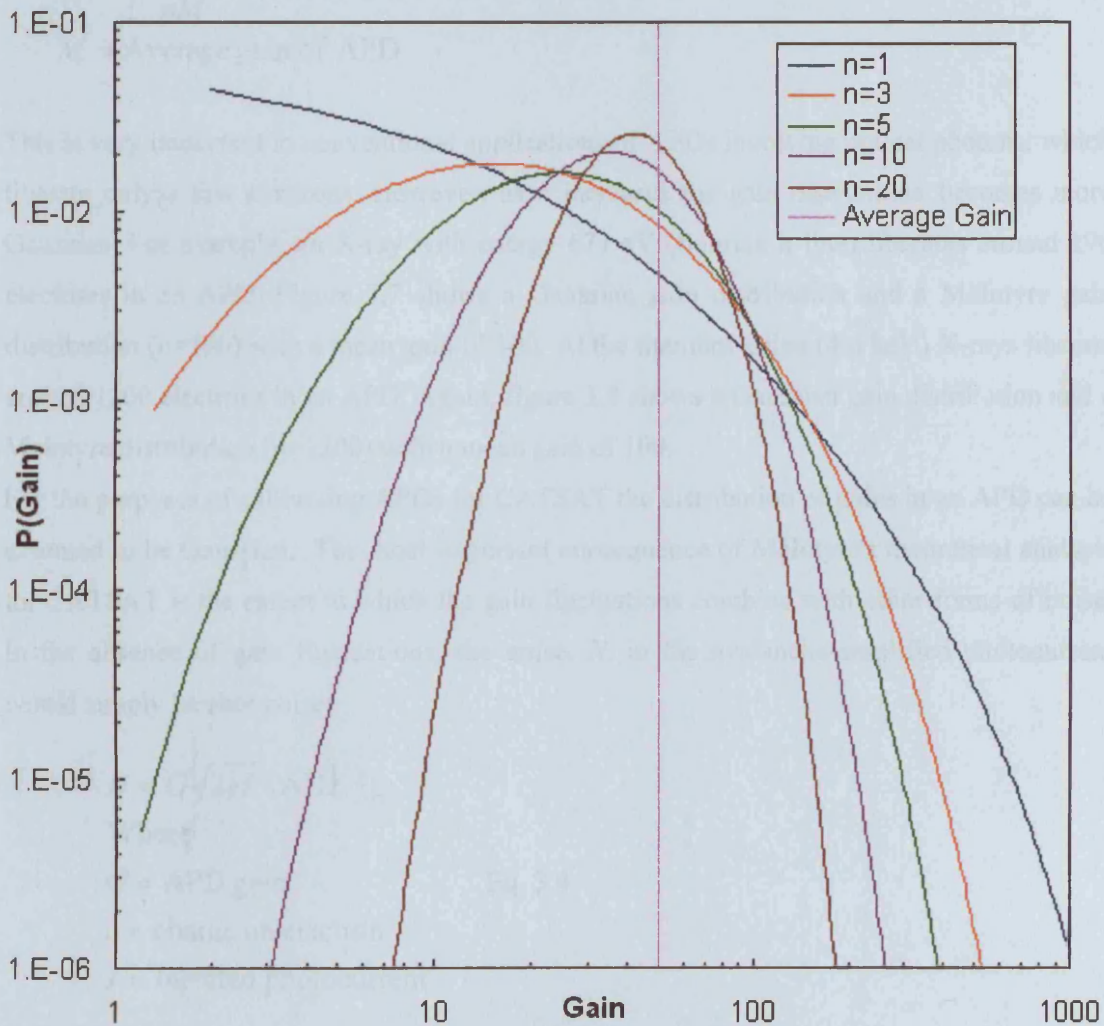
$$(H-1)(G-1) < 1 \quad \text{Eq 3.2}$$

None of CATSAT's flight APDs breakdown at values of  $G$  lower than 100, implying that the corresponding value of  $H$  must be less than 1.01.

The process of electron multiplication is not a predictable one. The collisions that create new electron-hole pairs are random, resulting in a distribution of gains from a single, uniform diode. The distribution of gains in APDs has been described in the past by McIntyre (1972), who showed that the gain distribution depends on the number of injected electrons,  $n$ , and is highly asymmetric for small values of  $n$  (see figure 3.6).

**Figure 3.6: McIntyre's distribution of gains in an APD with a mean gain of 50.**

Distributions are shown for several values of ' $n$ ', the number of injected electrons.



This work was experimentally verified by Conradi (1972). McIntyre's analysis was quite complicated and involved calculating the probability of  $n$  injected electrons causing exactly  $r$  ionisations within the avalanche region of the diode. The resulting probability distribution is given by:

$$P_{n \rightarrow n+r} = \frac{n}{\sqrt{2\pi r(n+r)(n+kr)}} \left(1 - \frac{nX}{r}\right)^r \left(1 + \frac{n(1-k)X}{n+kr}\right)^{\frac{n+kr}{1-k}} \quad \text{Eq 3.3}$$

Where :

$n$  = Number of electrons injected into the avalanche layer

$r$  = Number of ionisations that occurs as electrons cross the avalanche layer

$P_{n \rightarrow n+r}$  = The probability that an input of  $n$  electrons will result in an output of  $n+r$  electrons

$k$  = Effective ratio of electron and hole ionisation coefficients (a property of the APD)

$$X = \frac{n+r-nM}{nM}$$

$M$  = Average gain of APD

This is very important in conventional applications of APDs involving optical photons, which liberate only a few electrons. However, as  $n$  increases the gain distribution becomes more Gaussian. For example, an X-ray with energy 677 eV (fluorine k line) liberates around 190 electrons in an APD. Figure 3.7 shows a Gaussian gain distribution and a McIntyre gain distribution ( $n=190$ ) with a mean gain of 100. At the titanium k line (4.6 keV) X-rays liberate around 1200 electrons in an APD. Again, figure 3.8 shows a Gaussian gain distribution and a McIntyre distribution ( $n=1200$ ) with a mean gain of 100.

For the purposes of calibrating APDs for CATSAT the distribution of gains in an APD can be assumed to be Gaussian. The most important consequence of McIntyre's theoretical analysis for CATSAT is the extent to which the gain fluctuations combine with other forms of noise. In the absence of gain fluctuations, the noise,  $N$ , in the avalanche-amplified photocurrent would simply be shot noise:

$$N = G\sqrt{2eI} \quad \text{AHz}^{-\frac{1}{2}}$$

Where

$G$  = APD gain Eq. 3.4

$e$  = charge on electron

$I$  = Injected photocurrent

However, the effect of statistical fluctuations in gain is to introduce an excess noise factor,  $\epsilon$  (McIntyre 1966).



$$N = G\sqrt{2eI\varepsilon} \text{ AHz}^{\frac{1}{2}}$$

$$\varepsilon = G \left[ 1 - (1-k) \left( \frac{G-1}{G} \right)^2 \right]$$

Where

Eq 3.5

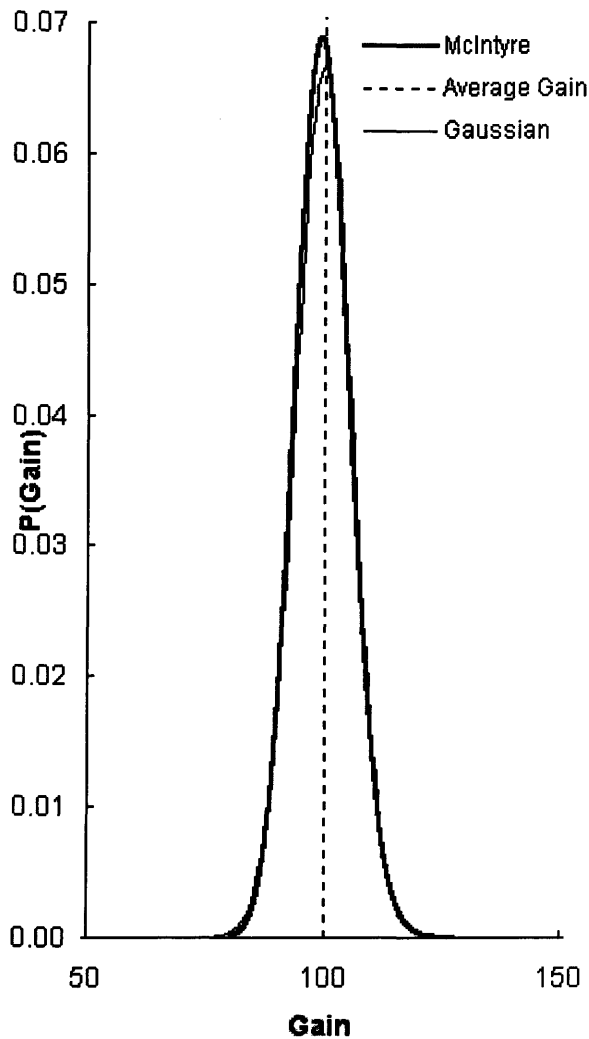
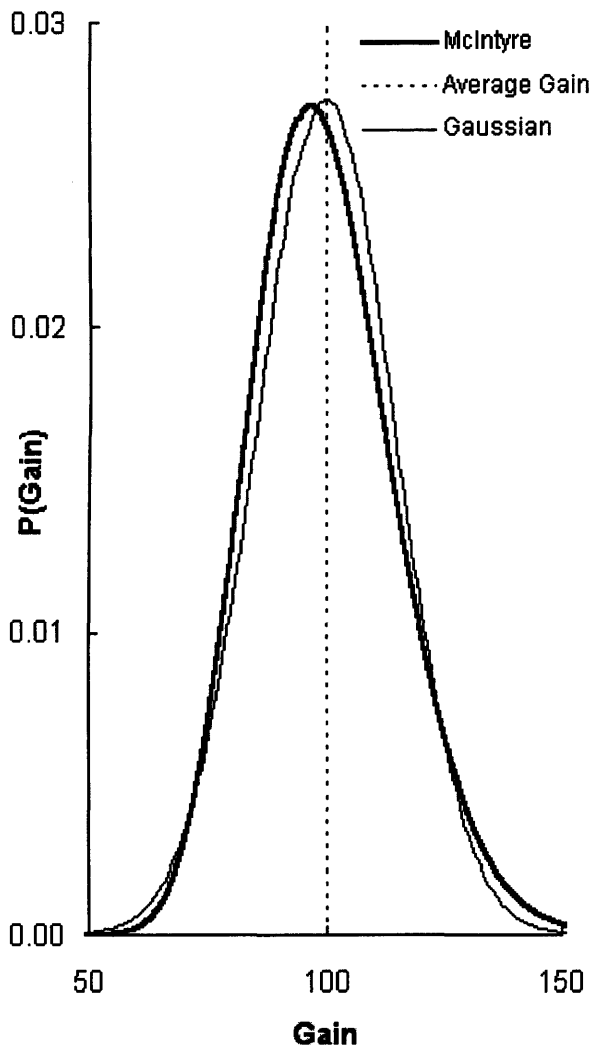
$\varepsilon$  = Excess noise factor

$k$  = Effective ratio of ionisation coefficients of electrons and holes

The electron and hole ionisation coefficients are different functions of electric field strength. Therefore, by adjusting the doping profile of a diode and hence the field profile within the device,  $k$  can also be adjusted (Redus et al. 1996). The value of  $k$  for early APDs was found to be around 0.0333, but researchers at RMD have determined experimentally that for CATSAT's devices  $k \approx 7 \times 10^{-4}$  (Redus et al. 1996).

**Fig 3.7: A Comparison of a McIntyre gain distribution and a Gaussian gain distribution for 190 input electrons.**

**Fig 3.8: A Comparison of a McIntyre gain distribution and a Gaussian gain distribution for 1200 input electrons.**



### 3.3 X-ray calibration equipment

All the data presented in this thesis was gathered using the JET-X test facility in figure 3.9.

**Figure 3.9: The Jet-X Test Facility**



This piece of equipment was originally constructed for the calibration of CCDs for the JET-X X-ray telescope programme and consists of various vacuum chambers, pumps, cold fingers, X-ray sources and detectors. The importance of the test facility lies in the fact that it enables a detector to be operated under vacuum and at any temperature between  $-100^{\circ}\text{C}$  and  $+30^{\circ}\text{C}$  and then to be illuminated by a monochromatic X-ray beam of known energy and flux.

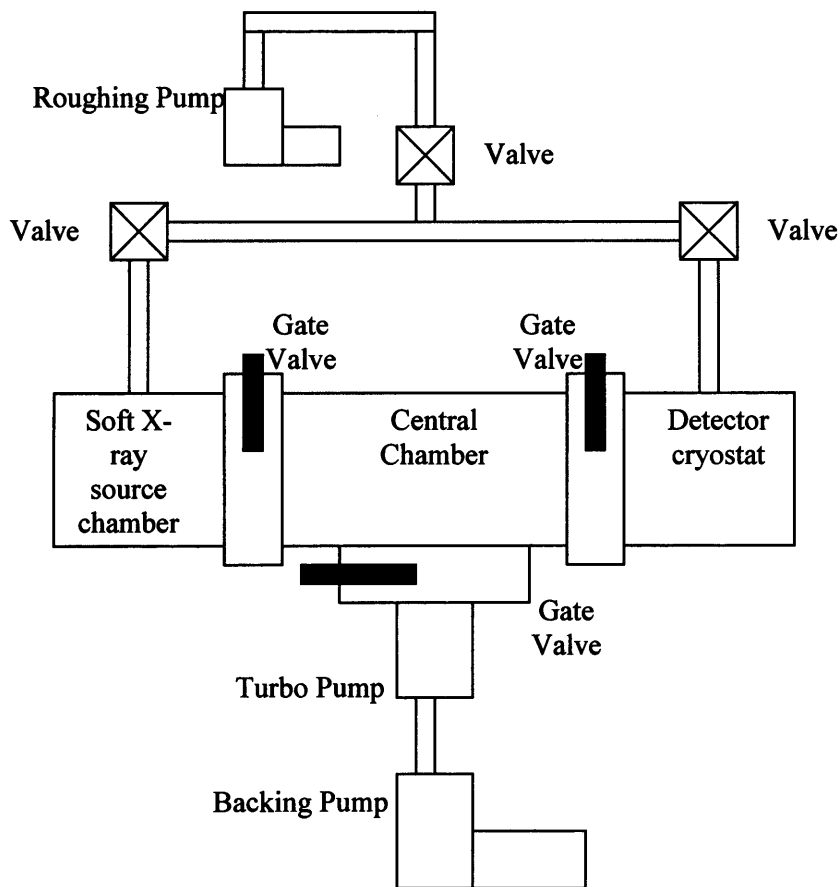
#### 3.3.1 Vacuum and cooling

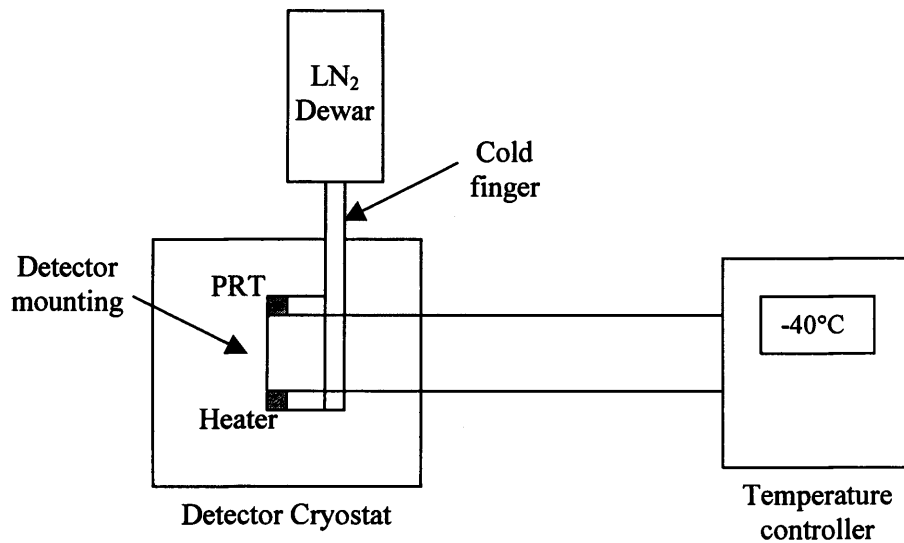
From a vacuum standpoint the test facility can be thought of as three discrete chambers separated by two gate valves (figure 3.10). The central chamber is attached to the turbo-pump that maintains an operating pressure of  $\approx 4 \times 10^{-5}$  mb. On one end is the detector cryostat and on the other is the soft X-ray source chamber. These two chambers can also be connected to a small roughing pump. All three chambers are monitored by a Penning gauge and a Pirani gauge.

This arrangement allows the soft X-ray source chamber or the detector cryostat to be isolated and back filled (for detector swap out or source anode re-coating) while the rest of the facility remains under vacuum.

X-ray detectors are mounted onto a cold finger in the detector cryostat. The cold finger passes out of the cryostat and connects to a dewar of liquid Nitrogen. In this way it is possible to cool the detector to  $-170^{\circ}\text{C}$ . This cooling is opposed by two electrical heaters which are regulated by an external temperature controller that monitors the detector's temperature with a Platinum Resistance Thermometer (PRT) (figure 3.11). This feedback system easily achieves a stability of  $\pm 0.1^{\circ}\text{C}$  at the  $-40^{\circ}\text{C}$  operating temperature that CATSAT's APDs require.

**Figure 3.10: A schematic of the JET-X Test facility vacuum system components**



**Figure 3.11: Arrangement for cooling detectors in JET-X test facility**

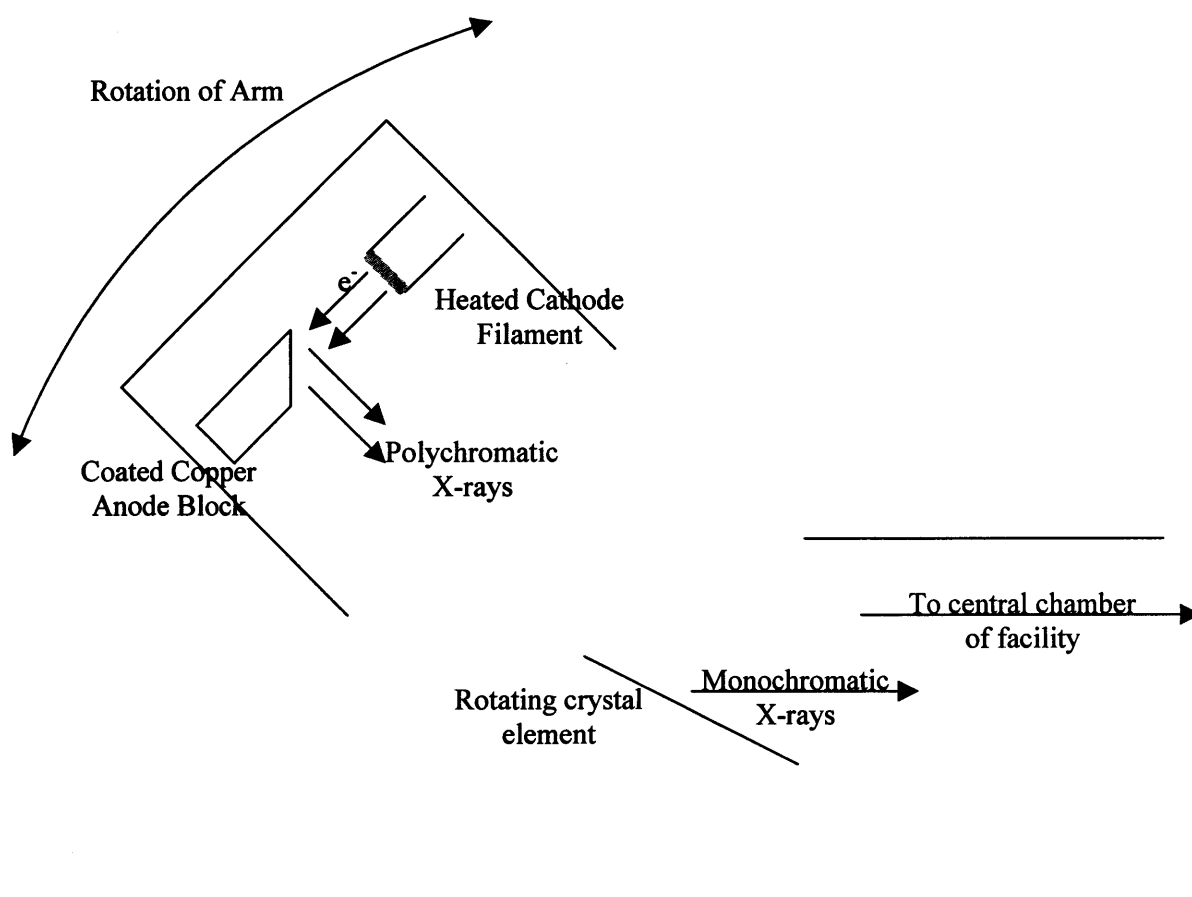
### 3.3.2 X-ray sources

The test facility uses two different X-ray sources. The first is mounted on the central chamber and consists of a commercial "Kevex" electron bombardment X-ray tube, used to excite fluorescence in different material targets mounted on a target wheel. By changing the targets, it is possible to produce a wide range of X-ray energies. The targets that have been used for CATSAT and their fluorescence energies are given below in table 1. The second X-ray source is of "in-house" origin and is mounted on the soft X-ray source chamber of the test facility. A simple heated-cathode/coated-anode electron bombardment arrangement is located at the end of an arm that is free to rotate about a crystal. The X-ray spectrum leaving the anode consists of X-ray lines from the coating material and bremsstrahlung. The arm is rotated about the crystal as shown in figure 3.12 to monochromate the X-rays by Bragg reflection.

**Table 1: Target materials used with the Kevex source**

Target Material	X-ray Energy (keV)
Mg	1.253
Al	1.487
Si	1.74
Ti	4.511
Fe	6.404
Cu	8.048

**Figure 3.12: A schematic diagram of the soft X-ray source and monochromator assembly**



The anode coating material and crystal can both be changed, as can the arm angle and crystal angle, making it possible to provide a variety of X-ray energies. Those that have been used for CATSAT are listed below in table 2.

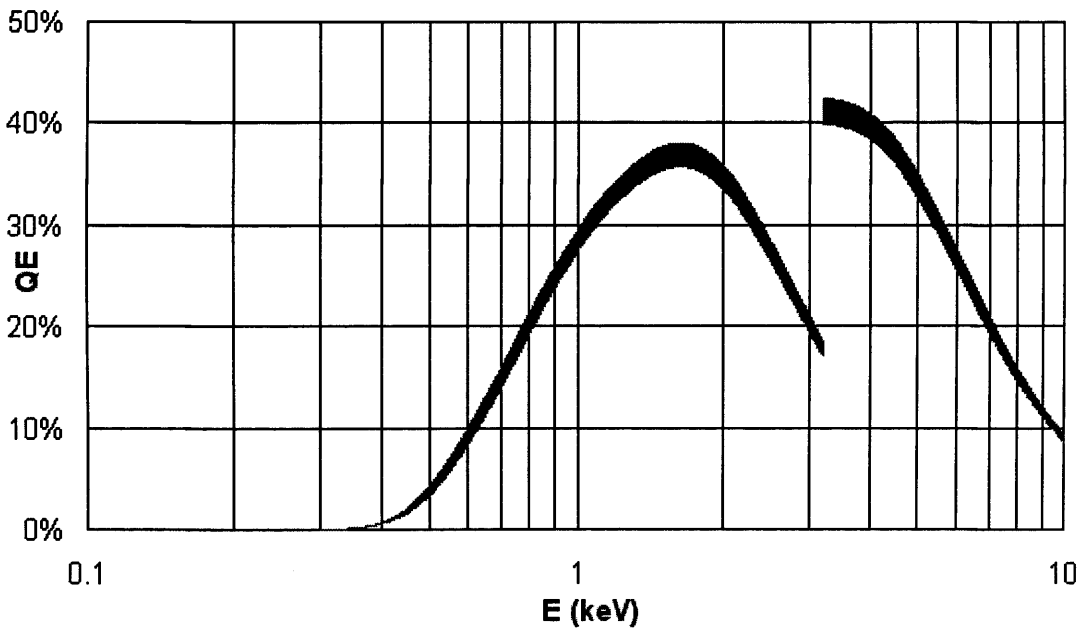
**Table 2: Coatings used with the soft X-ray source**

Active element in coating	X-ray Energy (keV)
F	0.677
Na	1.041
Cl	2.622

### 3.3.3 Gas Proportional Counter reference detector

The reference detector forms a crucial part of the JET-X test facility, as it allows the absolute X-ray flux to be measured. This must be known in order to determine the quantum efficiency of the X-ray detector under investigation. The reference detector used is a Gas Proportional Counter (GPC) with a chamber depth of  $2.51 \pm 0.03$  cm filled with P10 (90% Argon, 10% Methane) at 1 atmosphere. The sensing aperture of the device is circular with diameter  $0.95 \pm 0.01$  cm. The window is manufactured from stretched polypropylene whose density has been determined to be  $1.8 \pm 0.1 \times 10^{-4}$  g cm<sup>-2</sup> by X-ray attenuation measurements in front of a CCD. The window is supported by an exterior mesh whose measured transmission is  $42 \pm 1\%$ . These data allow the QE of the GPC to be calculated. Figure 3.13 shows the QE curve and the associated error. The errors shown are based on the measurement errors of the parameters given above, not on any other sources of systematic error.

**Figure 3.13: Quantum Efficiency of Gas Proportional Counter on JET-X test facility**



### 3.4 APD Aluminising

Once CATSAT is in orbit, the moon will occasionally illuminate the APDs in the SXR. Since they are light sensitive, they must be protected from this, otherwise the noise will increase. The worst case for lunar illumination occurs when the moon is nearly full and illuminates the top two diodes in each collimator of the rearmost SXR panel, as shown below in figure 3.14.

**Figure 3.14: Worst case lunar illumination of SXR**

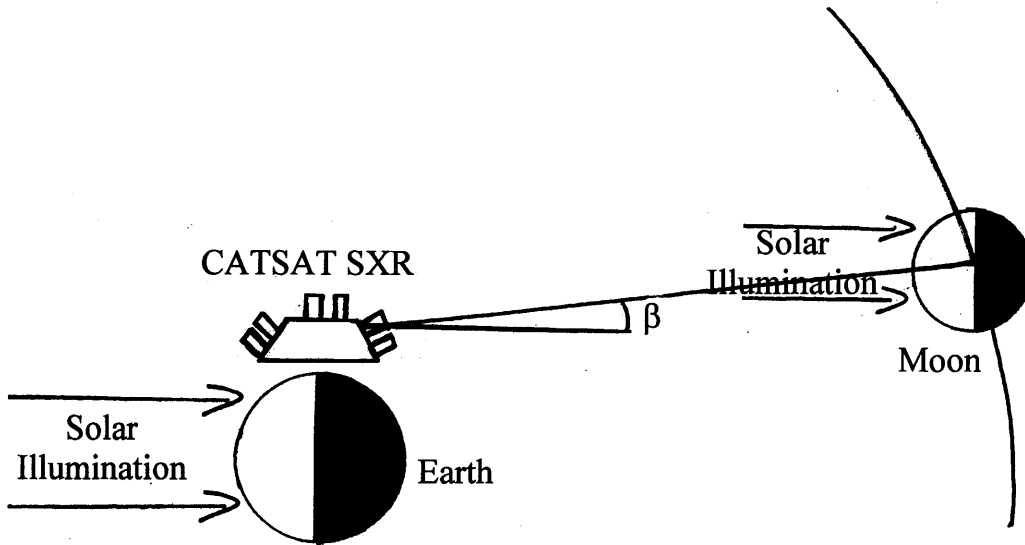
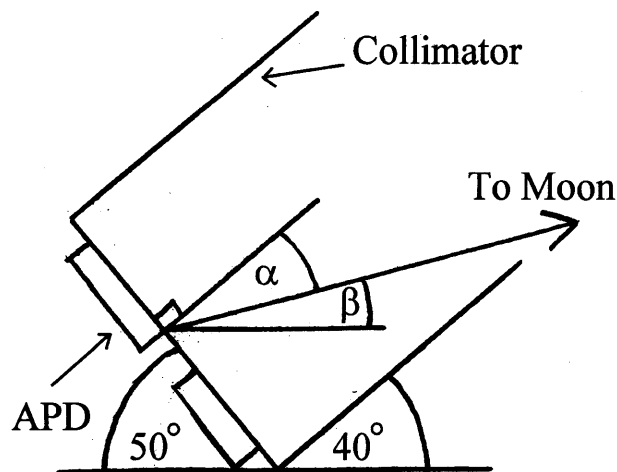


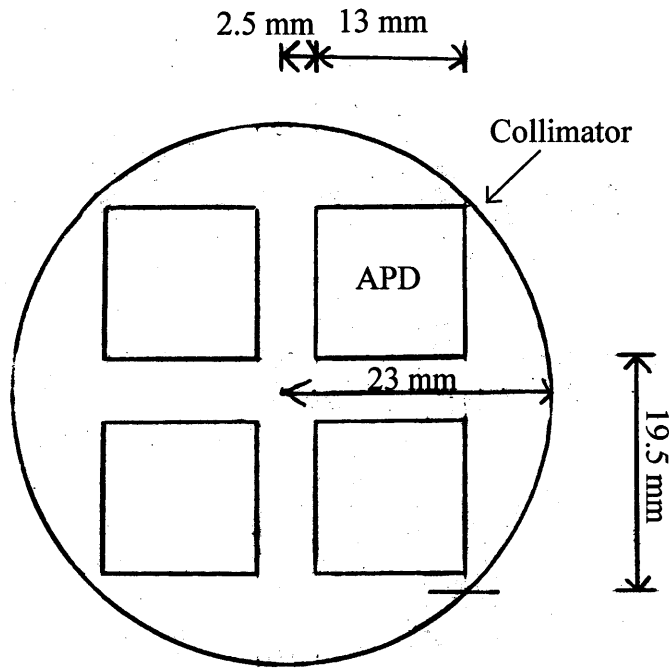
Figure 3.15 shows a close-up of one collimator, illustrating the geometry of this illumination. The collimator depth is 45.5 mm and the diameter is 46 mm. Because the collimator is cylindrical, not square in cross section, the moon vector does not clip the collimator tube in this drawing.

**Figure 3.15: The geometry of a single SXR collimator tube**



The arrangement of the APDs inside the collimator is shown below in figure 3.16.

**Figure 3.16: The arrangement of APDs in the collimator**



Therefore,  $\tan(\alpha) = 19.5 / 45.5$ , or  $\alpha = 23.2^\circ$ . This is the angle of incidence of the lunar illumination. Since  $\alpha + \beta = 40^\circ$ ,  $\beta = 16.8^\circ$ . So, the moon is  $16.8^\circ$  away from being full. Making the assumption that the moon is full, the power of the lunar illumination over the APD is given by:

$$P = I_0 a \times A_{APD} \times kF$$

Where :

$P$  = Power entering diode (W)

$I_0$  = Solar flux ( $1371 \text{ Wm}^{-2}$ )

$a$  = Moon's albedo (0.07)

$A_{APD}$  = Area of APD ( $1.7 \times 10^{-4} \text{ m}^2$ )

$k$  = Limb darkening factor for moon (conventionally  $2/3$ )

$F$  = View factor

Eq 3.6

The view factor can be calculated using formulae from Spacecraft Systems Engineering (Fortescue et al. 1995):



$$F = \frac{r^2}{R^2} \cos \alpha$$

Where :

$r$  = Moon's radius (1738 km)

$R$  = Distance to moon ( $3.5 \times 10^5$  km)

$\alpha$  = Angle of incidence ( $23.2^\circ$ ) Eq 3.7

So :

$$P = I_0 a \times A_{APD} \times \frac{2}{3} \frac{r^2}{R^2} \cos \alpha$$

$$\therefore P = 247 \text{ nW}$$

Assuming an optical responsivity of 0.3 A/W (common among silicon based photodetectors), this illumination corresponds to a photocurrent of 74 nA. If this illumination is attenuated by a factor of  $\gamma$  then the photocurrent falls to  $74/\gamma$  nA.

The noise in the photocurrent is simply shot noise:

$$N = \sqrt{2eI} \text{ AHz}^{-1/2} \quad \text{Eq 3.8}$$

Where  $e$  is the charge on an electron and  $I$  is the lunar photocurrent. This is increased by avalanche gain,  $G$ . The amplified noise is then:

$$N = G\sqrt{2eI\epsilon} \text{ AHz}^{-1/2} \quad \text{Eq 3.9}$$

Where  $\epsilon$  is the avalanche gain excess noise factor. The noise after pulse shaping is given by:

$$N_{amp} = \frac{N}{e} \sqrt{\frac{\tau}{2}} \text{ e}^- \text{rms} \quad \text{Eq 3.10}$$

where  $\tau$  is the amplifier peaking time. Substituting for  $N$  from Eq 3.9:

$$N_{amp} = G\sqrt{\frac{I\tau\epsilon}{e}} \text{ e}^- \text{rms} \quad \text{Eq 3.11}$$

This noise adds in quadrature to the diode's own internal noise  $n$  ( $n \approx 2500 \text{ e}^- \text{rms}$ ) to give the total 1-sigma noise level:

$$\sigma = \sqrt{\frac{G^2 I \tau \epsilon}{e} + n^2} \text{ e}^- \text{rms} \quad \text{Eq 3.12}$$

X-ray energy ( $E$ ) and charge ( $Q$ ) are related thus:

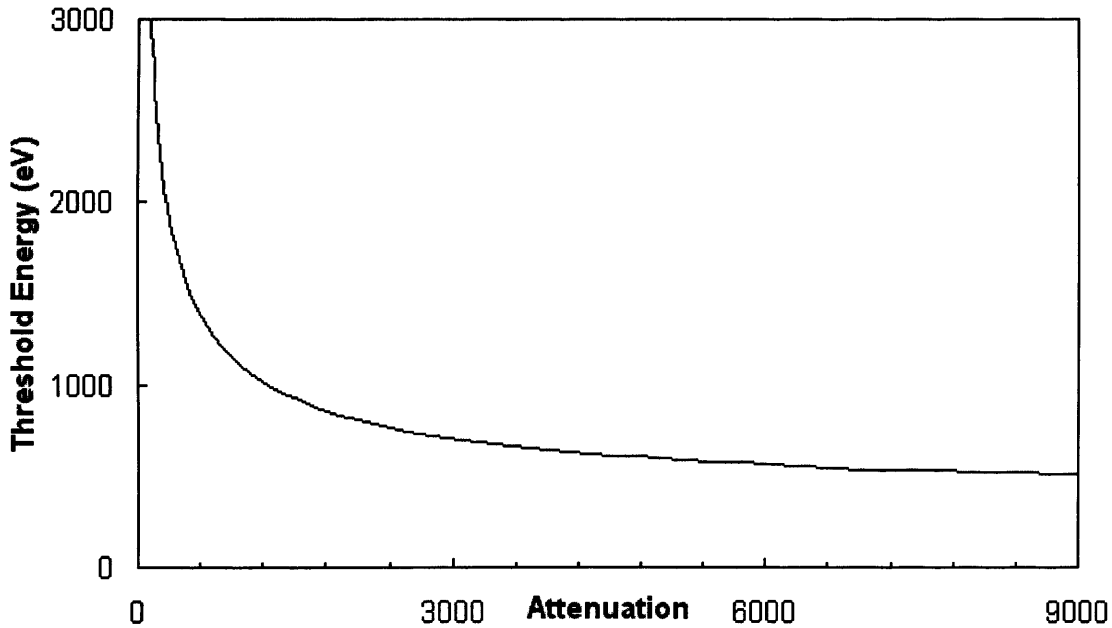
$$Q = G \frac{E(\text{eV})}{3.62} \quad \text{Eq 3.13}$$

So this noise level can be converted to an equivalent X-ray energy. The noise threshold of an APD has been found to be approximately six times the noise sigma. Therefore:

$$E(\text{eV}) = \frac{3.62}{G} \sqrt{\left(6G \sqrt{\frac{I\tau\epsilon}{e}}\right)^2 + (6 \times 2500 \text{ e}^- \text{ rms})^2} \quad \text{Eq 3.14}$$

Substituting  $G = 100$ ,  $I = 74/\gamma$  nA,  $k \approx 7 \times 10^{-4}$  and  $\tau = 2.4 \mu\text{s}$ , leads to the relationship plotted in figure 3.17.

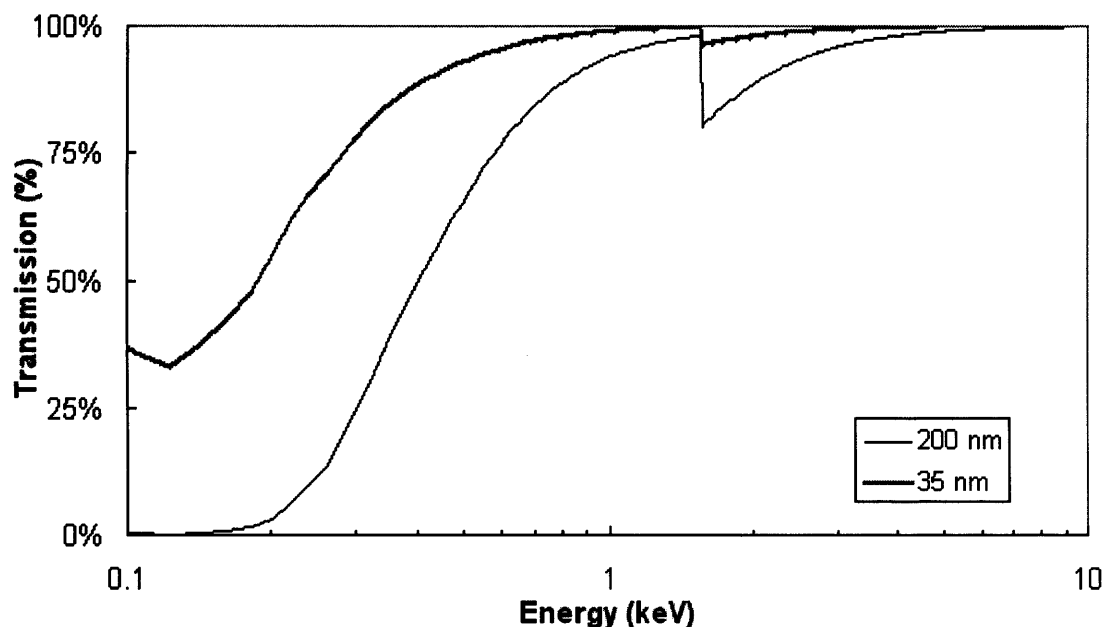
**Figure 3.17: The effect of optical attenuation on APD energy threshold**



An optical attenuation of around 2000 should be sufficient to keep the APD noise thresholds below 1 keV during periods of lunar illumination. Given that the optical reflectivity of Aluminium is 0.91 and the attenuation coefficient is  $1.5 \times 10^6 \text{ cm}^{-1}$  it should be possible to provide the required attenuation by depositing a layer of aluminium 346 Å deep. However, repeated tests of the aluminisation process have failed to produce the expected optical attenuation and it has been necessary to deposit 2000 Å to provide the required attenuation. Figure 3.18 shows theoretical transmission curves of these two filter depths. Past experience of Al deposition at Leicester indicates that this attenuation defect is due to a combination of

“pinholing” and oxidation (Aluminium oxide is transparent). In any case, 2000 Å of Al has been deposited onto the CATSAT flight APDs.

**Figure 3.18: Theoretical transmission curves of 35 and 200 nm of Al**



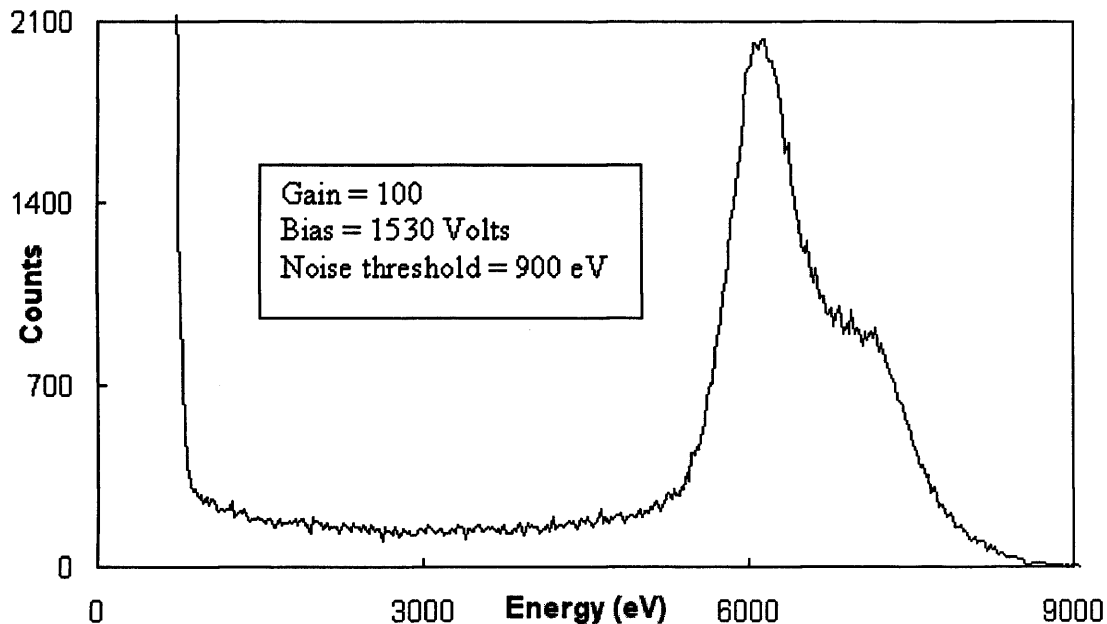
### 3.5 The detection efficiency of APDs

A typical APD pulse height distribution is shown in figure 3.19. The main feature of this spectrum is the peak around 6400 eV (in this case highly asymmetric). This is made up of those events whose charge was fully multiplied and collected. To the left of the peak is a wide region with relatively few counts per channel. This is known as the shelf. Counts in the shelf are X-ray generated. The escape peak (normally an important phenomena in detector physics) is effectively obscured by the shelf and is neglected in this work.

The Peak Quantum Efficiency (PQE) of an APD is the likelihood that an incident X-ray will interact with the diode resulting in a count in the peak of the pulse height distribution. This property is a function of photon energy. It has previously been suggested (Forrest 1995), that APD PQE might be described by the "standard" model of Si based X-ray detector efficiency: A SiO<sub>2</sub> dead layer at the front of the device (from which charge is collected incompletely or not at all) followed by a Si sensing region (from which charge is fully collected and multiplied) (Fraser 1989). We have adapted this model (figure 3.20) to include an aluminium dead layer (the light filter) and a further silicon dead layer (in response to new data from RMD). In our model the first dead layer is the aluminium light filter, which we expect to be 0.2 microns thick. The next dead layer is made of silicon dioxide, and should be approximately 0.1 microns thick (Farrell 1999). A heavily doped silicon dead layer follows

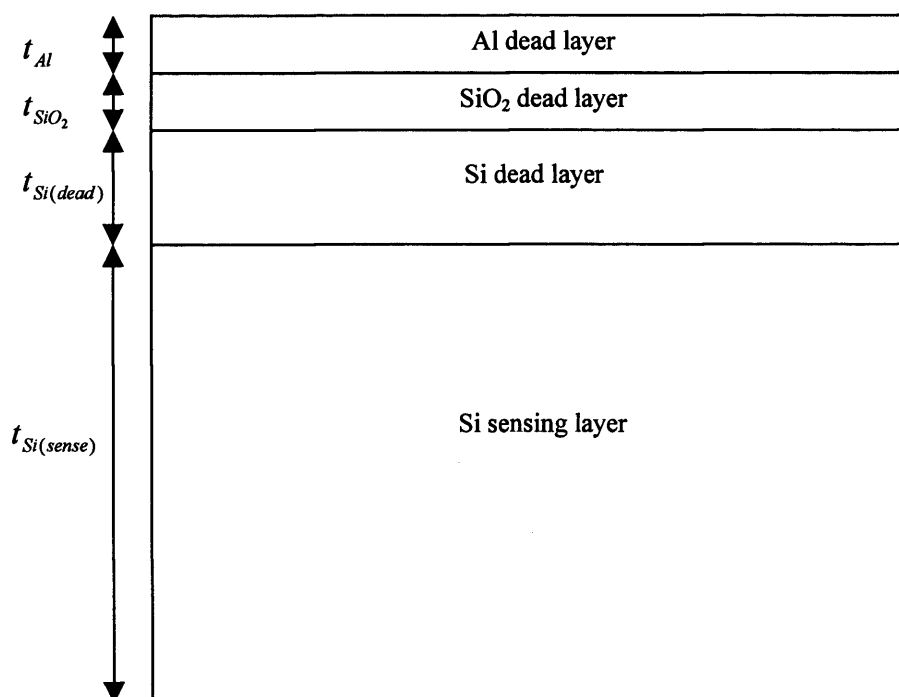
with an expected thickness of order 1 micron (Farrell 1999). A photon interaction in any of these three layers produces photoelectrons that are either partially or completely lost to recombination resulting in either a smaller output pulse or no pulse at all.

**Figure 3.19: Pulse Height Distribution from APD 112R (6.4 keV)**



This produces either no count in the pulse height distribution or a count to the left of the main peak. The sensing layer starts at the point where charge starts to be collected completely and none is lost to recombination and trapping.

**Figure 3.20: A layered model of APD structure for calculating PQE**



It ends at the start of the avalanche region, as any photons absorbed past this point would see reduced avalanche gain, resulting in pulses to the left of the peak. The sensing layer should be less than 40 microns thick (Farrell 1999). Given this physical model, Beer's law of exponential attenuation can be applied to derive an expression for PQE:

$$PQE(E) = e^{-t_{Al}\mu_{Al}(E)} \times e^{-t_{SiO_2}\mu_{SiO_2}(E)} \times e^{-t_{Si}\mu_{Si}(E)} \times [1 - e^{-t_{Sense}\mu_{Si}(E)}]$$

Where

$PQE(E)$  = Quantum efficiency at energy  $E$

$t_{Al}$  = Thickness of Al dead layer

$\mu_{Al}(E)$  = Linear attenuation coefficient of Al at energy  $E$

$t_{SiO_2}$  = Thickness of  $SiO_2$  dead layer

$\mu_{SiO_2}(E)$  = Linear attenuation coefficient of  $SiO_2$  at energy  $E$

$t_{Si}$  = Thickness of Si dead layer

$\mu_{Si}(E)$  = Linear attenuation coefficient of Si at energy  $E$

$t_{Sense}$  = Thickness of sensing layer

Eq 3.15

The first measurements of large area APD X-ray PQE over a wide energy range were made at Leicester using the JET-X test facility. Figure 3.21 shows a typical set of measurements. Our model of APD PQE has been compared with this data by allowing the layer thicknesses to vary and finding the best match with a  $\chi^2$  test. The curve shown is the one with the lowest value of  $\chi^2$ . All but the lowest energy data point (0.677 keV) are in good agreement with one another. This data point is suspect because the X-ray peak (677 eV) was partially obscured by the noise (700 eV). For this reason it has not been used in the fitting process. This reasoning applies to all APDs analysed in this thesis. Eight data points were used for the fit and there are 4 model parameters, giving 4 degrees of freedom. The box below the graph gives details of the best fit model parameters and one sigma error ranges.

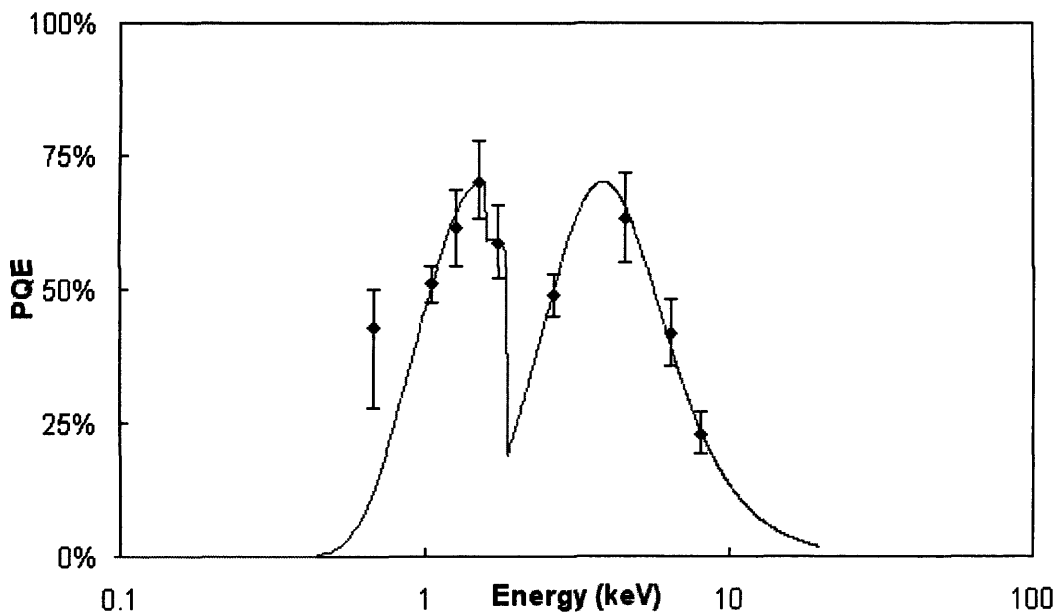
At low energy, PQE values are low because most photons are absorbed in the dead layers, but as energy rises the X-rays become more penetrating and PQE increases to 70% at 1.487 keV. At 1.562 keV (the Al absorption edge), the light filter suddenly becomes more opaque and QE drops. At 1.84 keV (the Si absorption edge) the Si and  $SiO_2$  dead layers become more opaque and QE drops again. After these drops QE rises once more as the X-rays become more and more penetrating. At around 4 keV, PQE gains from dead layer transparency become less important than losses from increasing sensing layer transparency and PQE begins to fall.

The best fit values of the PQE model parameters are all broadly consistent with the values that were expected. However, the error ranges on many of the parameters are very large

indeed, in particular those of the silicon and silicon dioxide dead layer thicknesses. These two layers perform the same function in the model: they attenuate low energy X-rays and reduce low energy PQE. Furthermore the absorption properties of these two materials are very similar. This creates a situation where it is hard to distinguish the effect of one from another, leading to the large uncertainties seen here. This leads us to conclude that it is not justifiable to include both layers in the model and the SiO<sub>2</sub> layer (the thinner of the two) has been removed.

The Aluminium light filter that was deposited onto the APD's front surface was applied using the coating system belonging to the micro-channel plate group at Leicester. This system is calibrated to an accuracy of approximately 5%. Therefore, the fitting process can further be constrained by insisting that the Al layer depth must lie between 0.19 and 0.21 microns.

**Figure 3.21: Peak Quantum Efficiency of APD 116**



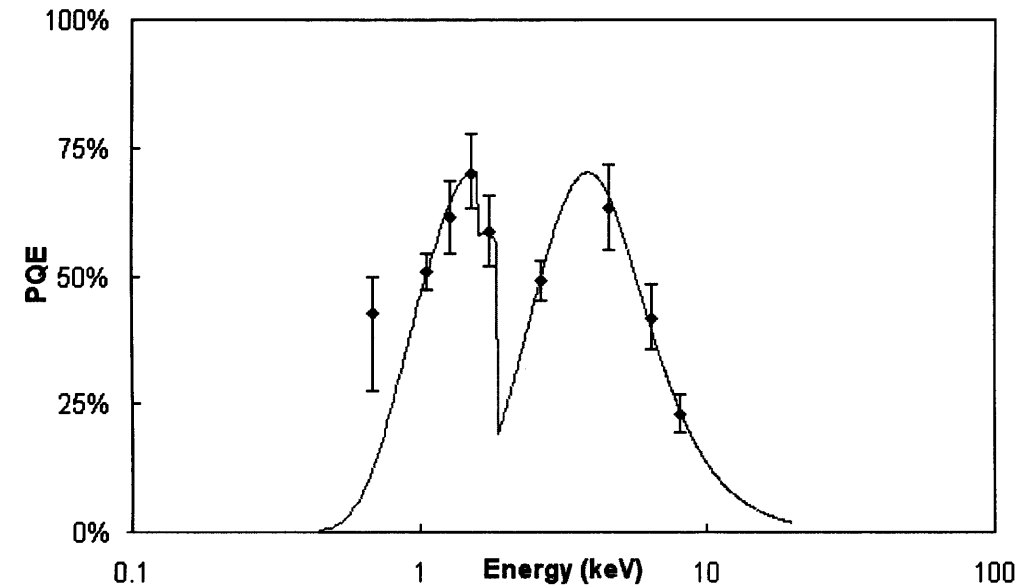
APD Gain = 97  
Bias = 1519 Volts

Best fit values of PQE model parameters:

tAl	= 0.2 +0.9/-0.2 microns	(expected: 0.2 microns)
tSiO2	= 0.0 +0.7/-0.0 microns	(expected: ≈0.1 microns)
tSi (dead)	= 2.0 +0.9/-1 microns	(expected: ≈1 microns)
tSi (sense)	= 20 +10/-4 microns	(expected: <40 microns)
Reduced Chi Squared = 0.14		

The model has been re-fitted to the data with these two adaptations and the results are shown in figure 3.22. This adaptation of the model produces a lower value of reduced chi squared.

**Figure 3.22: Peak Quantum Efficiency of APD 116 using adapted model**



```

APD Gain = 97
Bias      = 1519 Volts

Best fit values of PQE model parameters:
tAl       = 0.19          microns (constrained: 0.19→0.21 microns)
tSi (dead) = 2.0 +0.7/-0.6 microns (expected: ≈1          microns)
tSi (sense) = 20 +11/-8   microns (expected: <40          microns)
Reduced Chi Squared = 0.11

```

The thickness of the silicon dead layer is now better constrained and is of the order of a micron, as expected. The thickness of the sensing layer is slightly less well constrained than before, but it is still consistent with our expectation of <40 microns.

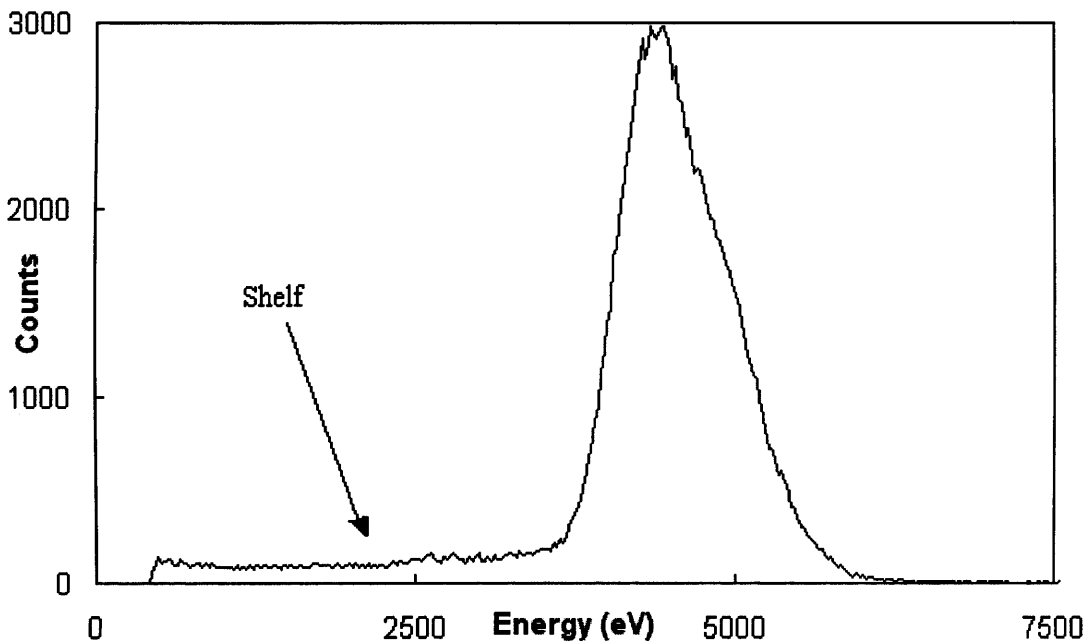
Looking again at figure 3.22, the agreement between the data points and the model appears to be very good. Indeed, the deviation between the two is always much smaller than the associated error bar, a fact that is reflected in the low value of reduced chi squared. It may seem surprising, then, that the errors associated with the fitted parameters  $t_{\text{Si}(\text{dead})}$  and  $t_{\text{Si}(\text{sense})}$  are so large. The reason for this is that only the first few data points are really sensitive to  $t_{\text{Si}(\text{dead})}$ , and only the last few data points are really sensitive to  $t_{\text{Si}(\text{sense})}$ . This means that the model can stray quite far from the optimum values before reduced chi squared increases significantly. For example: consider increasing  $t_{\text{Si}(\text{sense})}$  from its optimum value. This causes a deviation of model from data for the 3 highest energy data points only, giving rise to a new contribution to chi squared. The lower energy data points (ie: the majority) have been much less effected by the change, so the average increase in chi squared is small. This is the reason

for the large errors. The problem could be rectified by the inclusion of many more data points. This could be achieved by studying APDs with a synchrotron source. However, this work is sufficient for our present purpose: increasing our understanding of APDs and using that knowledge to calibrate CATSAT's SXR to study GRBs.

### 3.6 The “shelf” in APD pulse height distributions

APD pulse height distributions contain a region to the left of the main peak with relatively few counts per channel. This is known as the shelf. An example is shown below in figure 3.23.

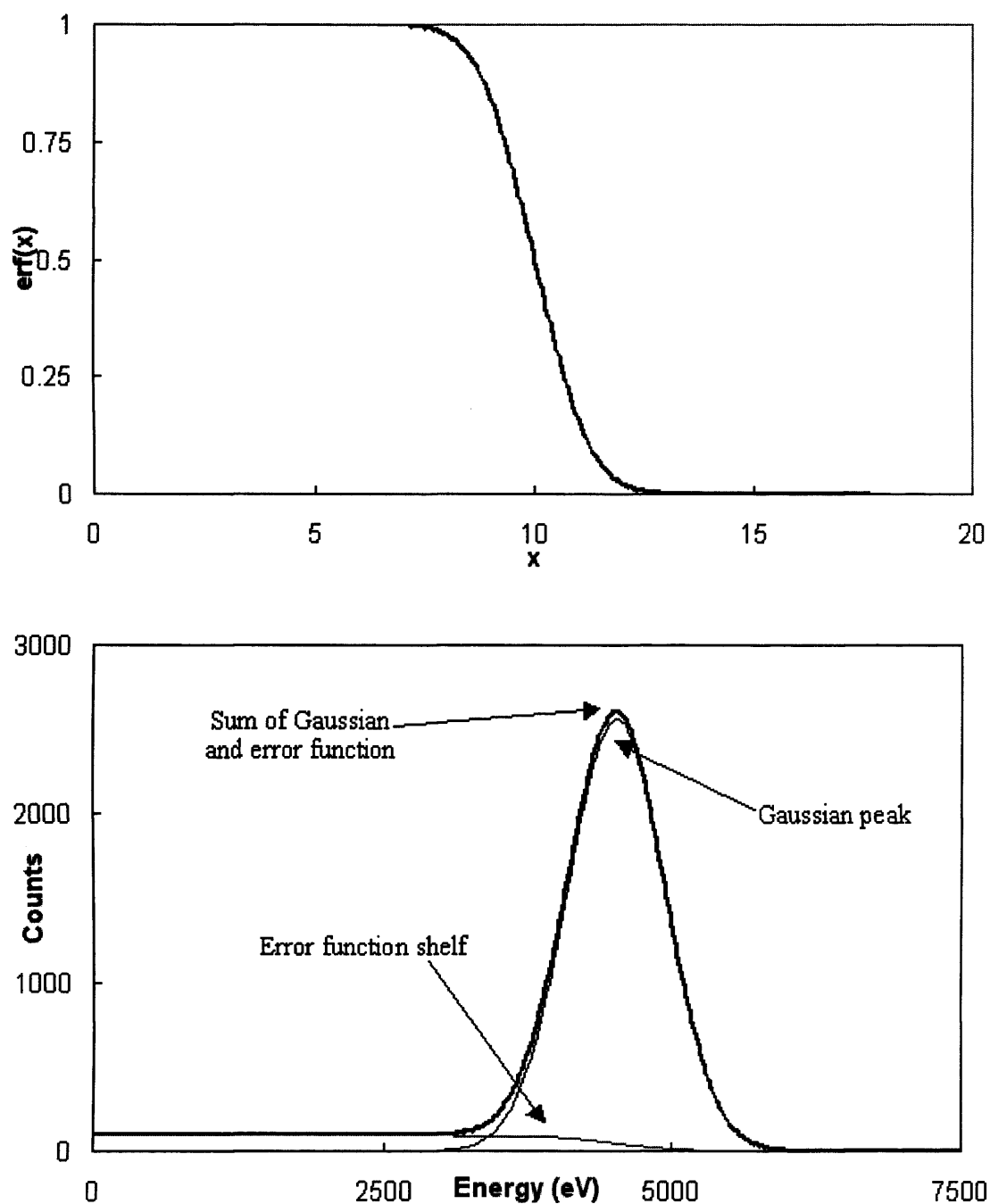
**Figure 3.23: An APD pulse height distribution including a shelf (recorded from APD 69R at an energy of 4.51 keV)**



As has already been stated, the counts that make up the shelf are X-ray generated. For convenience, the shape of the shelf has been parameterised thus: the number of shelf counts in a given channel is proportional to the total number of counts in the peak to the right of that channel, where the constant of proportionality is the same for all channels. This results in a shelf shape that is the same as the error function, or  $\text{erf}(x)$  as shown in figure 3.24. This shape has been adopted because it represents the observed shape of the shelf and is not based on any physical theory of detector mechanisms. Once this shape has been adopted, the problem then becomes one of predicting the value of the constant of proportionality for any energy.



**Figure 3.24: The shape of the error function and the way it contributes to the overall model of pulse height distribution shape**



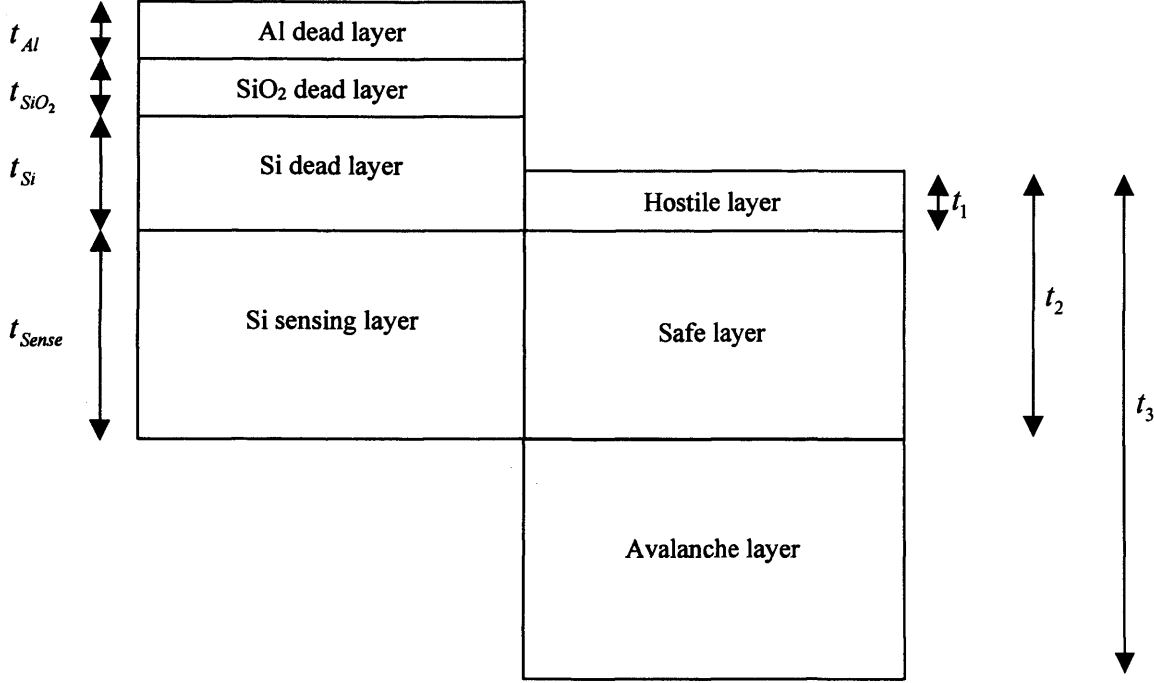
Previously it had been suggested (Forrest 1995) that shelf counts originated in the silicon dead layer of the device; X-ray interactions here would produce charge clouds that would be only partially collected, resulting in reduced pulse heights. However, this model met with very limited success in explaining the relative sizes of the shelf and the main peak as a function of energy (Forrest 1995, Table 4-2).

I have produced a more detailed model to explain the origin of the shelf, consisting of three physical layers:

1. The hostile layer ( $0 < \text{depth} < t_1$ ). This thin layer lies at the back of the silicon dead layer in our PQE model. Some photoelectrons deposited in this part of the detector are collected, but not all, giving rise to smaller events in the pulse-height distribution than expected. So photons absorbed here appear in the shelf.
2. The safe layer ( $t_1 < \text{depth} < t_2$ ). This is a thick layer, which begins after the hostile layer and ends at the start of the avalanche region. All electrons deposited here are collected and see the full gain of the device. So, photons that interact here appear in the main peak. This is the same layer as the sensing layer in the PQE model.
3. The avalanche layer ( $t_2 < \text{depth} < t_3$ ). This is also a thick layer, which starts at the front of the avalanche region and ends at the back. Electrons injected in this region are collected, but they see less than full gain. Photons absorbed here appear in the shelf.

Figure 3.25, below, shows how this model lines up with the PQE model.

X-rays that interact in the first or third layers produce shelf counts and those that interact in the second layer produce counts in the main peak of the pulse-height distribution. The peak fraction (PF), then, is the number of photons that interact in layer 2 divided by the total number of X-ray interactions or, equivalently, the number of counts in the peak divided by the total number of counts. At low energies, the PF will be low because a high proportion of interactions will take place in layer 1. As energy increases fewer and fewer photons will be absorbed in layer 1 and more in layer 2, thus the PF will rise. As the photons become more energetic still, fewer X-rays will interact in layer 2 and more in layer 3, reducing the PF once more.

**Figure 3.25: Comparison of PF & PQE models of internal layer structure of APDs**

If the three layer thicknesses are known then it is possible to apply Beer's law again to calculate the PF:

$$PF(E) = \frac{\text{Peak counts}}{\text{All counts}}$$

$$PF(E) = \frac{\text{Interactions in safe layer}}{\text{Interactions in hostile, safe and avalanche layers}} \quad \text{Eq 3.16}$$

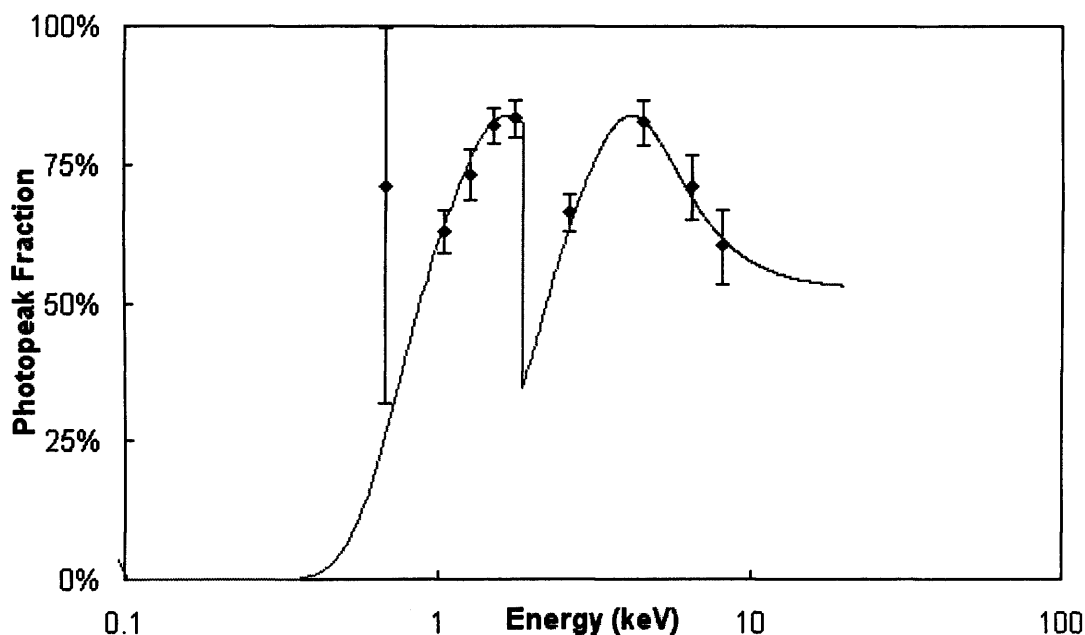
$$PF(E) = \frac{e^{-t_1 \mu_{Si}(E)} - e^{-t_2 \mu_{Si}(E)}}{1 - e^{-t_3 \mu_{Si}(E)}}$$

Figure 3.26 shows a typical set of PF measurements. Our model of APD PF has been compared with the data by allowing the layer boundaries to move and finding the best fit with a  $\chi^2$  test. As with the PQE data, the lowest energy data point does not fit in and has not been used in the fitting process. There are 8 data points to fit to and 3 model parameters, giving 5 degrees of freedom. The shape of the curve follows the general trends outlined above, and has a large step change at the silicon edge. The box below the graph gives details of the best fit model parameters and one sigma error ranges. The best fit PF model parameters suffer from the same insensitivity problem as the parameters of the PQE model, leading to quite large error ranges. Given the relationship between our models of PQE and PF (figure 3.25), we expect that  $t_1 \leq t_{Si(dead)}$  and this is indeed the case. The safe layer is analogous to the sensing

layer in the PQE, so, like the sensing layer, it should be less than 40 microns thick. The best fit value is consistent with this constraint, although the errors are large and the fitted thickness of the safe layer is only marginally consistent with that of the sensing layer. The value of  $t_3$  is equal to the sum of  $t_2$  and the thickness of the avalanche layer. The upper limit on  $t_2$  is 40 microns, as has already been explained (Farrell 1999). At operational gains as low as 100, thickness of the avalanche layer should be less than 50 microns across (Redus et al. 1996). Therefore, we should expect  $t_3$  to be less than 90 microns. This is indeed the case, although the uncertainty in  $t_3$  is large. Prior to this work, the only known photopeak fraction analysis had been performed by Glenn Forrest at the University of New Hampshire (Forrest 1995). Those results are included here as figure 3.27 (cf. figure 3.26).

Figure 3.28 shows the best fit PQE and PPF models side by side on linear and log scales. Again, this work provides important information about APD internal structure as well as a model of APD response to use in CATSAT calibration and flight data analysis.

**Figure 3.26: Peak fraction of APD 116**



```

APD Gain = 97
Bias      = 1519 Volts

Best fit values of PF model parameters:
t1 = 1.4 +0.5/-0.4 microns    (t1 expected: <tSi(dead) )
t2 = 30 +50/-10 microns      (t2 expected: <40 microns)
t3 = 60 +140/-30 microns     (t3 expected: <90 microns)
Reduced Chi Squared = 0.22

```

**Figure 3.27: Photofraction measurements made by Glenn Forrest at the University of New Hampshire (Forrest 1995, Figure 3-15). This graph re-produces the original, but here the energy axis has been made logarithmic to enable comparisons with figure 3.25 above.**

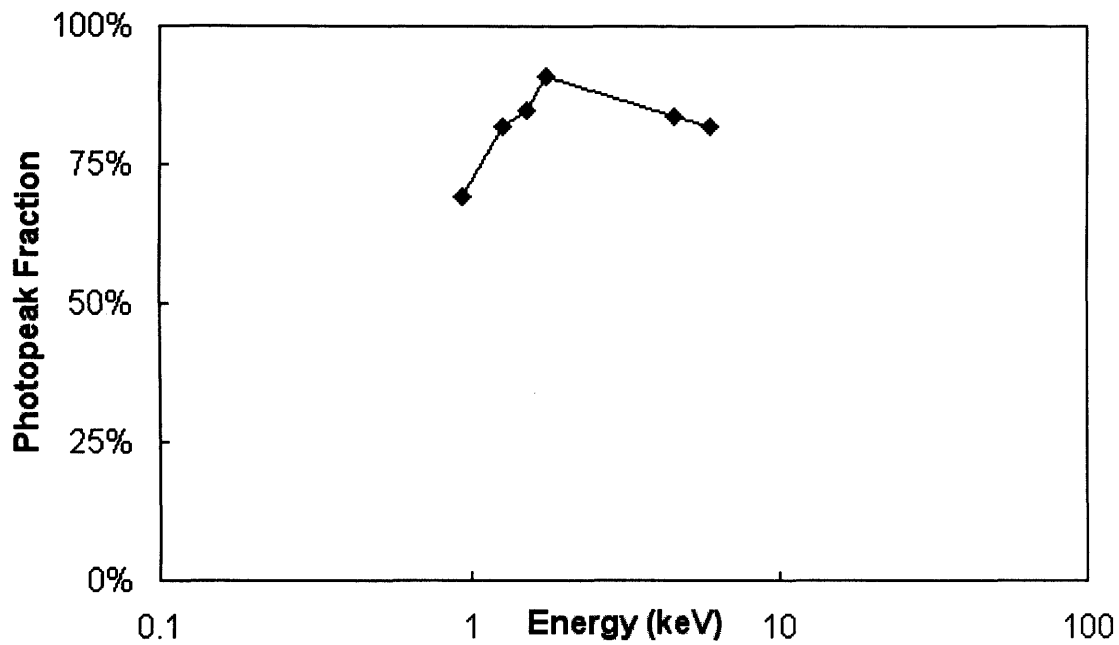
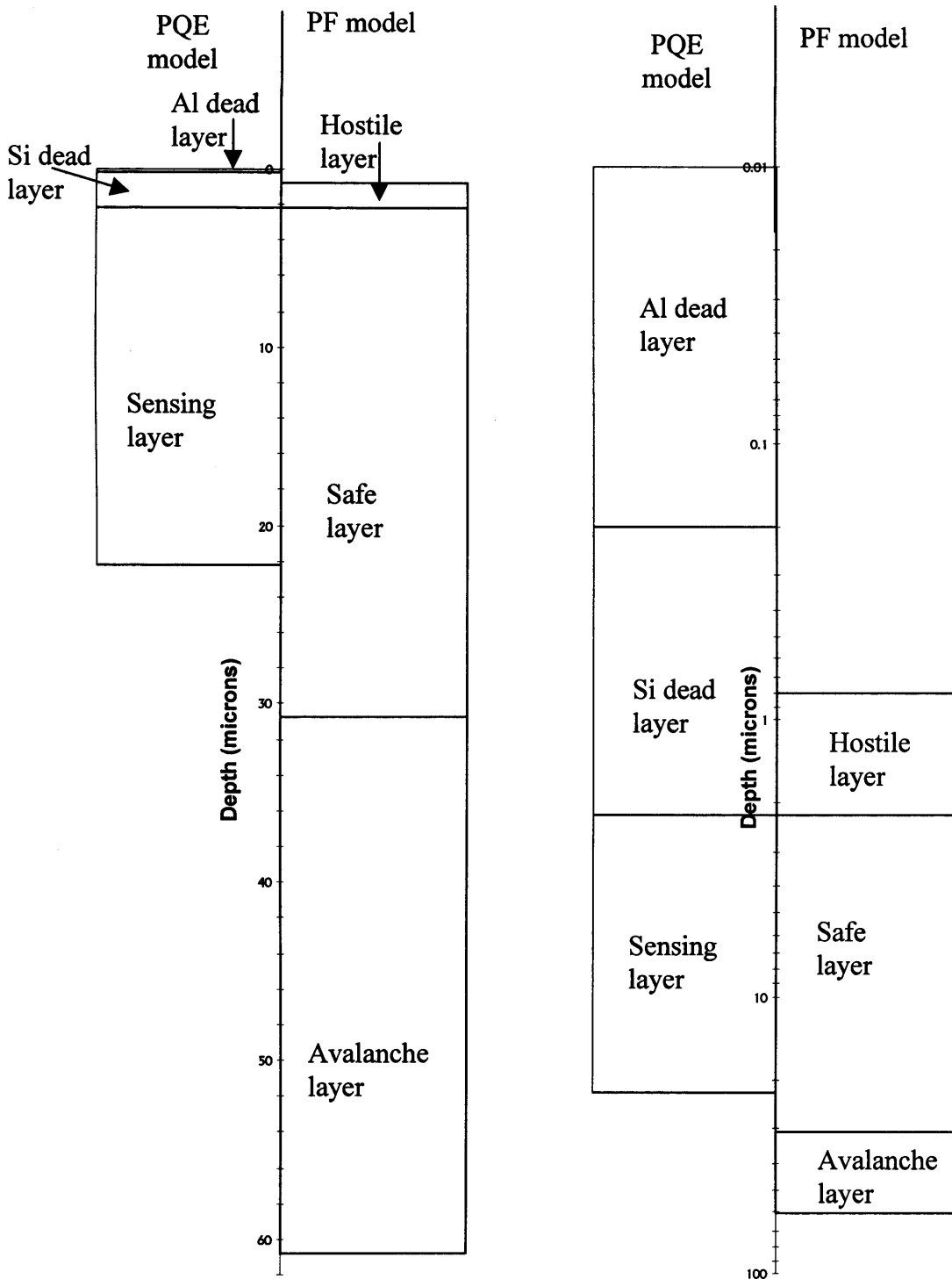


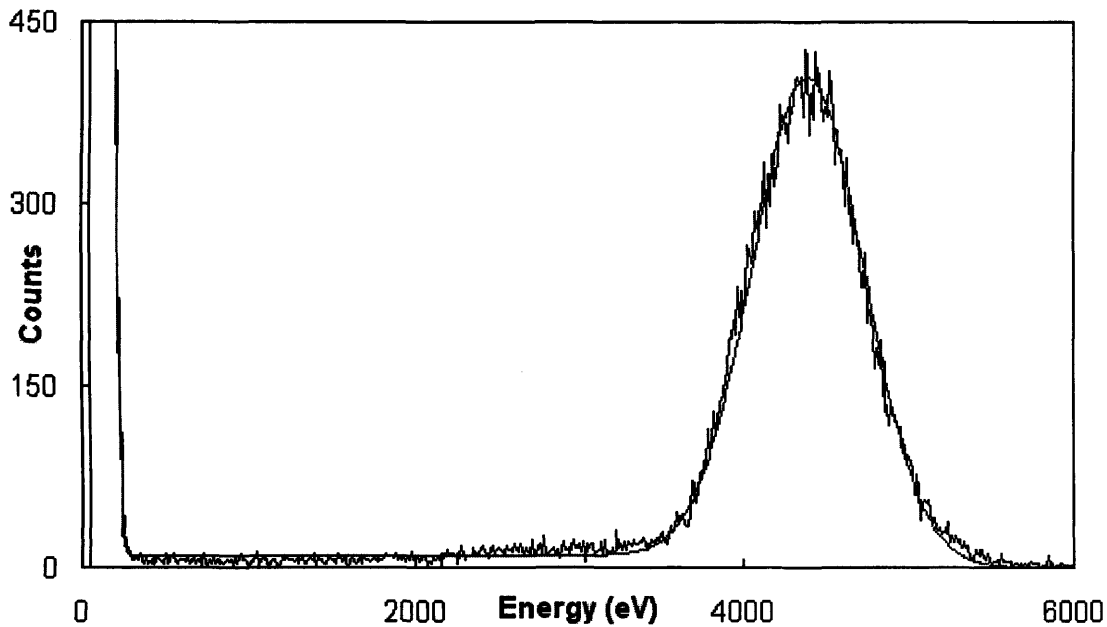
**Figure 3.28: Comparison of best fit PQE and PF models. The figure on the left plots PF & PQE models on a linear scale whilst the figure on the right uses a log scale**



### 3.7 Asymmetric peaks in APD pulse height distributions

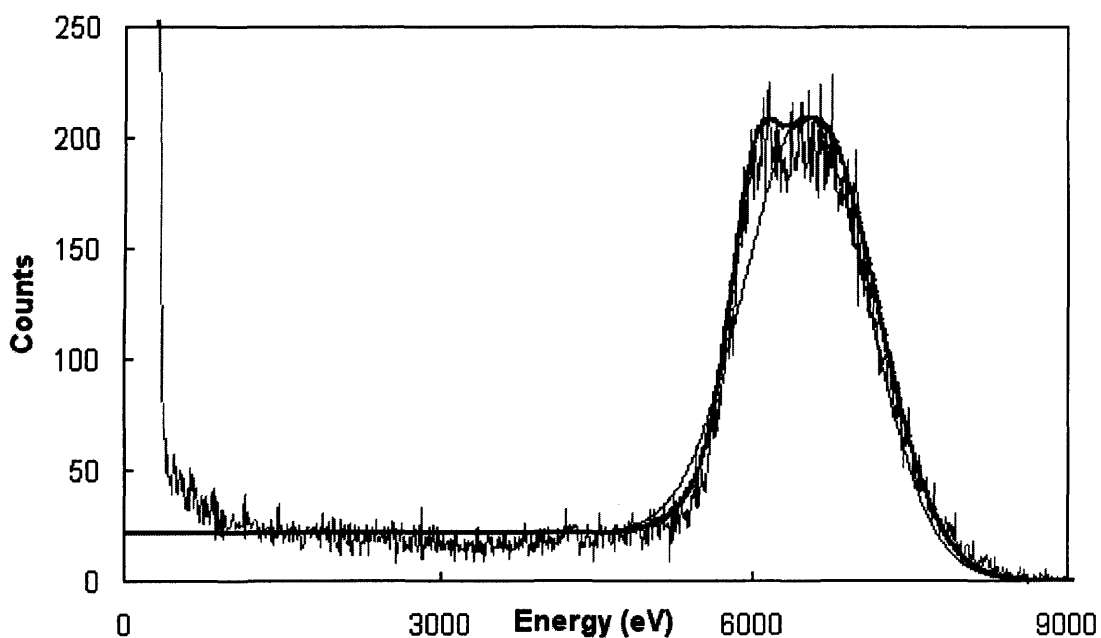
Some APDs produce a pulse height distribution with a peak that is well described by a single, symmetrical Gaussian like that in figure 3.29.

**Figure 3.29: The response of APD 86 at 4.51 keV: A simple Gaussian peak**



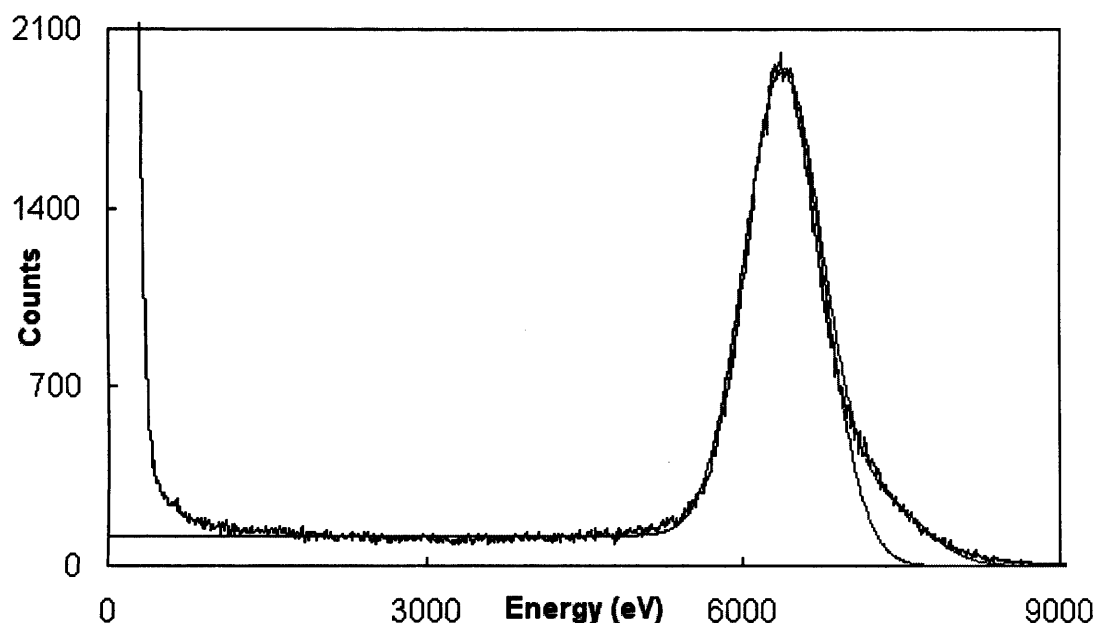
In this case the single peak model and the data overlap convincingly. However, for the majority of APDs the observed response is more complicated. Specifically, the main peak is not wholly described by a single Gaussian. One such device is number 48, whose response is shown below in figure 3.30, along with single and double Gaussian response functions.

**Figure 3.30: The response of APD 48 at 6.4 keV. This device has a peak that is better described as the sum of 2 Gaussians (bold) than as a single Gaussian (faint)**



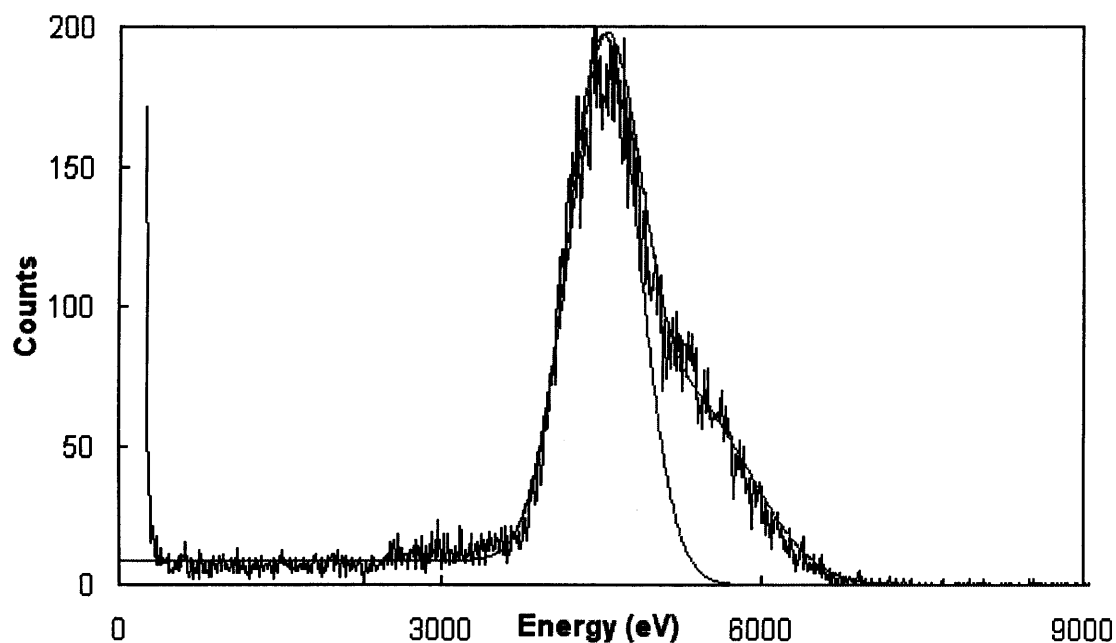
Devices 23 and 61 are also poorly described by a single Gaussian peak as shown in figure 3.31 & figure 3.32.

**Figure 3.31: The response of APD 23 at 6.4 keV. This device also has a 2 Gaussian peak.  
In this case the right hand Gaussian is much smaller.**



The peaks in the pulse height distributions in figures 3.31 and 3.32 are both far better described as the sum of two Gaussians rather than as a single Gaussian. This cannot be accounted for by the presence of  $k_{\beta}$  X-ray lines: they could not be resolved at all by an APD.

**Figure 3.32: The response of APD 61 at 4.51 keV. Again, a 2 Gaussian peak is necessary.**





Perhaps the most obvious response to this phenomenon is to suggest that different physical regions of the diode have different gains. In order to test this hypothesis, researchers at RMD and UNH measured the gains of different parts of an APD by scanning a small spot of light across a device. They found only insignificant gain variation (Farrell et al. 1995, Forrest 1998) hence this mechanism was rejected. Other mechanisms that were suggested all proposed the existence of a more complex layer structure within APDs. However, all of these models predicted that asymmetry ought to undergo a step change at the silicon edge, which, despite many attempts, was never observed. Ultimately, the only option remaining was to seek to replicate the results of Farrell and Forrest in the X-ray regime. A small mask (a circular aperture of diameter 0.95 mm) was scanned across APD #5 and a pulse height distribution was recorded at each location. The X-ray energy used was 6.4 keV. The resulting individual pulse height distributions were found to be symmetrical. Furthermore, the peaks were significantly narrower than ever observed before from a CATSAT APD: FWHM/centroid  $\approx 9\%$ , compared with 14% for the left-hand side of the peak from the diode as a whole. Most significantly, peaks from different parts of the diode had different centroids, indicating different gains. The maximum gain recorded from any area was 108, whilst the lowest was 83: this represents a variation of 25%. Figure 3.33 shows the APD's gain as a function of position. The sum of the many pulse height distributions recorded in this way was found to be approximately the same as a pulse height distribution recorded from the whole diode (figure 3.34) i.e.: the observed variations in gain were sufficient to create the observed asymmetry.

These observations explain peak asymmetry and also indicate that even in diodes that appear to be symmetrical, spectral resolution is dominated by gain variations. One possible reason for the failure of previous attempts to detect gain non-uniformity is that they scanned much smaller portions of the device.

The most likely explanation for variations in gain across the surface of a device is non-uniformity of the doping profile across the device. Previous numerical simulation (Redus et al. 1996) has indicated that avalanche gain may be very sensitive to doping profile and that inhomogeneities in the doping material could cause point to point fluctuations in the gain.

**Figure 3.33: A gain map of APD #5. The gain in the centre of the device was only 83, whilst the gain in the top-right hand corner was 108.**

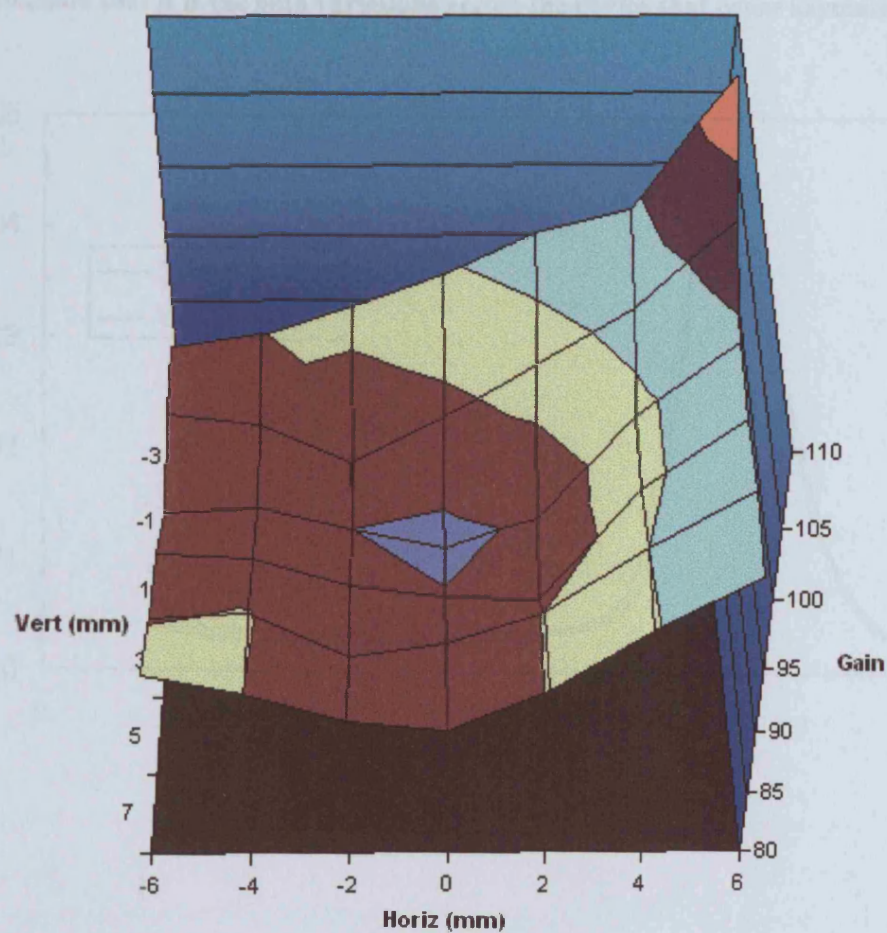
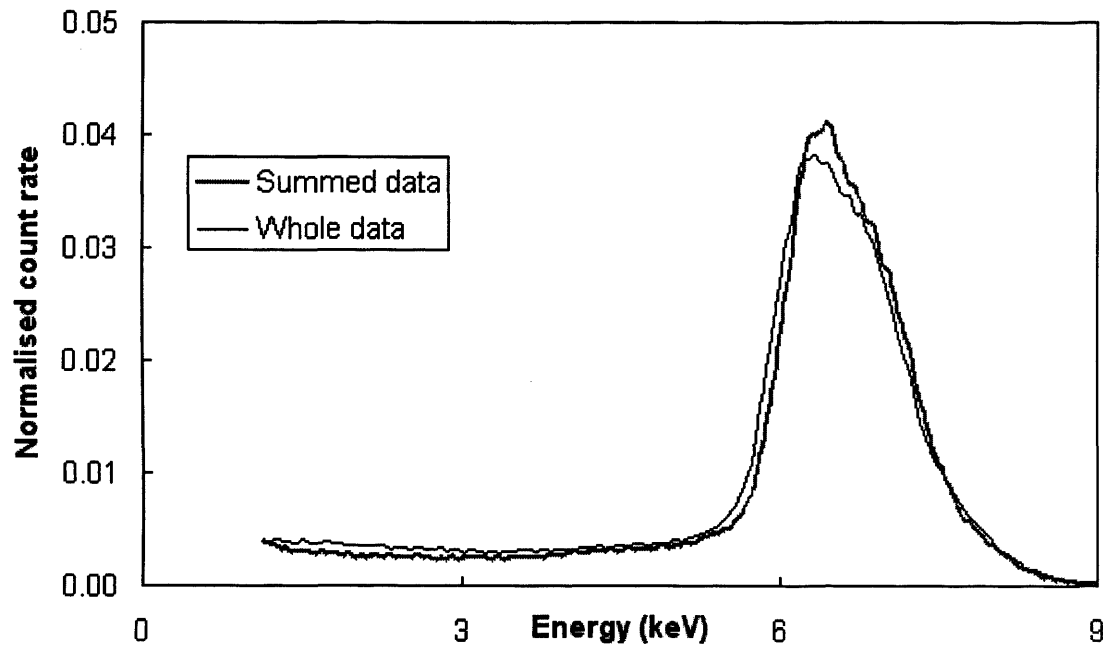


**Figure 3.34: The result of summing spectra from the many parts of APD 5 and also a spectrum recorded from the whole diode at once. These plots are so similar as to indicate that it is the gain variations across the device that cause asymmetry**



## Chapter 4

# Calibration and assembly

The process of producing the SXR flight panels from CATSAT's stock of APDs can be broken down into four steps:

- The devices must all been screened to reject those that are faulty and to measure the performance of those that work.
- The functional diodes must be grouped according to their performance to maximise SXR performance as a whole.
- Each group of diodes then needs to be aluminised before being assembled into an SXR panel together with the relevant high voltage and amplifier electronics.
- The resulting panel must then be calibrated, to allow data returning from CATSAT after launch to be correctly interpreted.

This chapter addresses each of these stages in turn.

### 4.1 APD screening

CATSAT's stock of APDs totals 143, most of which have been in storage at UNH for approximately 2 years. During this period they have undergone no testing at all, making it necessary to screen the devices upon arrival at Leicester. To this end, APDs have been temporarily fitted, 16 at a time, into flight panels and mounted into the JET-X test facility (described in chapter 3), which was evacuated overnight to  $\approx 4 \times 10^{-5}$  mbar. Cooling to  $-40^\circ\text{C}$  took approximately 90 minutes. The bias on each diode was then increased gradually over the next 3 hours up to a limit of 1600 volts, but never to the extent that breakdown was induced. Not all of the devices worked. Those that were non-functional exhibited one these symptoms:

- Unable to take any bias at all without breaking down.
- Able to take some bias, but not enough to achieve any avalanche gain and allow X-rays to be seen.
- Able to take enough bias to produce low gains but not enough to produce  $G=100$ .
- Able to produce  $G=100$ , but noise threshold is too high ( $>>1$  keV).
- Unable to see X-rays at all.

104 of the 143 diodes did not exhibit these symptoms and these were exposed to 8 keV and 4.5 keV X-rays whilst in the test facility. Two important properties were recorded with each device to provide data for the APD grouping programme: the low energy noise threshold of the device and the width of the 8 keV Copper X-ray line. The whole screening process took approximately 2 months.

## 4.2 APD grouping

When 16 APDs are assembled into an SXR panel, the output from the 16 separate pre-amplifier chains is irreversibly summed and a low-level discriminator is used to reduce the noise. There is only one discriminator per panel and its levels must reject noise from the noisiest device in the panel. As a result, in a panel with 15 quiet diodes and one noisy diode, the threshold setting would inadvertently reject perfectly good low energy data from the 15 good devices. In order to prevent this sort of data loss, we have decided to group APDs in particular panels according to their noise thresholds.

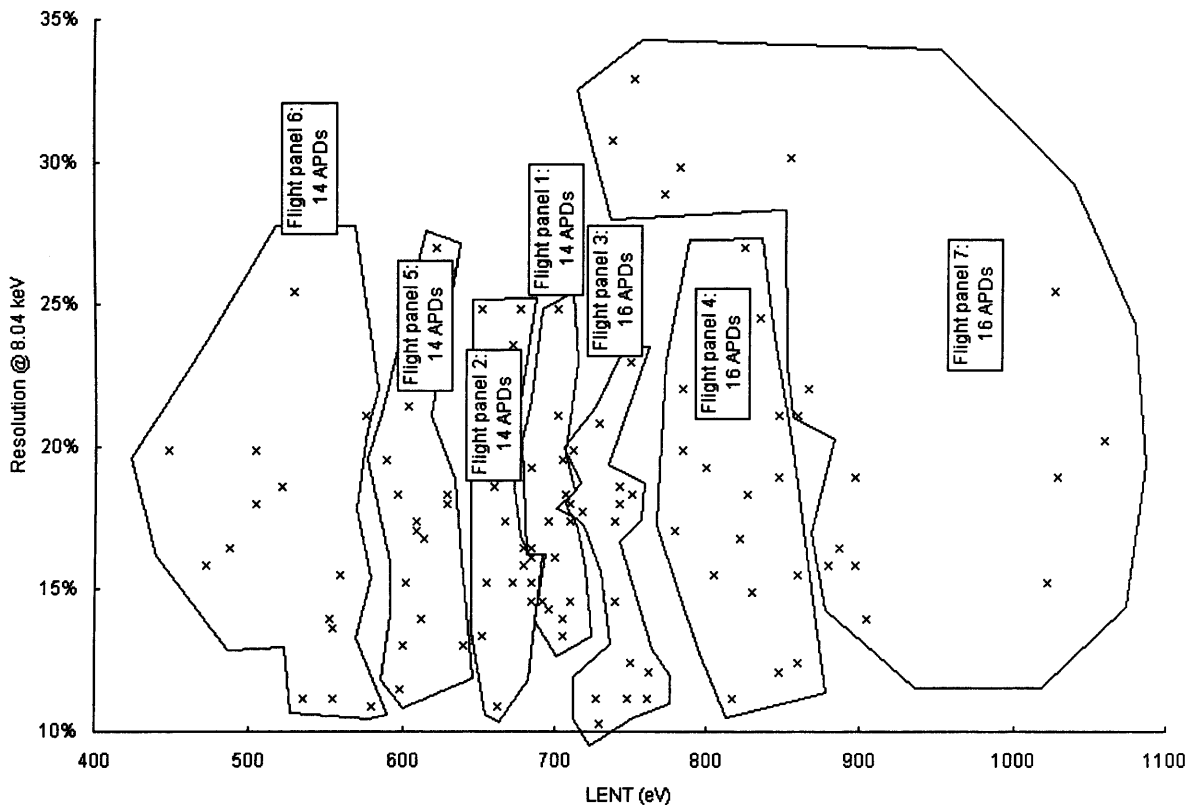
When the output of 16 APDs is summed, the resulting X-ray line width will be between the best and worst of the 16 individual devices. In a panel containing 16 APDs whose line widths span a wide range, the output spectrum may have a line width much greater than that produced by the best diode in the panel, resulting in degradation of spectral resolution. For this reason, we have decided to use resolution as a secondary grouping property where a choice exists between devices with identical noise thresholds. Chapter 3 described how the resolution of an APD is dominated by gain variations across the area of the device. This effect is more noticeable at higher energies, where it is not masked by other peak-broadening mechanisms like Poisson statistics, which are more important at lower energies. Therefore the resolution measurements used for grouping were made at the highest energy we could achieve: 8 keV.

Figure 4.1 shows a scatter plot of the 104 flight diodes; Low Energy Noise Threshold (LENT) (eV) is used as the ordinate and resolution at 8 keV (%) is used as the abscissa. The figure also shows how the diodes have been allocated to the seven panels of the SXR. In general, the

APDs have been sorted by noise threshold first and resolution second as discussed above. These criteria were over-ridden in the case of group seven, which has been allocated some APDs with exceptionally poor resolution, which would otherwise have been allocated to groups 3 & 4. The purpose in this was to keep the range of resolutions in groups 3 and 4 in line with those of groups 1, 2, 5 & 6, i.e.: from 10% to 27%. This intervention has resulted in an increase in the noise threshold of groups 3 & 4, but only a very small one ( $\approx 10$  eV).

The SXR has 7 panels each requiring 16 APDs, making a total requirement of 112 APDs. Since only 104 of the available 143 devices are functional, CATSAT will be launched with 8 empty APD sockets. Two each of these "holes" have been allocated to panels 1, 2, 5 & 6, while panels 3, 4 & 7 have no holes. This allocation is accidental: when SXR assembly began (with panel 1) every panel was to have had two blanks, but after panel 1 had been completed 6 more functional diodes were purchased, whose operational characteristics placed them in groups 3, 4 & 7.

**Figure 4.1: A scatter plot of CATSAT's flight APDs according to their noise threshold and resolution. The seven groups of diodes are shown and labelled.**



### 4.3 Aluminising and assembly

Aluminising takes place in a coating system, consisting of a large vacuum tank, in which up to 28 APDs can be suspended face-down over a heating element loaded with Aluminium rods. When the heater is turned on, the aluminium evaporates and some is transferred onto the APDs. The deposited thickness is measured using a commercial quartz crystal monitor system.

After they are aluminised, the APDs are transferred to a large, nitrogen-filled glove-box for assembly into an SXR panel.

### 4.4 Calibration

It is necessary to know the behaviour of the peak centroid, peak width, peak fraction and peak quantum efficiency as a function of energy. The first two have been found to be linear with energy, hence, in principle, only 2 measurements are needed of each property. The last two properties have been found to be well described by the models presented in chapter 3. These are more complicated models with more degrees of freedom. Therefore, more data points have been gathered in order to constrain the parameters. As shown in figure 3.20 & figure 3.21, nine X-ray lines have been used, covering the energy range 677 eV  $\rightarrow$  8040 eV. Each of these lines was observed for a sufficient period to provide 10 000 counts in each APD. A full calibration procedure is included as appendix A.

#### 4.4.1 Asymmetry and Calibration

As discussed in chapter 3, gain variations across an APD give rise to asymmetry in the peak in the pulse height distribution. However, it is desirable to use a simpler model for calibration: a single, symmetric gaussian peak. The X-ray spectral fitting package XSPEC (Arnaud ) has been used to analyse the systematic errors introduced when a single gaussian response function is used in fitting a GRB model to data recorded by devices with a double peaked response. Firstly, it was necessary to create two XSPEC compatible response function files: one to represent a panel of double-peaked APDs and the other to represent the single-peaked approximation. APD number 48 was at one time the most obviously double peaked device at Leicester and so it was selected as the starting point for these files. A double-peaked function was fitted to the count spectrum in figure 3.29 and then the centroids and standard deviations of the two peaks were assumed to vary linearly with energy. Relative weightings were assumed to be constant. Similarly, a single-peaked response function was fitted to the same data set. In both cases, the area of the device was scaled up by a factor of sixteen to represent an entire SXR panel.

This analysis was performed before the full development of Peak Fraction (PF) and Peak Quantum Efficiency (PQE) models and used a slightly simpler approach. Firstly, PF was assumed to be constant at around 70% (from the data in figure 3.29). Secondly, QE was defined as the likelihood of an X-ray being detected at all, anywhere in the pulse-height distribution. This simplified QE model was fitted to data taken from APD 48 resulting in a 0.59  $\mu\text{m}$  SiO<sub>2</sub> dead layer and a 48  $\mu\text{m}$  Si detection layer. A 1500 Å Al dead layer was added to this model to represent the light filter before it was used to calculate the QE for both response files.

The recent model of Hasinger (1996) was used to predict the soft X-ray background flux. In the region of the spectrum 0.1 keV to 100 keV, this model consists of three components: a plasma (kT  $\approx$  0.215 keV), another plasma (kT  $\approx$  0.086 keV), and a Bremsstrahlung component (kT 38 keV).

A "standard" Gamma-ray Burst was selected to predict GRB count rates: GRB 870521. Of all the GRBs observed in the soft X-ray regime by GINGA (Strohmayer et al. 1998), this has the best signal to noise ratio in the SXR's energy range. Since this burst has the highest statistical quality, this is the one that ought to best show up flaws in the calibration. Like almost all GRBs this burst was well described by the Band model (Band et al. 1993):

$$\begin{aligned} \text{When } E \leq (a-b)E_0 \quad N(E) &= A \left( \frac{E}{100 \text{ (keV)}} \right)^a e^{-\frac{E}{E_0}} \\ \text{When } E \geq (a-b)E_0 \quad N(E) &= A \left[ \frac{(a-b)E_0}{100 \text{ (keV)}} \right]^{a-b} e^{b-a} \left( \frac{E}{100 \text{ (keV)}} \right)^b \end{aligned}$$

For GRB 870521:

$$\begin{aligned} A &= 101.0 \text{ photons/s/cm}^2/\text{keV} \\ a &= 0.822 \\ b &= -2.12 \\ E_0 &= 2.38 \text{ keV} \end{aligned} \quad \text{Eq 5.1}$$

In each simulation run, the first step was to take the X-ray background (XRB) photon spectrum and use it to simulate the background count spectrum in the panel, by folding it through the double-peaked response and adding the appropriate counting statistics.

Figure 4.2a shows the 3 components of the X-ray background (XRB) spectrum and their sum. Figure 4.2b shows the output count spectrum this gave rise to, given a ten-minute integration. The data have been re-binned according to a scheme by Dr Forrest in which bin widths increase linearly with energy.



**Figure 4.2a: The 3 components of the spectrum of the X-ray background and their sum. The two plasma components die away around 1 keV leaving only the Bremsstrahlung.**

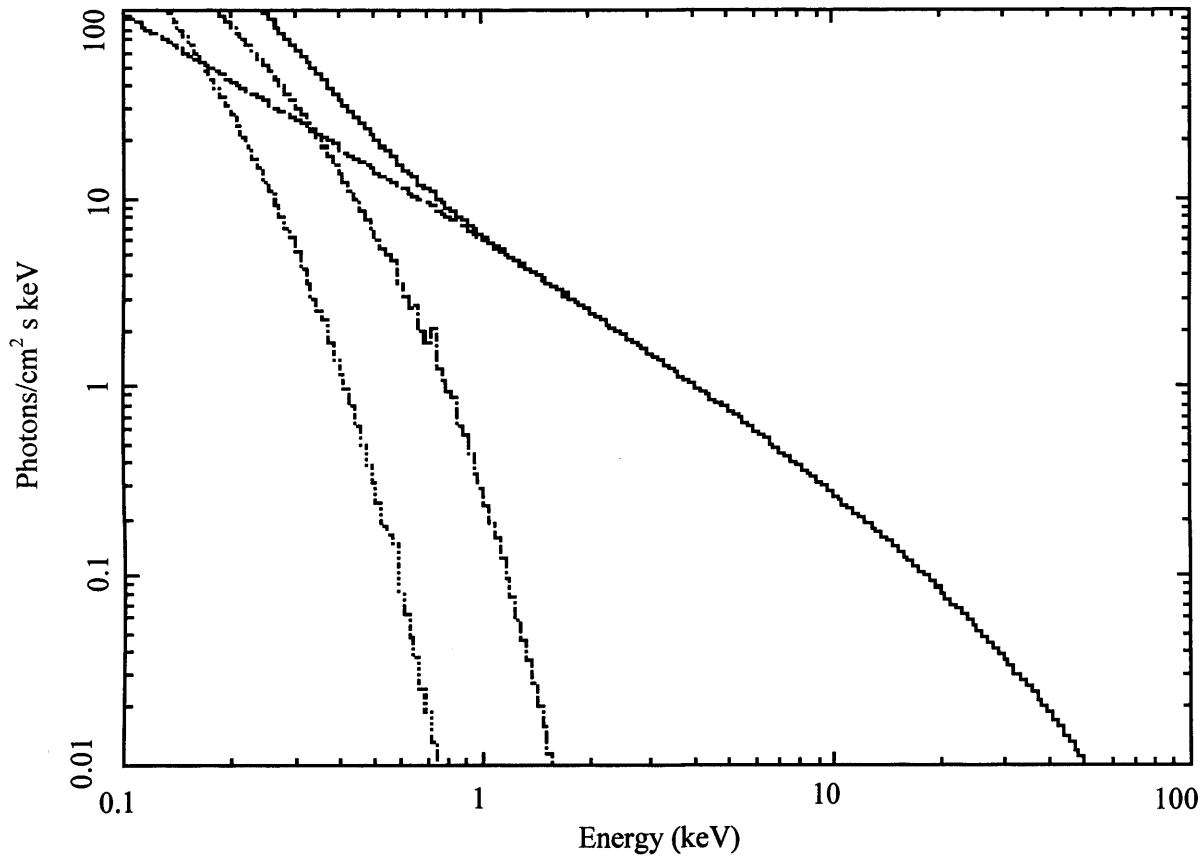
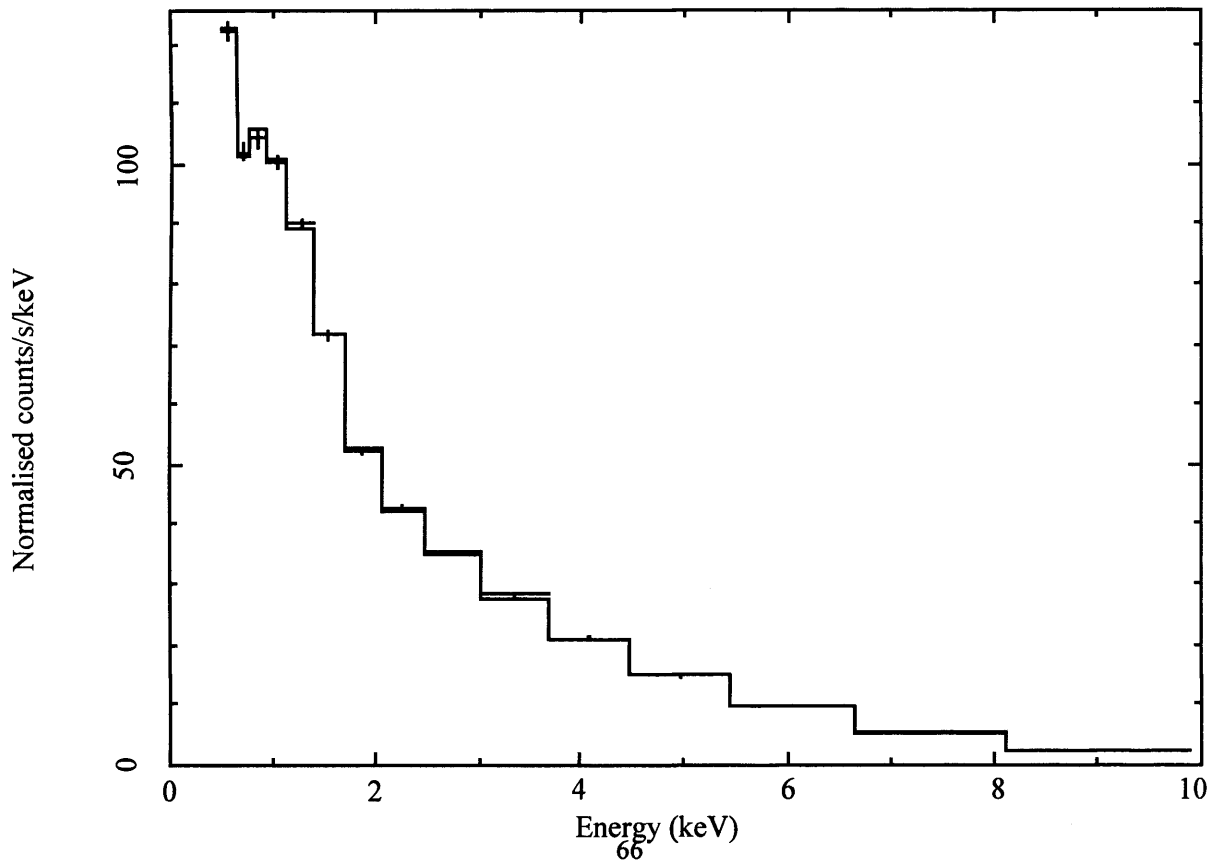


**Figure 4.2b: The resulting count spectrum in a panel of identical double-peaked APDs.**



Next, the photon spectrum of GRB 870521 was folded through a photoelectrically absorbing hydrogen column of density  $n_H = 0.0 \times 10^{22} \text{ cm}^{-2}$  (i.e.: zero), added to the background spectrum and a second output count spectrum was produced, again using the double peaked response.

Figure 4.3a shows the XRB spectrum with the added GRB spectrum. Figure 4.3b shows the simulated observation of this event. This represents an integration of 48 seconds, the recorded duration of this burst in the GINGA data set. Once again, counting statistics have been added and the data have been re-binned.

The third step was to attempt to fit the XRB model to the simulated XRB data assuming no prior knowledge, still using the double peaked response. The fourth step was to attempt to fit the GRB model to the simulated GRB data using the result of step three to account for the XRB and still using the double peaked response. This process produced a set of best fit GRB parameters. By repeating steps 3 & 4 with the single peaked response it was possible to obtain a second set. These two sets could then be compared to look for systematic errors introduced by using the single peaked response.

Table 1 shows the results from ten runs as described above. Each of these runs used the same model parameters and response matrices; the differences between the results arise purely from the counting statistics of the simulated data. The first column shows the number of that run. The next 5 show the best-fit values of the GRB parameters when using the double-peaked response, starting with the 90% confidence range for  $n_H$ . The other model parameters were not sufficiently constrained by the data to allow XSPEC to calculate confidence intervals, only best fit values. The seventh column gives the value of reduced chi squared that these values achieved and the eighth column indicates whether or not XSPEC required any human intervention in the fitting, for instance to manually seek a better starting point for the fitting process. The next seven columns provide the same data for the fitting process using the single-peaked approximation. Notice that the runs are not listed in numerical order, but are ranked according to column 13, the best-fit normalisation factor found when using the single-peaked response. The reason for this will be discussed later. This simulation process was then repeated for input hydrogen column densities of  $0.1 \times 10^{22} \text{ cm}^{-2}$ ,  $1.0 \times 10^{22} \text{ cm}^{-2}$  and  $50.0 \times 10^{22} \text{ cm}^{-2}$ . The results of these repeats are shown in tables 2, 3 and 4. Special attention was paid to the case of  $n_H = 1.0 \times 10^{22} \text{ cm}^{-2}$  since this is the order of magnitude of column density we hope to see.

Once CATSAT is in orbit, observations of burst spectra by the HXR and DGS (see chapter 2) will complement SXR data and will help to constrain A, b and  $E_0$ . This will improve our

**Figure 4.3a: The X-ray background, the spectrum of GRB 870521 and their sum. The GRB spectrum rises between 0.1 and 5 keV, before falling again.**

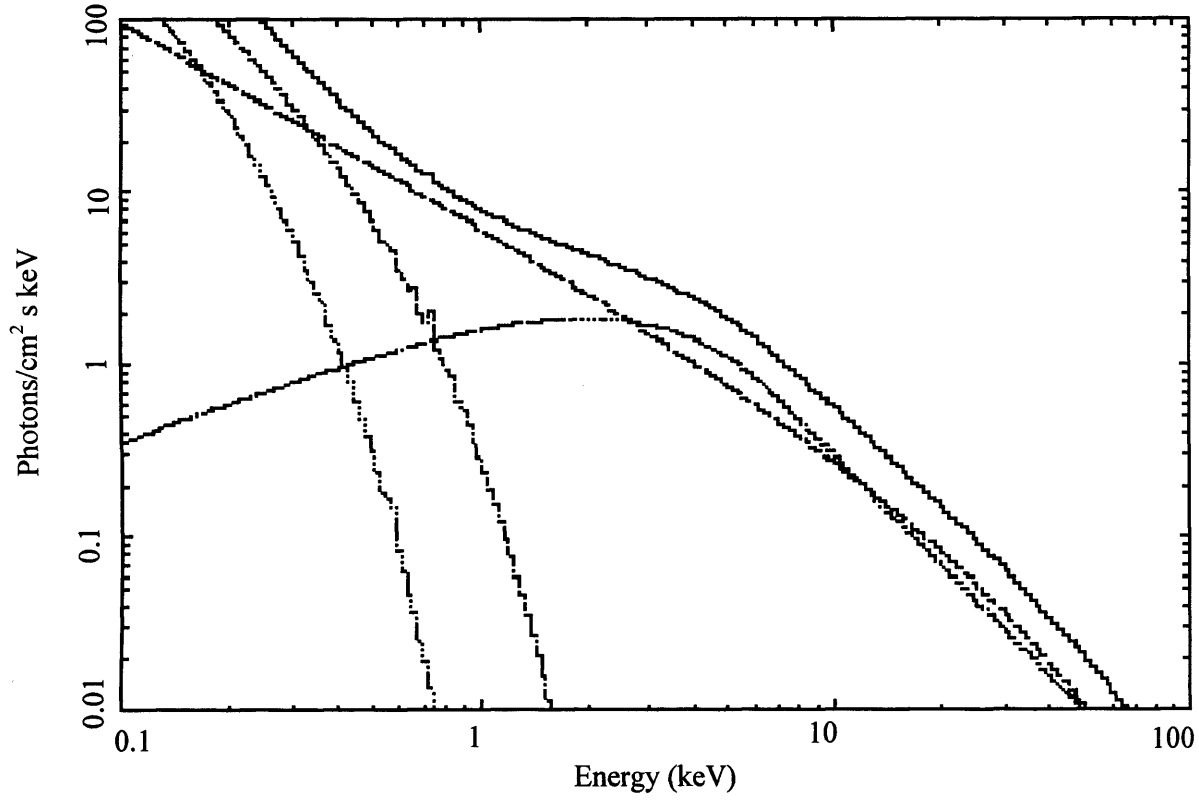
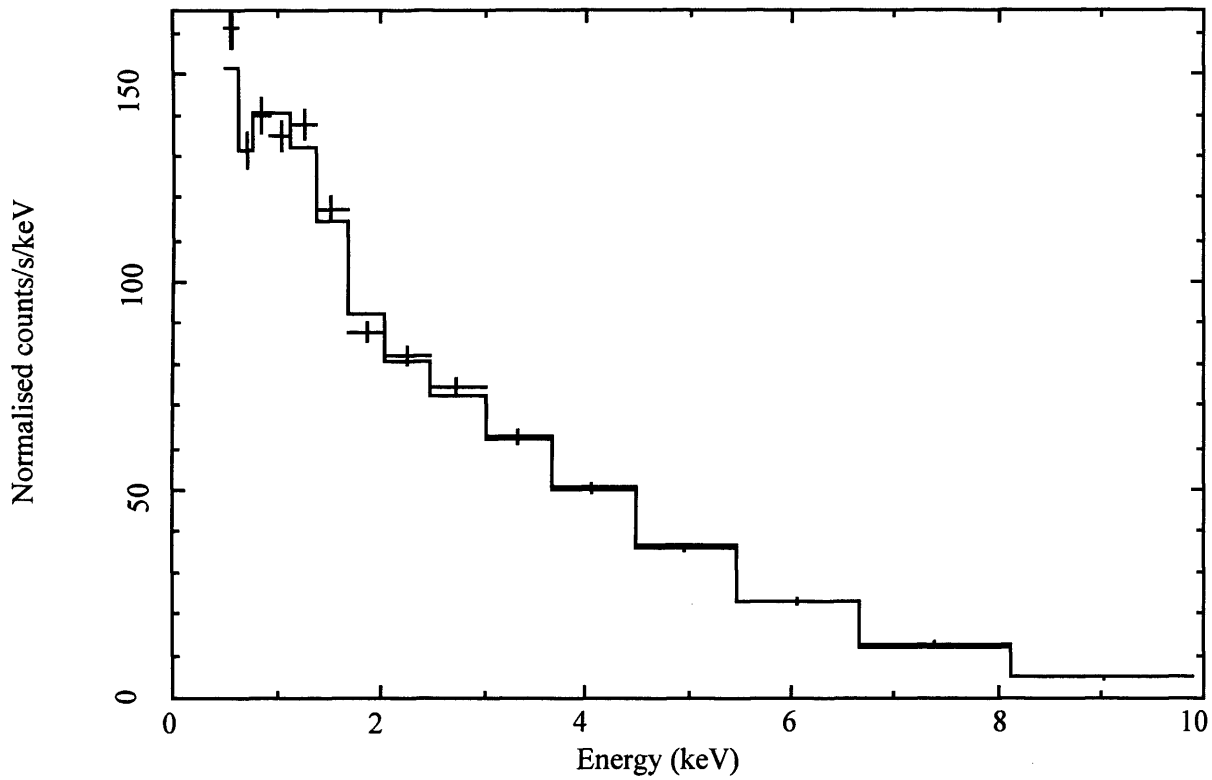


**Figure 4.3b: The resulting count spectrum in a panel of identical double-peaked APDs.**



ability to fit  $a$  and  $n_H$  using SXR data. Therefore, a further simulation was performed for the special case of  $n_H = 1.0 \times 10^{22} \text{ cm}^{-2}$ , with the parameters  $A$ ,  $b$  and  $E_0$  fixed at their correct input values. The results of this work are shown in table 5. Notice that in this case XSPEC is able to provide confidence intervals for  $a$  as well as  $n_H$ . Figure 4.4 shows the contours of the chi-squared landscape in  $n_H$ - $a$  parameter space when fitting with the double response. These contours correspond to regions of 10%, 68%, 90% and 99% confidence. In the centre of these regions is the best-fit location marked with a cross. Figure 4.5 shows the same landscape after fitting with the single-peaked response.

Table 1  
Results of fitting to GRB 870521 with  $nH = 0.0E+22 /cm^2$

Run	Result of Fitting With Double Response								Result of Fitting With Single Response							
	nH (10 <sup>22</sup> cm-2)	a	b	Eo (keV)	A (ph/s/cm2/keV)	R	Chi Sq	Help?	nH (10 <sup>22</sup> cm-2)	a	b	Eo (keV)	A (ph/s/cm2/keV)	R	Chi Sq	Help?
48	<b>0.055-&gt;0.53</b>	<b>0.0</b>	<b>-9.9</b>	<b>3.9</b>	<b>3.99</b>	<b>0.6</b>	<b>N</b>		<b>0.042-&gt;0.40</b>	<b>0.0</b>	<b>-9.8</b>	<b>3.8</b>	<b>4.24</b>	<b>0.6</b>	<b>N</b>	
45	<b>0.054-&gt;0.50</b>	<b>0.1</b>	<b>-2.9</b>	<b>3.5</b>	<b>6.11</b>	<b>0.9</b>	<b>N</b>		<b>0.084-&gt;0.47</b>	<b>0.1</b>	<b>-2.5</b>	<b>3.5</b>	<b>6.32</b>	<b>0.9</b>	<b>N</b>	
49	0.0001->0.25	0.2	-1.7	3.7	6.80	0.8	Y		0.0001->0.23	0.2	-1.7	3.7	6.55	0.8	Y	
42	0.0001->0.26	0.3	-3.4	3.2	12.68	1.1	Y		0.0001->0.25	0.3	-3.3	3.2	12.71	1.1	Y	
50	0.0001->0.42	0.4	-3.4	2.9	18.09	1.4	N		0.0001->0.39	0.4	-3.2	2.9	18.97	1.4	N	
41	0.0001->0.073	0.5	-10.0	3.0	22.81	1.4	N		0.0001->0.067	0.4	-10.0	3.1	20.24	1.4	N	
46	0.0001->0.21	0.6	-3.3	2.7	40.60	2.2	Y		0.0001->0.21	0.6	-3.3	2.7	39.97	2.2	Y	
43	0.0001->0.23	0.6	-7.7	2.6	52.80	0.7	Y		0.0001->0.21	0.7	-5.1	2.6	53.73	0.7	Y	
44	0.0001->0.12	0.9	-2.2	2.4	119.90	1.8	Y		0.0001->0.12	0.8	-2.2	2.4	106.80	1.8	Y	
47	0.0001->0.095	0.9	-9.9	2.2	167.00	0.9	N		0.0001->0.085	0.9	-4.0	2.3	149.50	0.9	N	

True values:

$nH (10^{22} \text{ cm}^{-2})$       0.0  
 a                              0.822  
 b                              -2.12  
 $E_0 \text{ (keV)}$                 2.38  
 $A \text{ (ph/s/cm}^2/\text{keV)}$     101

Table 2  
Results of fitting to GRB 870521 with  $nH = 0.1E+22 /cm^2$

Run	Result of Fitting With Double Response							Result of Fitting With Single Response								
	nH (10 <sup>22</sup> cm-2)	a	b	Eo (keV)	A (ph/s/cm2/keV)	R	Chi Sq	Help?	nH (10 <sup>22</sup> cm-2)	a	b	Eo (keV)	A (ph/s/cm2/keV)	R	Chi Sq	Help?
26	<b>0.16-&gt;0.59</b>	<b>-0.1</b>	<b>-9.8</b>	<b>4.4</b>	<b>2.9</b>	<b>1.2</b>	<b>N</b>		<b>0.15-&gt;0.56</b>	<b>-0.1</b>	<b>-9.7</b>	<b>4.3</b>	<b>2.9</b>	<b>1.1</b>	<b>N</b>	
27	0.0032->0.73	0.0	-3.2	3.8	4.0	0.4	N		0.0001->0.69	0.0	-3.0	3.8	4.4	0.4	N	
24	0.058->0.45	0.1	-9.5	3.9	5.5	1.3	N		0.048->0.43	0.1	-9.2	3.9	5.9	1.3	N	
22	0.073->0.48	0.1	-3.7	3.6	6.8	0.2	N		0.062->0.45	0.2	-3.5	3.5	7.0	0.2	N	
28	0.0001->0.42	0.4	-1.8	2.8	23.3	0.9	Y		0.0001->0.39	0.4	-1.9	2.9	21.4	0.9	Y	
30	0.0001->0.49	0.8	-2.0	2.3	106.1	0.9	Y		0.0001->0.46	0.6	-2.1	2.5	56.1	0.8	Y	
29	0.0001->0.24	0.8	-2.1	2.4	104.7	1.3	Y		0.0001->0.22	0.9	-2.1	2.4	125.8	1.2	Y	
21	0.0001->0.31	1.1	-2.2	2.2	246.0	0.9	Y		0.0001->0.26	1.1	-2.2	2.1	313.2	0.9	Y	
25	0.0001->0.15	1.3	-2.4	1.9	777.2	2.0	Y		0.0001->0.13	1.3	-2.4	1.6	639.6	2.1	Y	
23	0.0001->0.27	1.3	-2.0	1.8	770.5	1.5	Y		0.0001->0.26	1.3	-2.0	1.8	771.9	1.5	Y	

True values:

$nH (10^{22} \text{ cm}^{-2})$       0.1  
 a                              0.822  
 b                              -2.12  
 $E_0 \text{ (keV)}$                 2.38  
 A (ph/s/cm<sup>2</sup>/keV)      101

Table 3  
Results of fitting to GRB 870521 with  $nH = 1.0E+22 \text{ /cm}^2$

Run	Result of Fitting With Double Response							Result of Fitting With Single Response								
	nH (10 <sup>22</sup> cm-2)	a	b	Eo (keV)	A (ph/s/cm2/keV)	R	Chi Sq	Help?	nH (10 <sup>22</sup> cm-2)	a	b	Eo (keV)	A (ph/s/cm2/keV)	R	Chi Sq	Help?
15	0.58->2.36	0.0	-10.0	3.9	4.3	0.4	N		0.53->2.23	0.1	-10.0	3.7	5.6	0.4	N	
7	0.55->2.75	0.0	-9.3	3.8	3.8	1.7	N		0.49->2.57	0.1	-9.8	3.6	5.6	1.8	N	
11	0.28->2.10	0.1	-10.0	3.8	5.0	0.8	N		0.23->1.95	0.2	-9.8	3.5	7.9	0.8	N	
18	0.32->1.92	0.3	-2.0	2.9	15.1	1.1	N		0.55->1.83	0.3	-2.0	2.8	18.6	1.1	N	
1	0.36->1.87	0.4	-4.6	2.9	20.6	0.6	N		0.32->1.77	0.4	-4.4	2.9	23.4	0.5	N	
8	0.29->2.04	0.4	-2.0	2.7	25.8	0.9	N		0.24->1.91	0.5	-2.0	2.6	35.2	0.9	N	
19	0.51->1.46	1.6	-1.9	1.6	2818.0	0.7	Y		0.65->2.05	0.5	-2.1	2.6	37.3	0.7	N	
17	0.19->1.43	0.7	-10.0	2.7	57.7	0.4	N		0.16->1.34	0.7	-9.8	2.7	63.0	0.4	N	
4	0.23->1.60	1.4	-2.0	1.9	906.6	1.0	Y		0.20->1.56	0.7	-2.1	2.6	70.6	1.0	N	
5	0.23->1.89	0.8	-3.5	2.5	90.5	1.6	N		0.20->1.77	0.8	-10.0	2.4	105.5	1.6	N	
6	0.21->1.27	0.9	-4.0	2.3	142.9	1.8	N		0.19->1.22	0.9	-9.4	2.3	141.8	1.9	N	
10	0.55->1.93	1.1	-2.3	2.0	355.4	1.3	N		0.51->1.92	1.0	-2.3	2.1	276.3	1.4	N	
2	0.22->1.77	1.0	-5.5	2.2	213.2	0.9	N		0.18->1.61	1.1	-3.8	2.1	341.0	0.9	N	
9	0.35->1.74	1.3	-1.7	1.8	976.2	0.5	Y		0.32->1.25	1.4	-1.7	1.7	1183.0	0.5	Y	
16	<b>0.037-&gt;0.76</b>	<b>1.5</b>	<b>-1.9</b>	<b>1.8</b>	<b>1690.0</b>	<b>1.2</b>	<b>Y</b>		<b>0.015-&gt;0.48</b>	<b>1.6</b>	<b>-1.9</b>	<b>1.7</b>	<b>2675.0</b>	<b>1.2</b>	<b>Y</b>	
20	<b>0.0001-&gt;0.80</b>	<b>1.4</b>	<b>-1.5</b>	<b>2.0</b>	<b>888.7</b>	<b>1.0</b>	<b>Y</b>		<b>0.0001-&gt;0.55</b>	<b>1.7</b>	<b>-1.5</b>	<b>1.8</b>	<b>2806.0</b>	<b>1.0</b>	<b>Y</b>	
13	0.10->1.07	1.7	-9.1	1.8	2996.0	1.0	Y		<b>0.067-&gt;0.65</b>	<b>1.7</b>	<b>-10.0</b>	<b>1.8</b>	<b>2907.0</b>	<b>1.0</b>	<b>Y</b>	
12	0.051->1.04	1.5	-3.8	1.9	1442.0	1.7	Y		<b>0.050-&gt;0.66</b>	<b>1.7</b>	<b>-2.1</b>	<b>1.8</b>	<b>2943.0</b>	<b>0.6</b>	<b>Y</b>	
14	0.051->1.04	1.5	-3.8	1.9	1.5	1.7	Y		<b>0.050-&gt;0.657</b>	<b>1.7</b>	<b>-2.1</b>	<b>1.8</b>	<b>2943.0</b>	<b>1.6</b>	<b>Y</b>	
3	<b>0.0001-&gt;0.38</b>	<b>1.9</b>	<b>-1.7</b>	<b>1.7</b>	<b>5947.0</b>	<b>1.1</b>	<b>Y</b>		<b>0.0001-&gt;0.31</b>	<b>1.9</b>	<b>-1.8</b>	<b>1.7</b>	<b>5988.0</b>	<b>1.1</b>	<b>Y</b>	

True values:

$nH (10^{22} \text{ cm}^{-2})$       1.0  
a                              0.822  
b                              -2.12  
 $E_0 \text{ (keV)}$               2.38  
 $A \text{ (ph/s/cm}^2\text{/keV)}$       101

Table 4  
Results of fitting to GRB 870521 with  $nH = 50.0E+22 /cm^2$

	Result of Fitting With Double Response								Result of Fitting With Single Response							
Run	nH (10^22 cm-2)	a	b	Eo (keV)	A (ph/s/cm2/keV)	R	Chi Sq	Help?	nH (10^22 cm-2)	a	b	Eo (keV)	A (ph/s/cm2/keV)	R	Chi Sq	Help?
37	35->85	-2.2	-2.3	3000.0	0.0014	0.4		Y	38->81	-2.9	-3.3	3000.0	0.0003	0.3		Y
40	<b>17-&gt;55</b>	<b>-1.8</b>	<b>-2.0</b>	<b>3000.0</b>	<b>0.0028</b>	<b>1.4</b>		<b>N</b>	<b>18-&gt;43</b>	<b>-1.9</b>	<b>-2.0</b>	<b>3000.0</b>	<b>0.0027</b>	<b>1.4</b>		<b>N</b>
36	32->77	-2.0	-2.0	3000.0	0.0036	1.5		N	32->88	-2.0	-2.0	3000.0	0.0035	1.5		N
33	26->105	-2.0	-2.0	3000.0	0.0038	2.9		Y	26->105	-2.0	-2.0	3000.0	0.0037	2.3		Y
34	27->120	-2.0	-2.0	3000.0	0.0049	2.1		Y	28->120	-2.0	-2.0	3000.0	0.0046	2.1		Y
35	27->130	-2.0	-2.6	3000.0	0.0046	1.0		Y	26->116	-2.0	-2.0	3000.0	0.0049	1.0		N
38	32->89	-1.8	-2.0	3000.0	0.0080	0.8		N	33->105	-1.8	-2.0	3000.0	0.0072	0.8		N
31	20->86	-1.5	-2.0	3000.0	0.0102	1.9		N	20->86	-1.5	-2.0	3000.0	0.0093	1.9		N
32	15->63	-1.2	-2.0	3000.0	0.0200	0.6		N	15->63	-1.2	-2.0	3000.0	0.0186	0.6		N
39	17->98	-1.2	-2.0	3000.0	0.0220	1.0		N	16->72	-1.2	-2.0	3000.0	0.0205	1.0		N

True values:  
 $nH (10^{22} \text{ cm}^{-2})$       50.0  
a                              0.822  
b                              -2.12  
 $E_0 \text{ (keV)}$                 2.38  
 $A \text{ (ph/s/cm}^2/\text{keV)}$       101



Table 5  
Results of fitting to GRB 870521 with  $n_H = 1.0E+22 \text{ /cm}^2$   
(A, E0 & b, constrained by DGS & HXR)

Run	Result of Fitting With Double Response				Result of Fitting With Single Response			
	$n_H (10^{22} \text{ cm}^{-2})$	a	R Chi Sq	Help?	$n_H (10^{22} \text{ cm}^{-2})$	a	R Chi Sq	Help?
61	0.703->1.486	0.802->0.845	0.7	N	0.658->1.412	0.806->0.848	0.6	N
62	0.500->1.106	0.800->0.839	0.9	N	0.465->1.048	0.803->0.842	1.0	N
63	0.822->1.650	0.793->0.836	1.1	N	0.771->1.570	0.797->0.840	1.1	N
64	0.659->1.385	0.793->0.834	0.9	N	0.617->1.313	0.797->0.837	0.9	N
65	0.644->1.411	0.800->0.843	1.4	N	0.598->1.333	0.805->0.846	1.3	N
66	0.607->1.322	0.805->0.846	0.9	N	0.563->1.251	0.809->0.849	0.8	N
67	0.756->1.548	0.799->0.841	0.6	N	0.710->1.473	0.803->0.844	0.6	N
68	0.769->1.545	0.793->0.835	1.1	N	0.723->1.471	0.797->0.838	1.1	N
69	0.574->1.264	0.805->0.846	0.6	N	0.534->1.199	0.809->0.849	0.6	N
70	0.719->1.494	0.806->0.848	0.9	N	0.674->1.424	0.809->0.851	0.9	N

True values:

$n_H (10^{22} \text{ cm}^{-2})$	1.0
a	0.822
b	-2.12
E0 (keV)	2.38
A (ph/s/cm <sup>2</sup> /keV)	101

Since the goal of this analysis was to compare the two methods of deconvolution with one another to determine the efficacy of the simpler method, we firstly compare the fits with one another, rather than with the input model parameter values. The first thing to note is that in general, the two methods of fitting agree very well. Looking through tables 1-4, we see that they achieve similar values of the fitted parameters and of chi squared and require similar levels of human intervention. There is a small overall effect whereby the single-peaked function produces slightly lower values of  $n_H$  than does the double gaussian, but both are usually consistent with the input value.

Comparing now the fitted values with the input values in tables 1-4, there are a few cases (runs: 16, 20, 13, 12, 14, 3, 26, 48, 45 & 40) where one or both of the attempts to fit yields a 90% confidence interval for  $n_H$  which does not include the input value. These runs are shown in the tables in bold italics. These runs are also those where the value in column 13 (the best-fit normalisation factor found when using the single-peaked response) has strayed farthest from the input value (hence the ranking in the tables).

# Chapter 4: Calibration and assembly

Confidence contours for nH & alpha when  
beta, A & EO are constrained (double response)

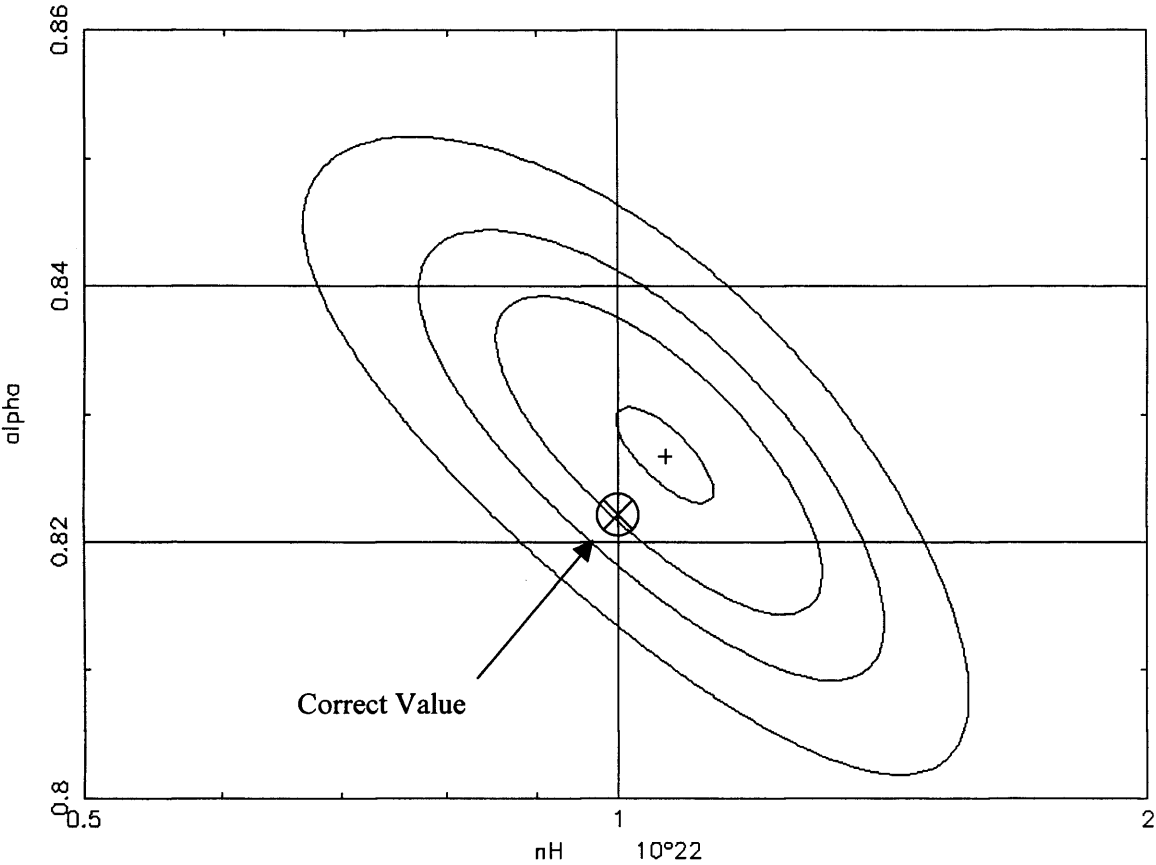
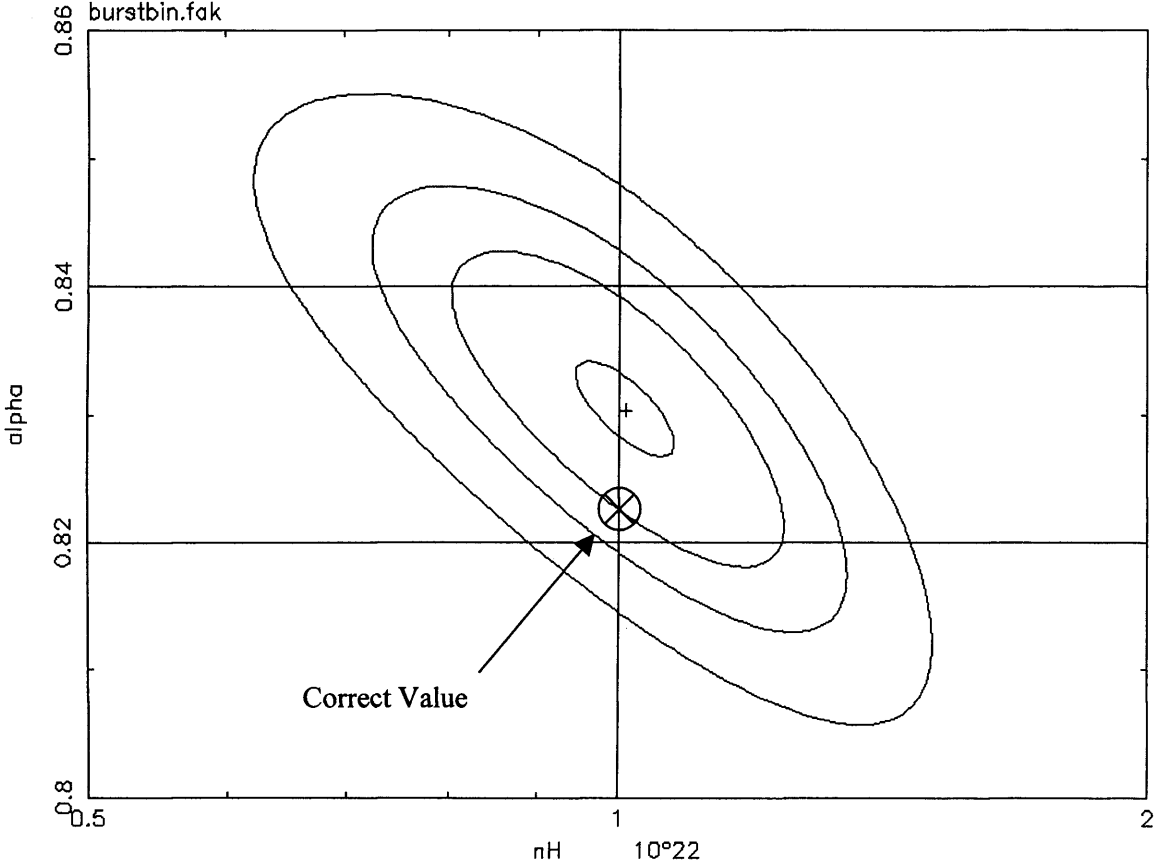


**Figure 4.4 (above): 10%, 68%, 90% & 99% Confidence regions from 2-peaked fitting**

**Figure 4.5 (below): 10%, 68%, 90% & 99% Confidence regions from 1-peaked fitting**

Confidence contours for nH & alpha when  
beta, A & EO are constrained (single response)



If this factor is constrained to a more sensible range, as the DGS and HXR data will do in the real CATSAT, then the fitted 90% confidence region moves and once again surrounds the input value. Looking through the results, it is clear that, for GRB 870521 at least, the SXR on its own is often unable to provide a good estimate of  $A$ .

When  $A$ ,  $E_0$  and  $b$  are fully constrained to their input values, as in table 5, the fitting process is better still. The confidence regions for  $n_H$  are reduced and it becomes possible to provide error estimates for  $a$ . Again, the best fit values of the parameters and the values of chi squared achieved using the 2 fitting methods are similar. There is still a very small effect whereby use of the single-peaked response tends to produce a slightly lower estimate of  $n_H$  and a slightly higher value for  $a$ . Figures 4.4 & 4.5 were produced from the fits in run 70. We can see that the location of the input model parameters lies just inside of the 68% confidence contour for both fits.

These results suggest that it is perfectly acceptable to use a mono-gaussian response function, as the systematic errors introduced are too small to be considered important, given the statistical quality of the data. This finding is of some importance to CATSAT as the requirement for a double gaussian response function would have complicated the calibration process considerably.

## Chapter 5

# Calibration results

The diodes of SXR flight panel one have been calibrated as described in appendix A. This chapter presents the results and then goes on to analyse these in the context of the detector physics.

Figure 5.1 presents the data gathered from the APD occupying socket 'zero' in SXR flight panel one, which corresponded to APD serial number 71R. 5.1a shows how the centroid of the main peak in the pulse height distribution increases with X-ray energy. A straight line fit to this data is shown, determined by linear regression. The gradient and intercept are also shown. Figure 5.1b shows how the standard deviation of the peak,  $\sigma$ , increases with energy. Again, a straight line fit to the data is shown and the gradient and intercept are given. The regression analysis ignored those data points gathered with the soft X-ray source (677 eV, 1.041 keV & 2.622 keV) because that source only illuminates a part of the diode, which would tend to reduce the effect of peak broadening by gain non-uniformity and therefore produce unrepresentatively narrow spectral lines. Lines generated by the kevex source illuminate the whole of the APD, giving true line widths. Figure 5.1c presents the Peak Fraction (PF) data from the device, to which the PF model from chapter three has been fitted. As with the data in chapter three, the lowest energy data point has not been used in PF model fitting. Finally, the figure in the lower right shows the PQE data and the fitted PQE model. Again, the lowest energy data point has not been used in the fitting process. To the right of the figures, the best fit values of the PF and PQE model parameters are given along with their associated errors and the resulting values of reduced chi squared. APD gain, bias and serial number are shown in the lower right hand corner. Figures 5.2 to 5.13 give exactly the same information for the remaining diodes in flight panel one.

Figure 5.1: Calibration data from flight panel 1, channel 0

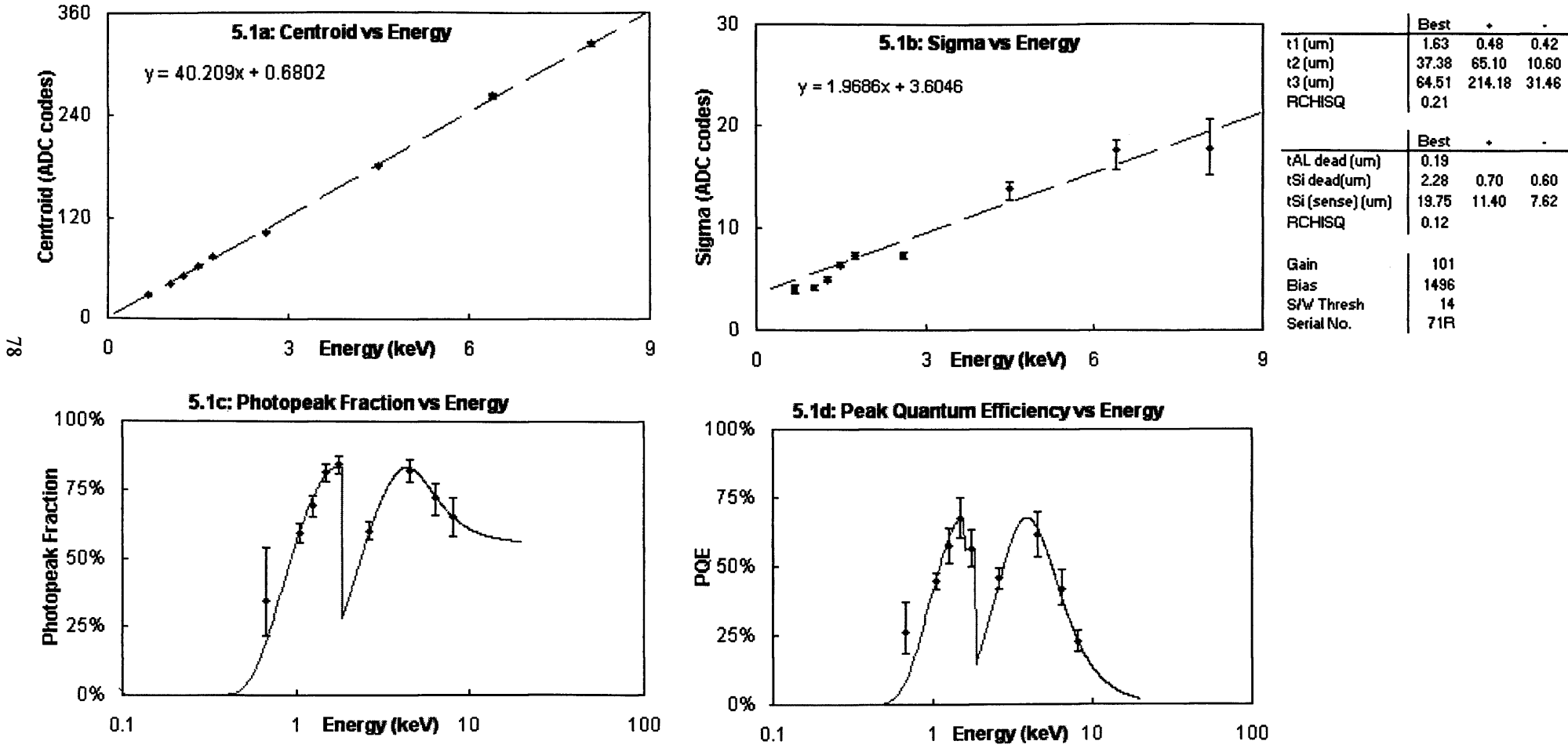
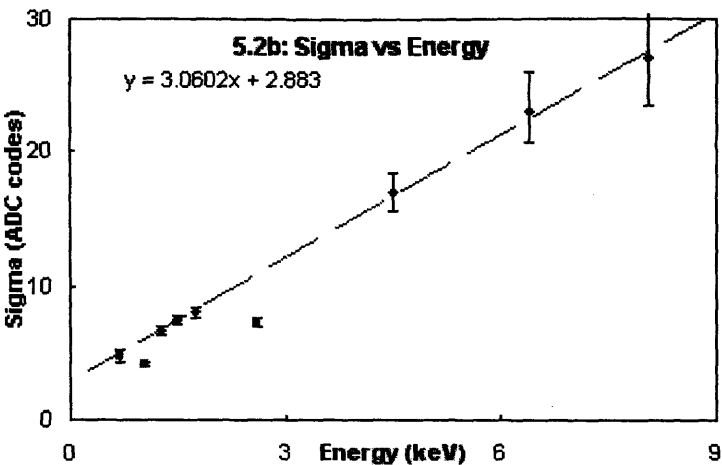
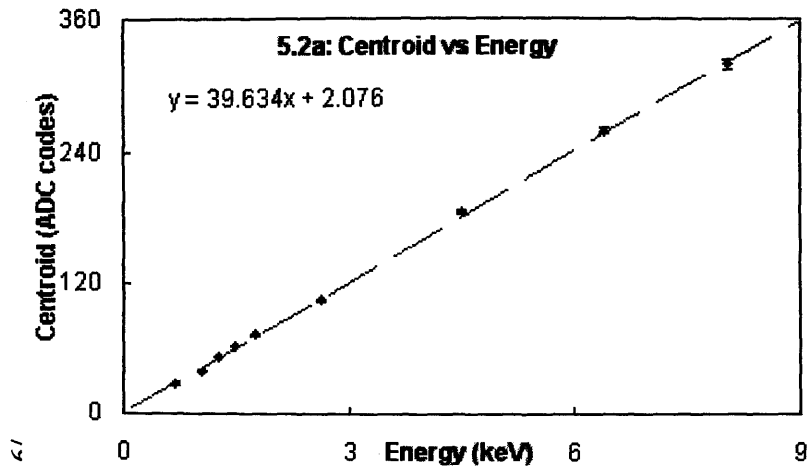


Figure 5.2: Calibration data from flight panel 1, channel 1



	Best	*	-
t1 (um)	1.33	0.42	0.35
t2 (um)	40.77	29.23	12.21
t3 (um)	76.94	8260966257.50	57.76
RCHISQ	0.11		

	Best	*	-
tAL dead (um)	0.20		
tSi dead(um)	2.10	0.69	0.58
tSi (sense) (um)	19.97	11.53	7.75
RCHISQ	0.16		

Gain	99
Bias	1525
S/W Thresh	14
Serial No.	81

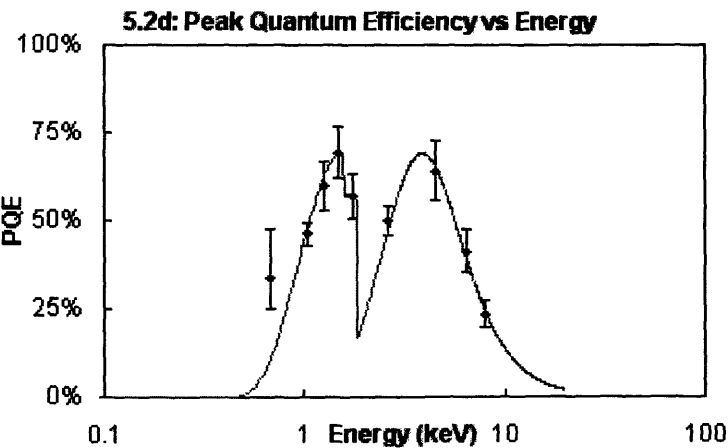
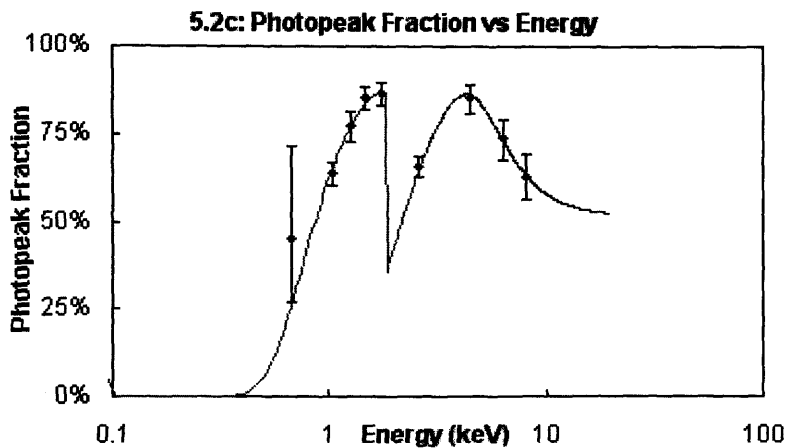
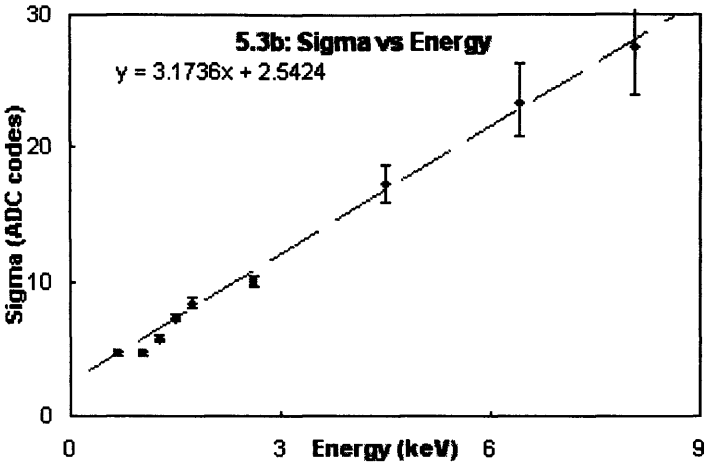
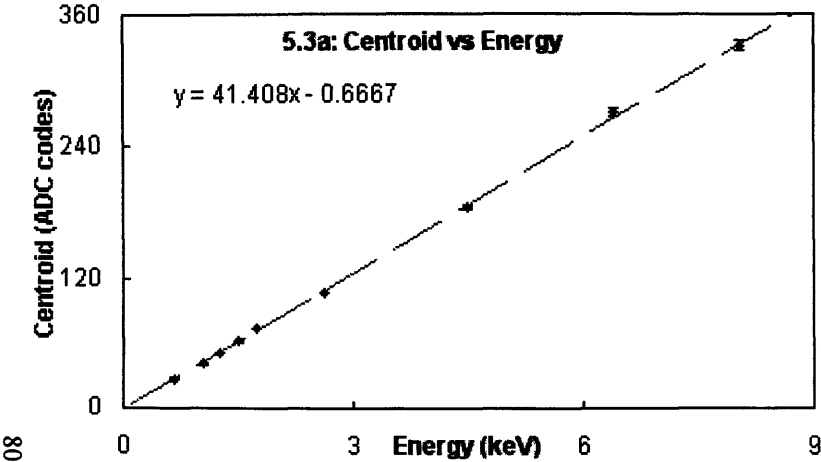


Figure 5.3: Calibration data from flight panel 1, channel 2



	Best	*	-
t1 (um)	0.98	0.34	0.30
t2 (um)	38.57	29.79	10.43
t3 (um)	69.31	189.62	33.59
RCHISQ	0.38		

	Best	*	-
tAL dead (um)	0.20		
tSi dead(um)	1.42	0.65	0.54
tSi (sense) (um)	20.84	13.01	8.46
RCHISQ	0.53		

Gain	104
Bias	1514
S/w Thresh	14
Serial No.	69R

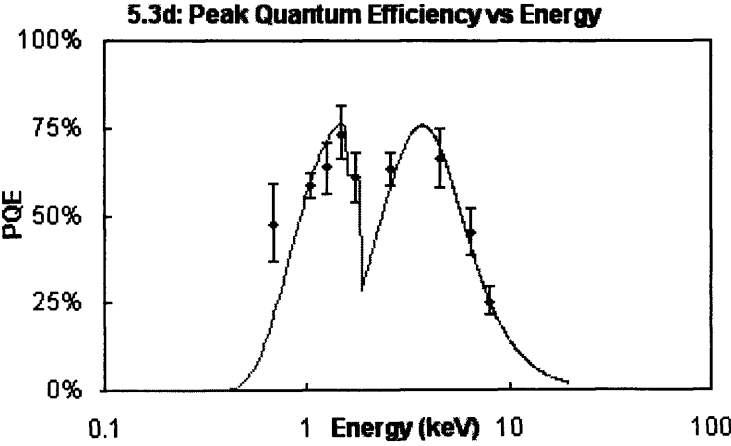
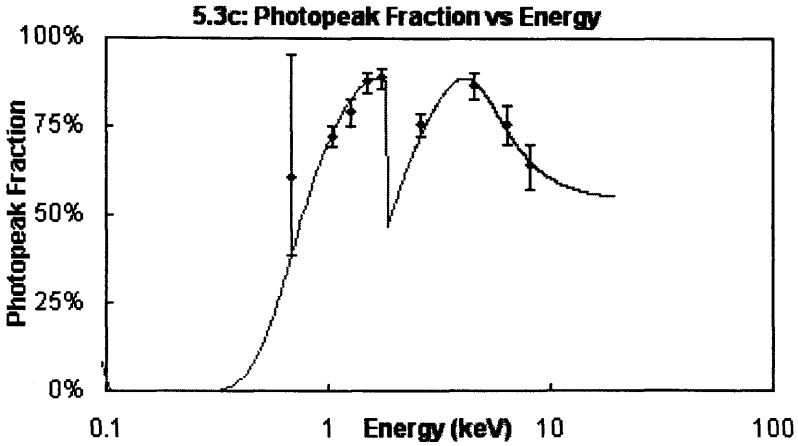
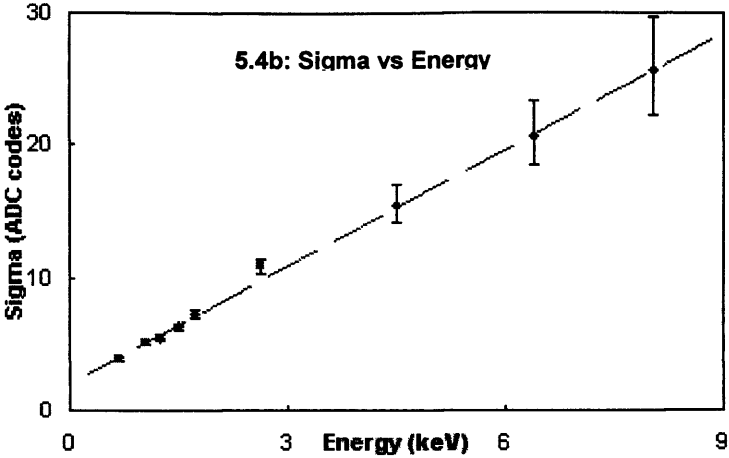
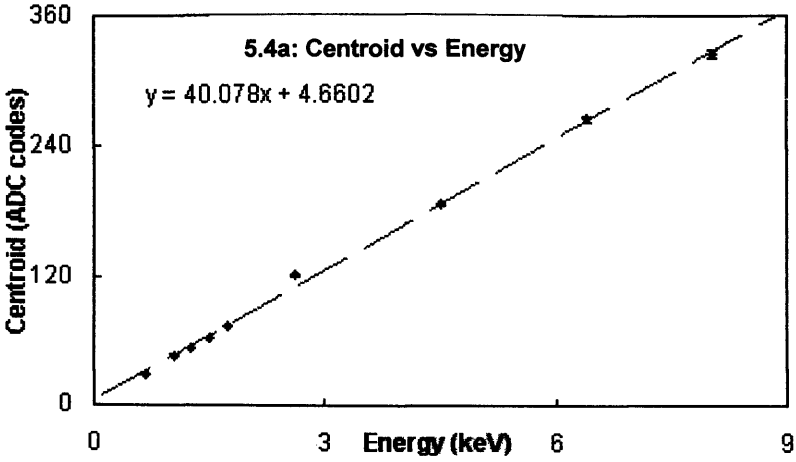


Figure 5.4: Calibration data from flight panel 1, channel 3



	Best	+	-
t1 (um)	1.07	0.37	0.33
t2 (um)	30.97	20.87	7.54
t3 (um)	53.27	57.24	24.29
RCHISQ	0.49		

	Best	+	-
tAL dead (um)	0.20		
tSi dead(um)	1.40	0.70	0.60
tSi (sense) (um)	20.20	12.75	8.40
RCHISQ	0.35		

Gain	100
Bias	1522
S/W Thresh	14
Serial No.	57

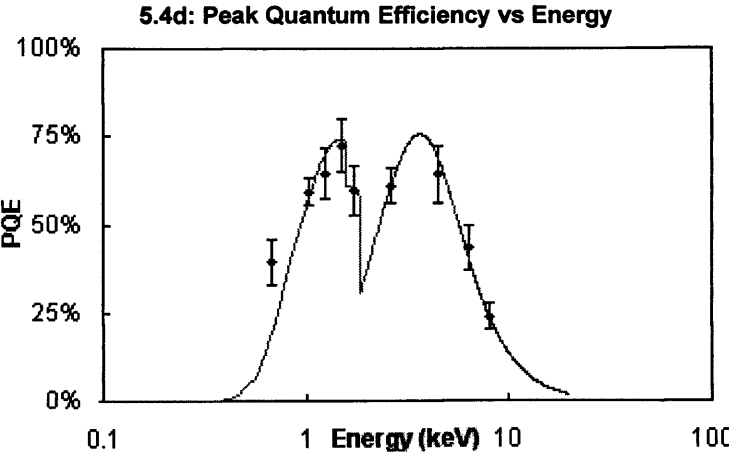
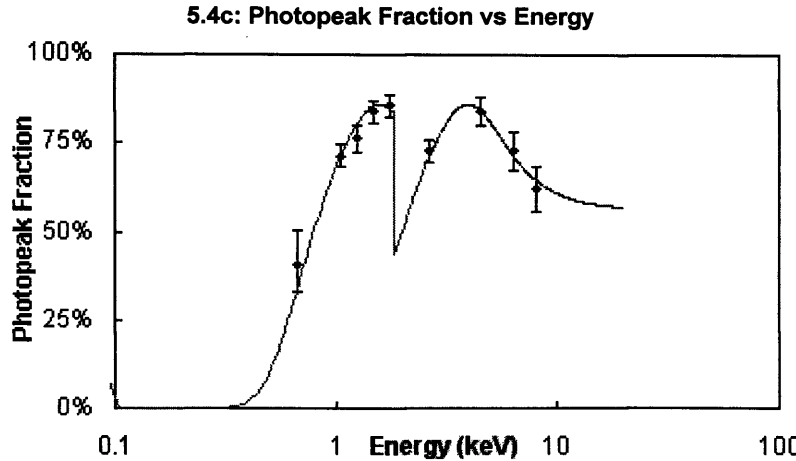
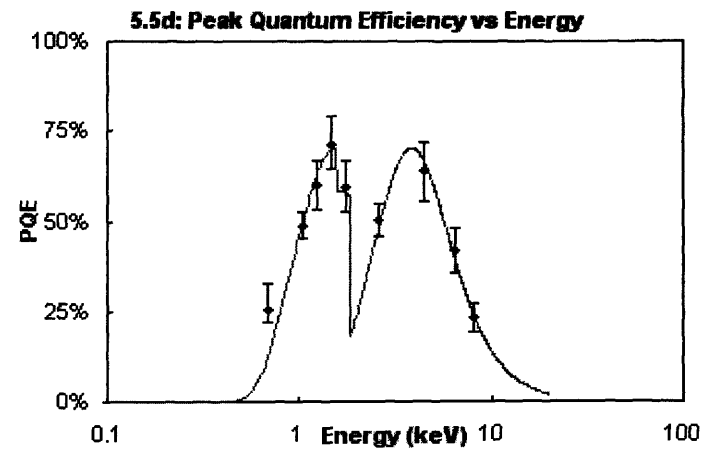
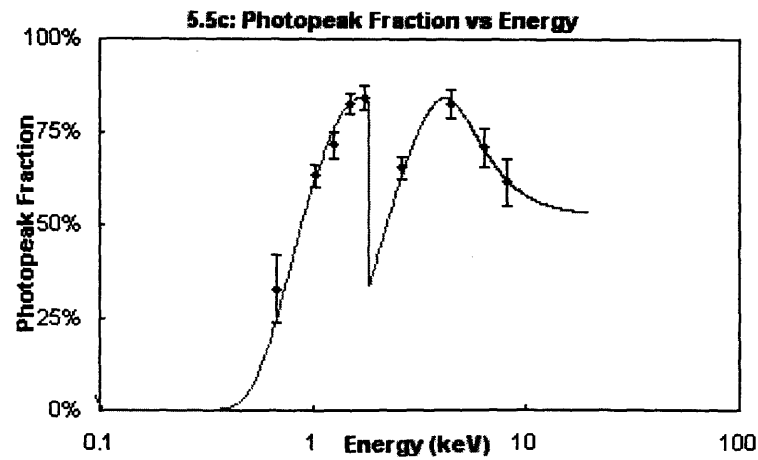
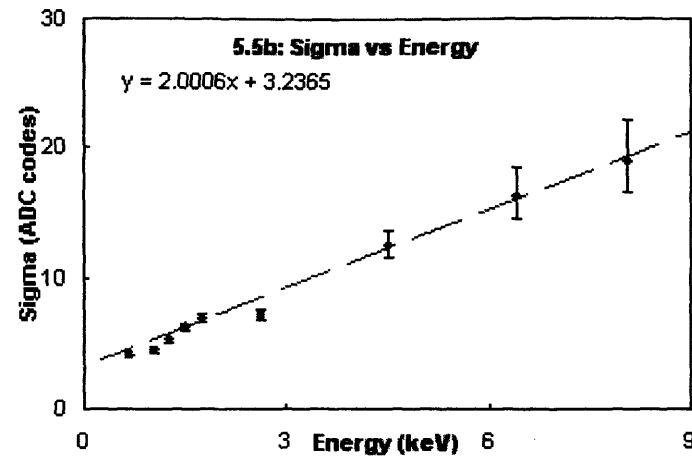
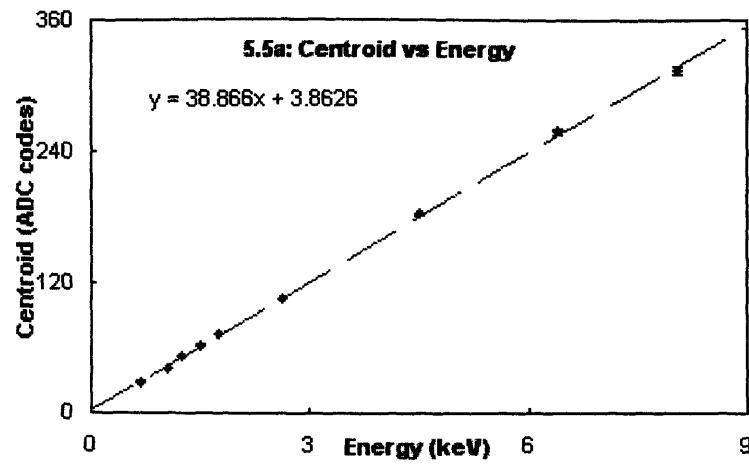




Figure 5.5: Calibration data from flight panel 1, channel 4



	Best	*	-
t1 (um)	1.42	0.41	0.36
t2 (um)	34.89	52.97	23.64
t3 (um)	63.88	4.83E+17	47.43
RCHISQ	0.42		

	Best	*	-
tAl dead (um)	0.19		
tSi dead (um)	2.01	0.79	0.66
tSi (sense) (um)	20.17	12.10	7.77
RCHISQ	0.13		

Gain	97
Bias	1503
SW Thresh	14
Serial No.	1

Figure 5.6: Calibration data from flight panel 1, channel 5

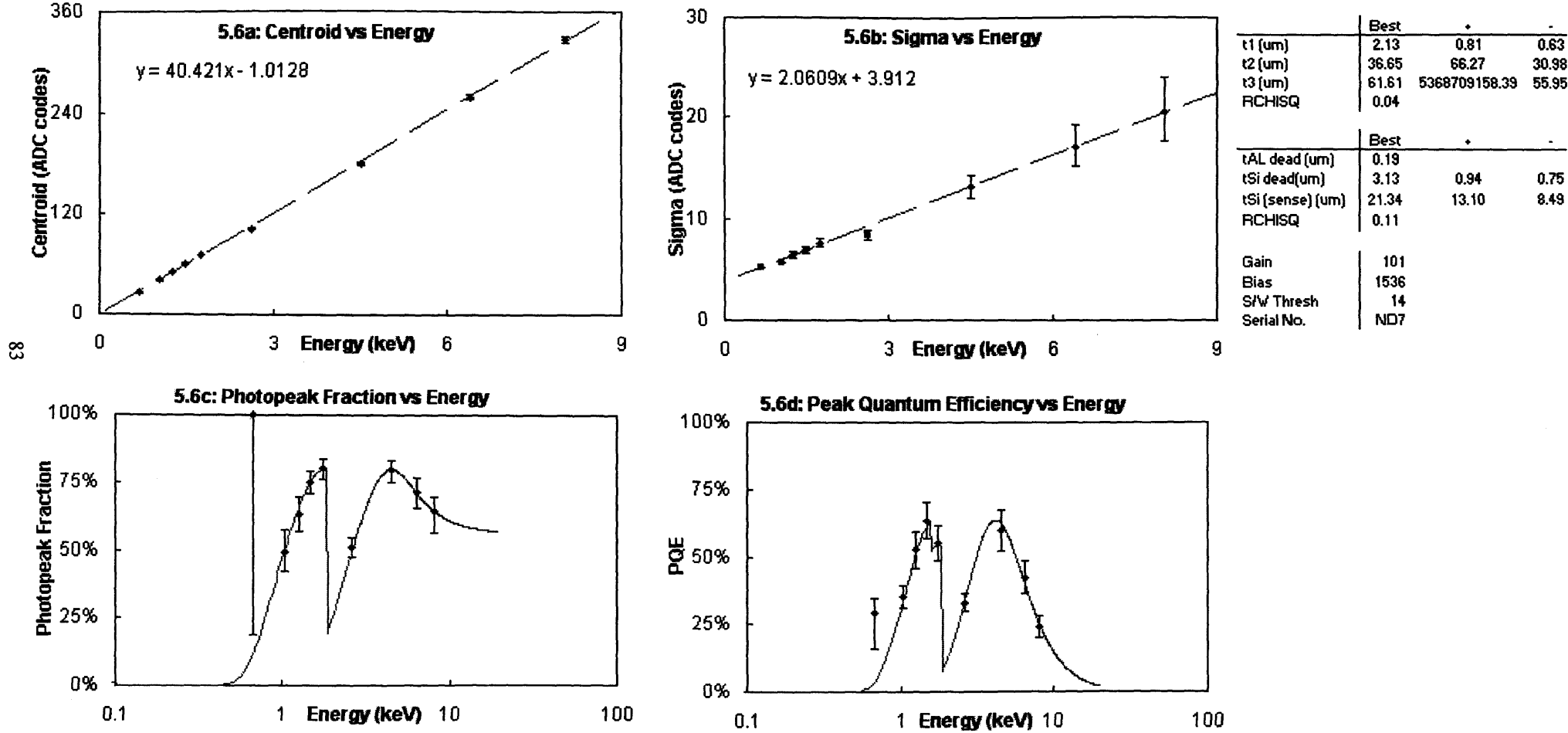
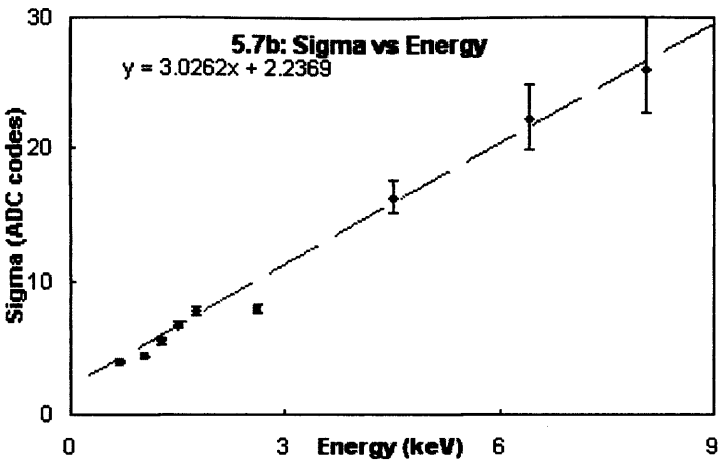
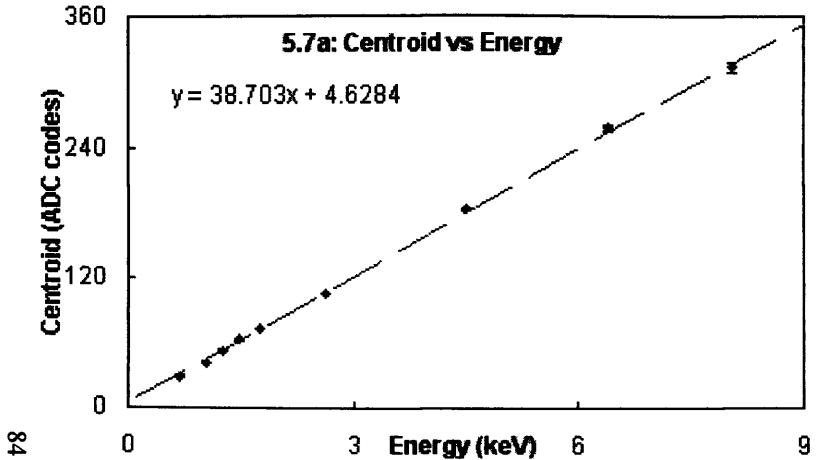


Figure 5.7: Calibration data from flight panel 1, channel 7



	Best	*	-
t1 (um)	1.23	0.37	0.33
t2 (um)	36.54	22.20	9.98
t3 (um)	68.35	7339296673.31	48.34
RCHISQ	0.32		

	Best	*	-
tAL dead (um)	0.19		
tSi dead(um)	1.77	0.64	0.55
tSi (sense) (um)	20.74	11.83	7.99
RCHISQ	0.19		

Gain	97
Bias	1509
S/w Thresh	14
Serial No.	34

Chapter 5: Calibration results

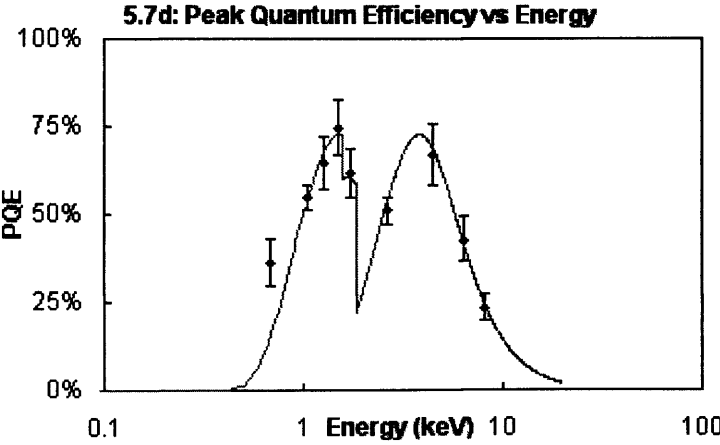
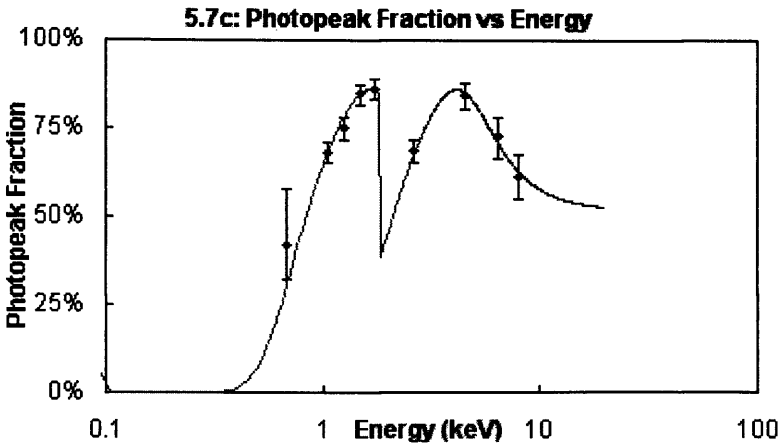
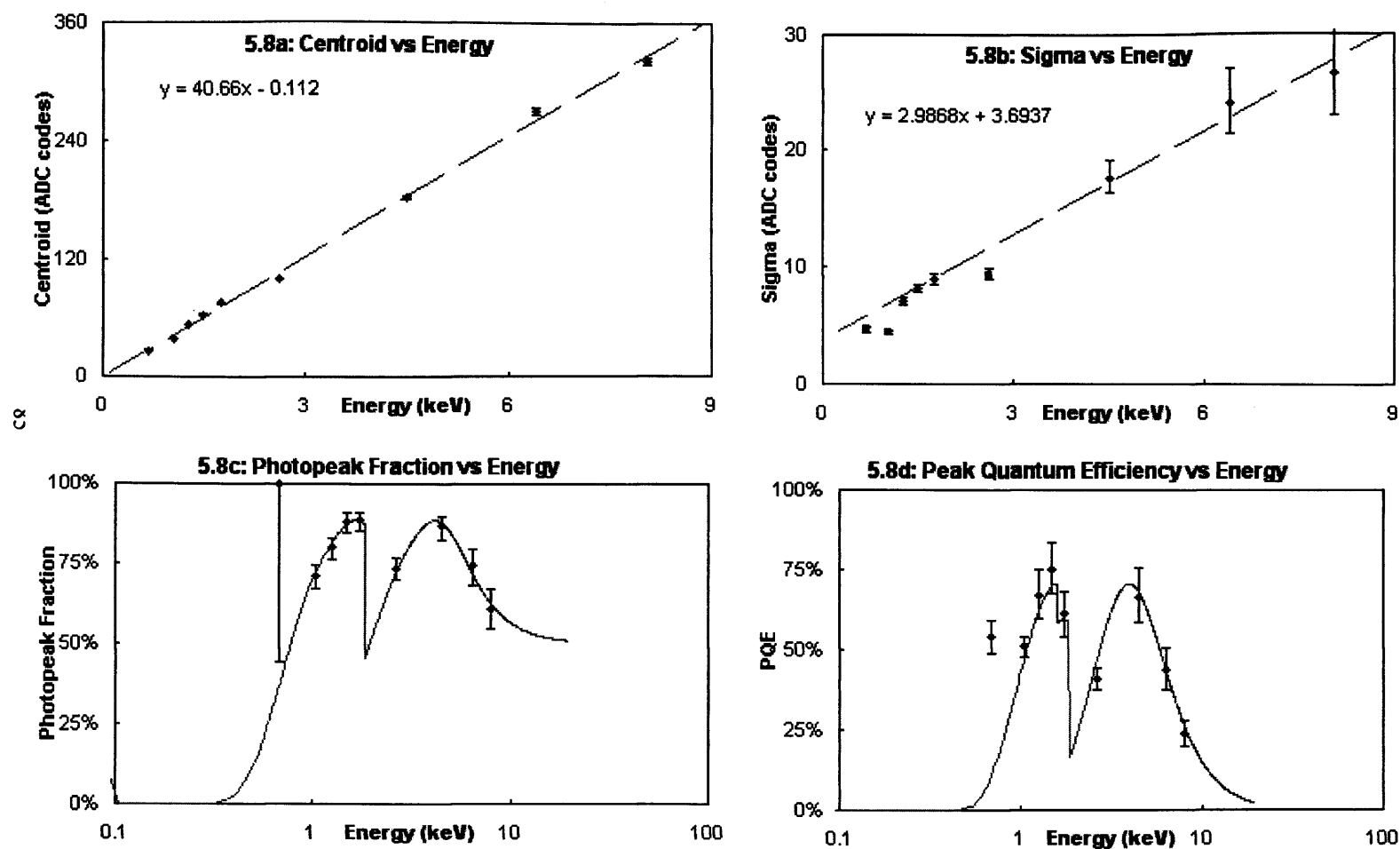
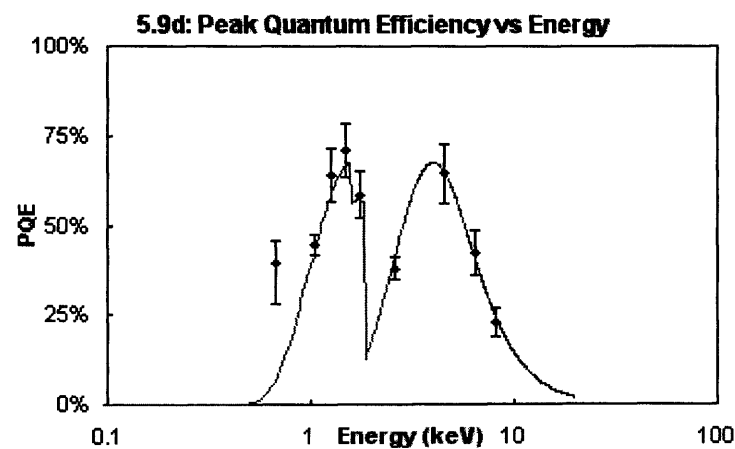
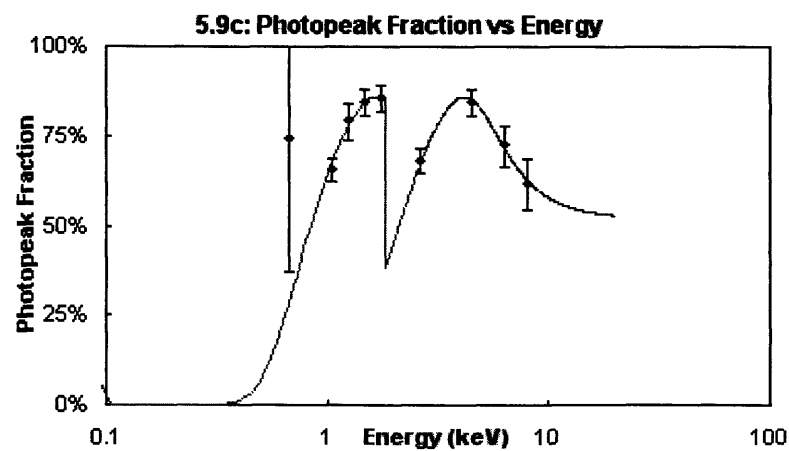
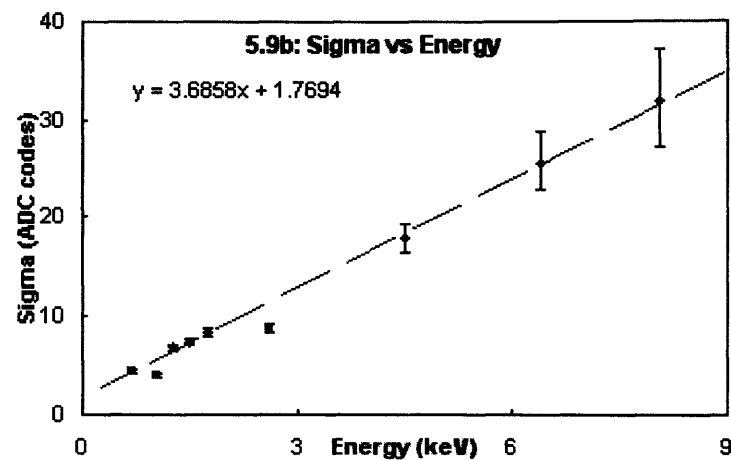
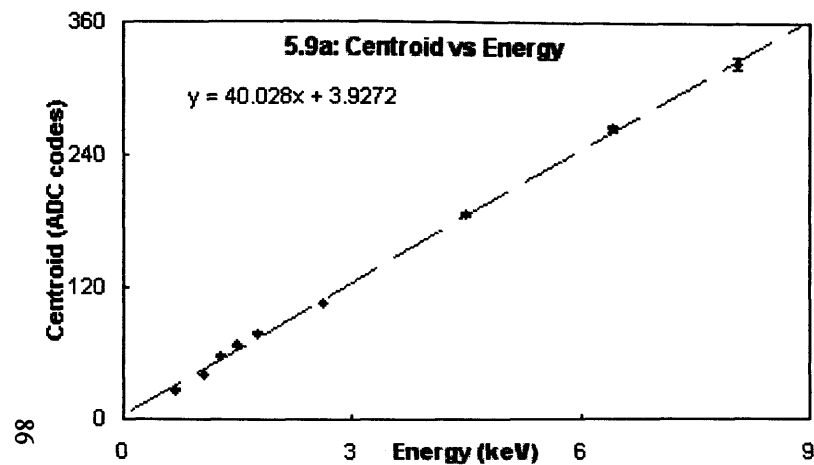


Figure 5.8: Calibration data from flight panel 1, channel 8



	Best	+	-
t1 (um)	1.02	0.39	0.34
t2 (um)	39.50	25.47	11.44
t3 (um)	77.22	8291849736.66	55.36
RCHISQ	0.17		
	Best	+	-
tAL dead (um)	0.19		
tSi dead(um)	2.15	0.67	0.58
tSi (sense) (um)	22.01	12.50	8.45
RCHISQ	1.21		
Gain	102		
Bias	1509		
S/W Thresh	14		
Serial No.	96		

Figure 5.9: Calibration data from flight panel 1, channel 9



	Best	+	-
t1 (um)	1.24	0.44	0.38
t2 (um)	36.52	27.69	10.79
t3 (um)	67.82	7282033191.01	32.62
RCHISQ	0.09		

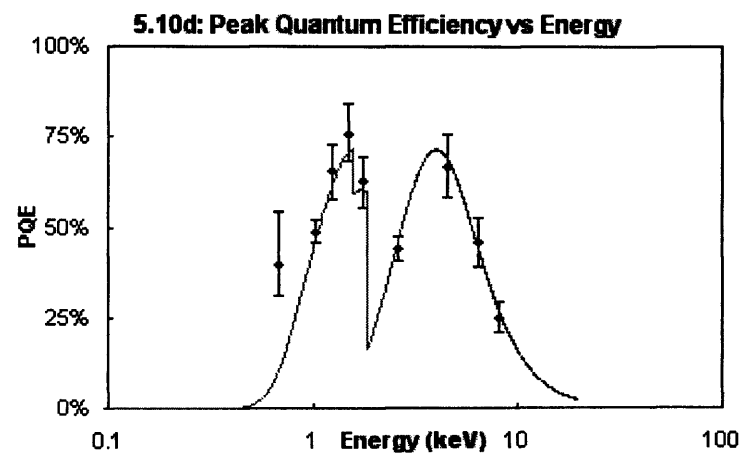
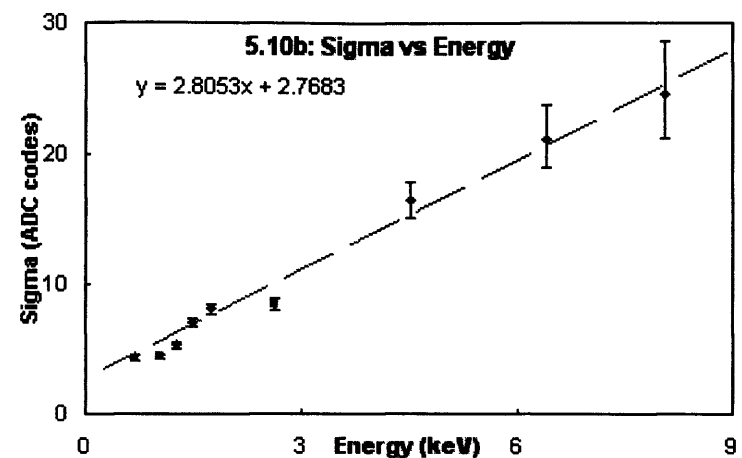
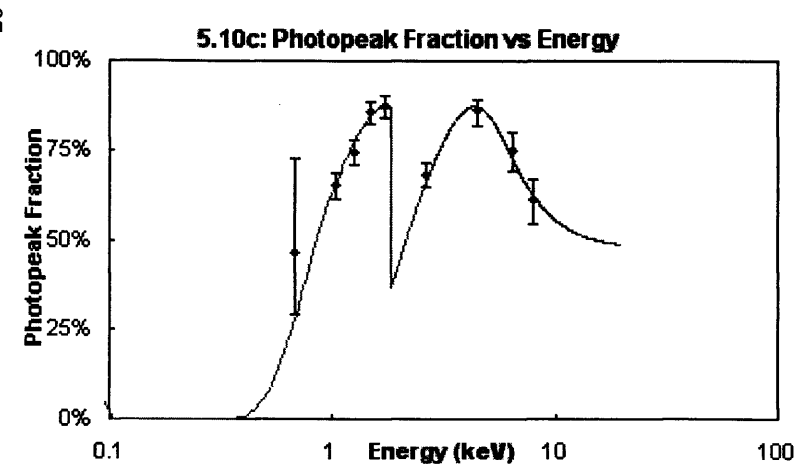
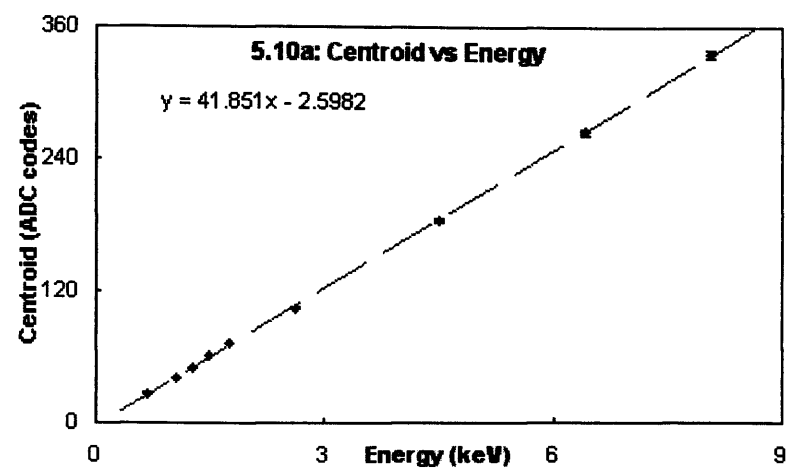
  

	Best	+	-
tAL dead (um)	0.19		
tSi dead(um)	2.47	0.69	0.59
tSi (sense) (um)	21.08	11.93	8.05
RCHISQ	0.77		

Gain	100
Bias	1530
S/W Thresh	14
Serial No.	112R

Figure 5.10: Calibration data from flight panel 1, channel 11



	Best	*	-
t1 (um)	1.30	0.41	0.36
t2 (um)	44.22	30.78	13.32
t3 (um)	90.11	9675018082.77	44.50
POCHSQ	0.33		

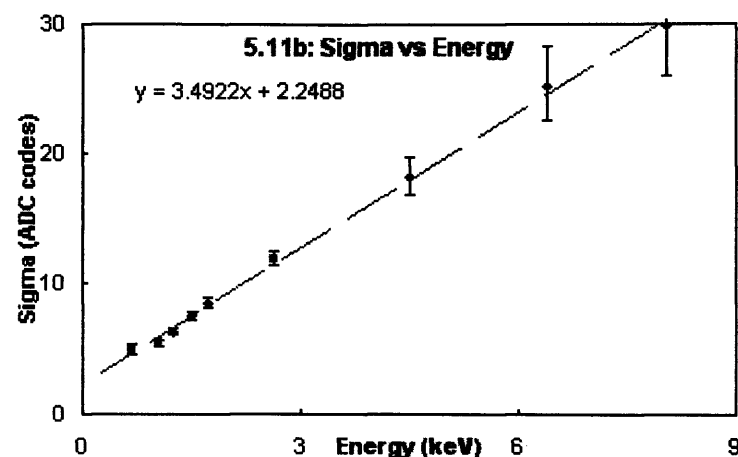
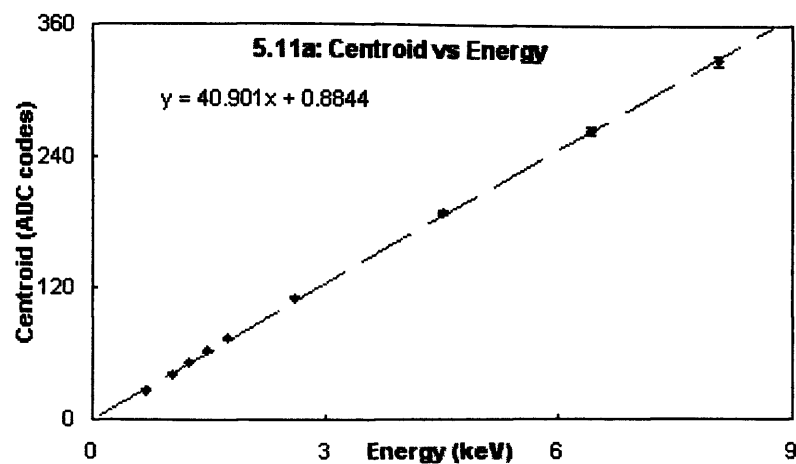
  

	Best	*	-
tAL dead (um)	0.19		
tSi dead(um)	2.13	0.66	0.56
tSi (sense) (um)	23.04	13.54	8.99
POCHSQ	0.44		

Gain	105		
Bias	1496		
S/W Thresh	14		
Serial No.	103		

Figure 5.11: Calibration data from flight panel 1, channel 12



	Best	+	-
t1 (um)	1.05	0.44	0.39
t2 (um)	36.47	26.39	10.10
t3 (um)	64.67	143.38	29.50
RCHISQ	0.15		

	Best	+	-
tAL dead (um)	0.20		
tSi dead(um)	1.68	0.67	0.56
tSi (sense) (um)	20.98	12.75	8.41
RCHISQ	0.21		

Gain	102
Bias	1531
S/w Thresh	14
Serial No.	117

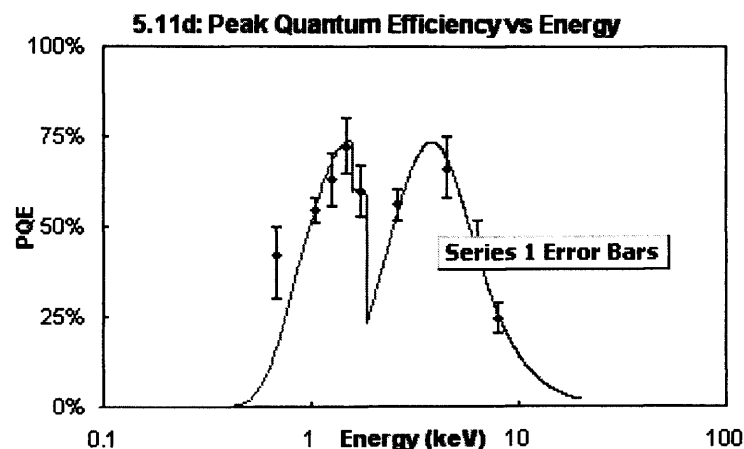
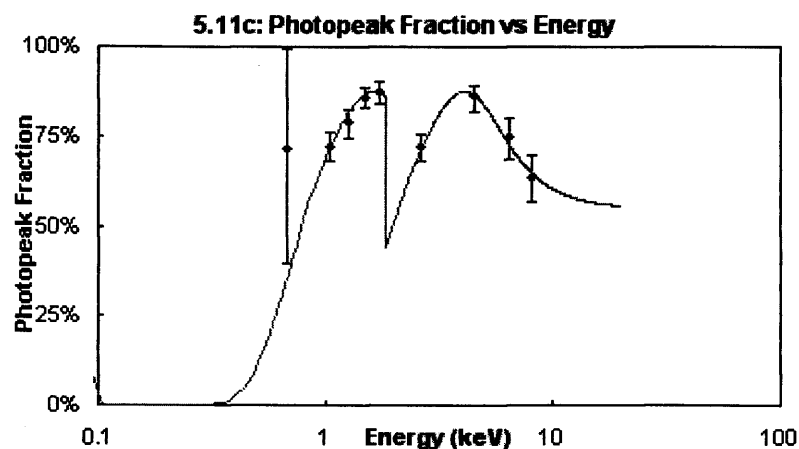
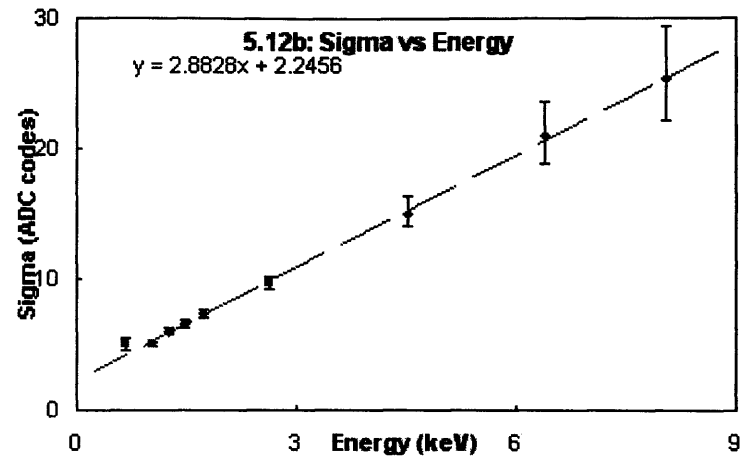
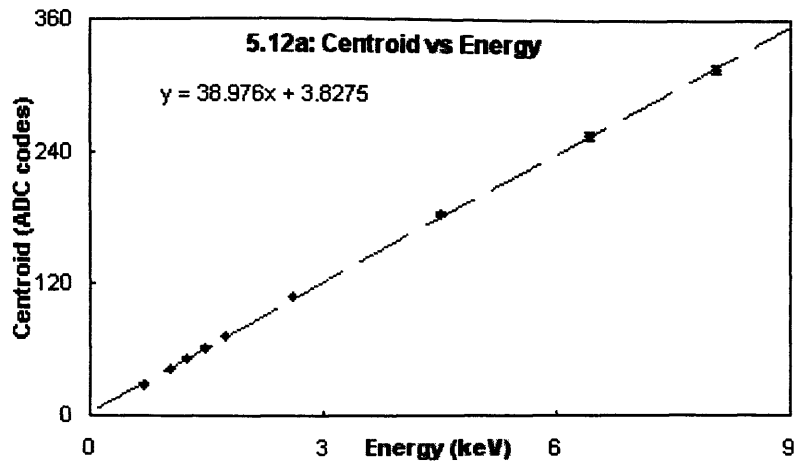


Figure 5.12: Calibration data from flight panel 1, channel 13



	Best	+	-
t1 (um)	1.37	0.47	0.42
t2 (um)	33.25	52.07	9.05
t3 (um)	60.76	138.84	31.07
RCHISQ	0.22		

	Best	+	-
tAL dead (um)	0.19		
tSi dead(um)	1.96	0.70	0.60
tSi (sense) (um)	19.81	11.47	7.67
RCHISQ	0.11		

Gain	97
Bias	1519
S/W Thresh	14
Serial No.	116

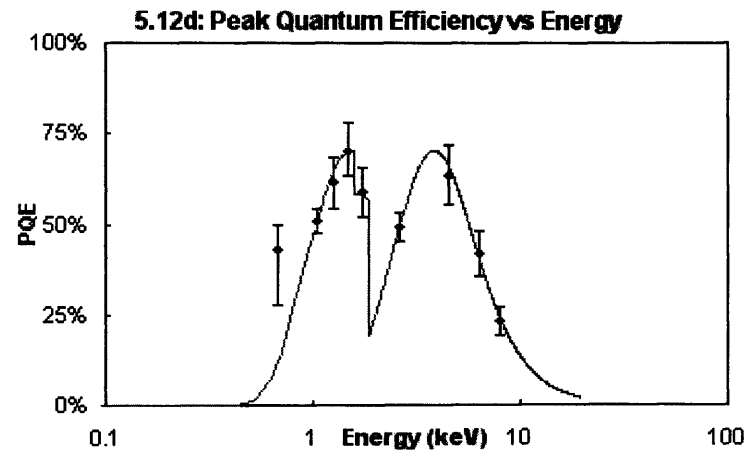
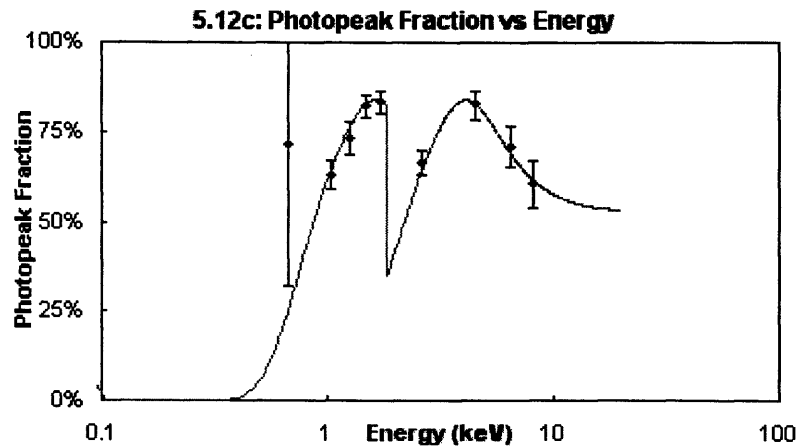
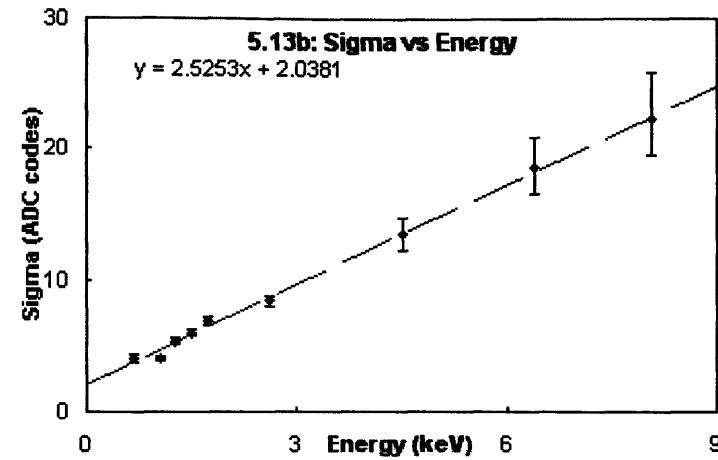
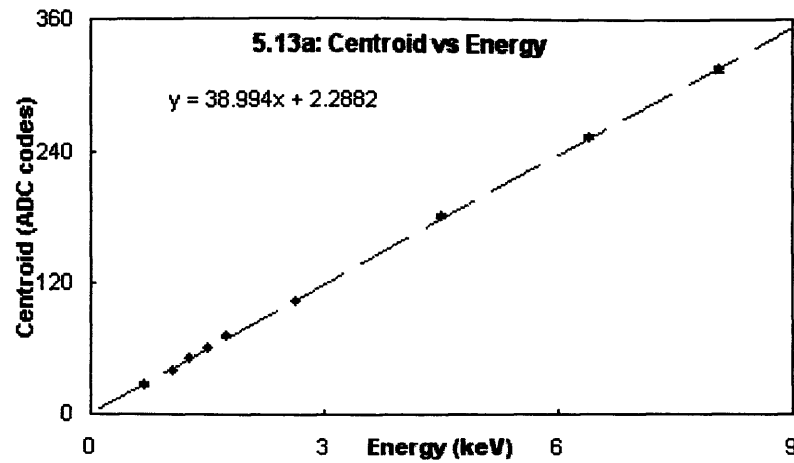




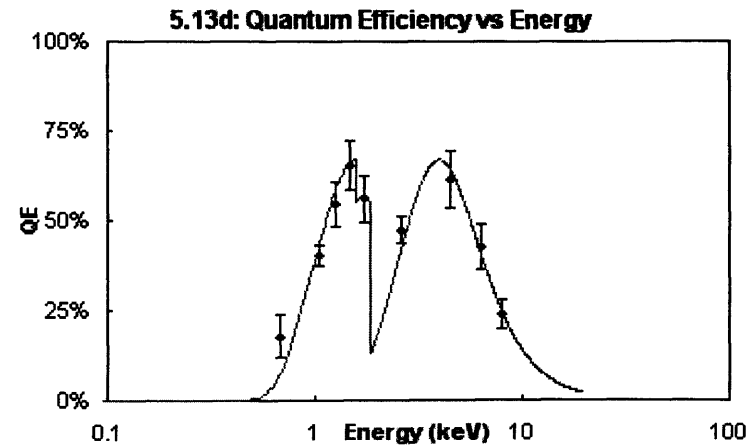
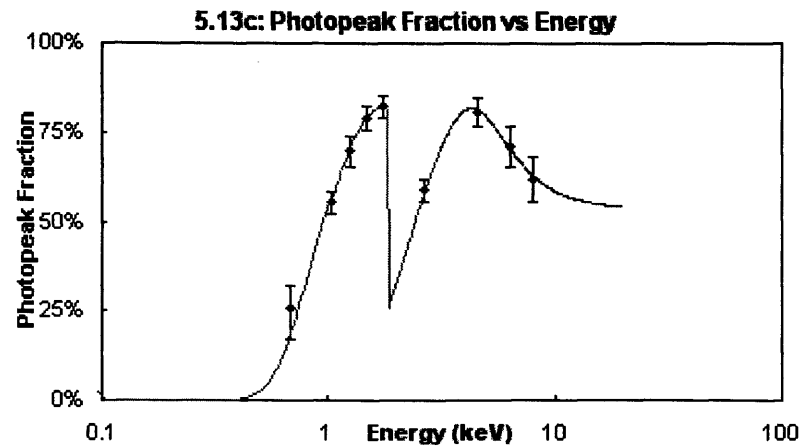
Figure 5.13: Calibration data from flight panel 1, channel 14



	Best	+	-
t1 (um)	1.74	0.48	0.42
t2 (um)	35.38	57.60	9.72
t3 (um)	62.94	135.81	32.29
RCHISQ	0.15		

	Best	+	-
tAL dead (um)	0.19		
tSi dead(um)	2.46	0.72	0.61
tSi (sense) (um)	20.29	12.06	7.97
RCHISQ	0.60		

Gain	97
Bias	1531
S/W Thresh	14
Serial No.	11



There are no data from channels 6 or 10 as these were empty as a result of the APD grouping scheme presented in chapter 4. Furthermore there are no data from channel 15 as the diode in that channel had ceased to function in-between screening and calibration.

All the diodes in flight panel one have a centroid vs. energy relationship that is linear, as expected. The gradient of this line can be used to calculate the gain: The amplifier electronics are set up to produce an energy/ADC channel relation of 25 eV per channel when the APD is operating at its nominal gain of 100. Therefore, the gain of an APD is given by:

$$\begin{aligned} G &= \text{gradient (ADC channels/keV)} \times 0.025 \text{ keV} \times 100 \\ G &= \text{gradient} \times 2.5 \end{aligned} \quad \text{Eq 6.1}$$

This is the gain given in the upper right hand corner in each of figures 5.1 to 5.13. All of the APDs in flight panel one were calibrated whilst operating within 5% of a gain of 100.

The intercept of the centroid vs. energy line with the y axis is not always zero, probably indicating a small offset in the analogue to digital converters (ADCs). These offsets never exceeded 5 ADC channels or 125 eV.

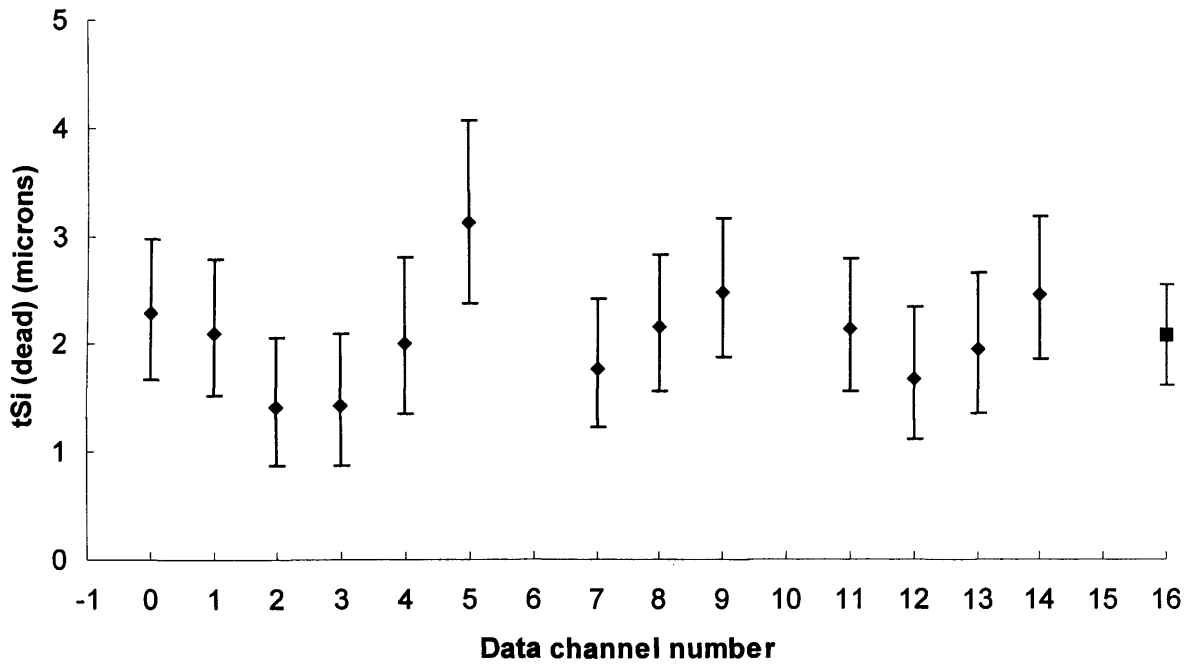
The width of the X-ray peak,  $\sigma$ , also increases linearly with energy. In general, X-ray detectors have a  $\sigma$  vs. energy relation that is a square root function of energy, indicative of Poission statistics (Fraser 1989). The unusual success of a straight line in describing peak width is not surprising when one recalls that in an APD peak width is dominated by gain non-uniformity, rather than by the usual statistical processes.

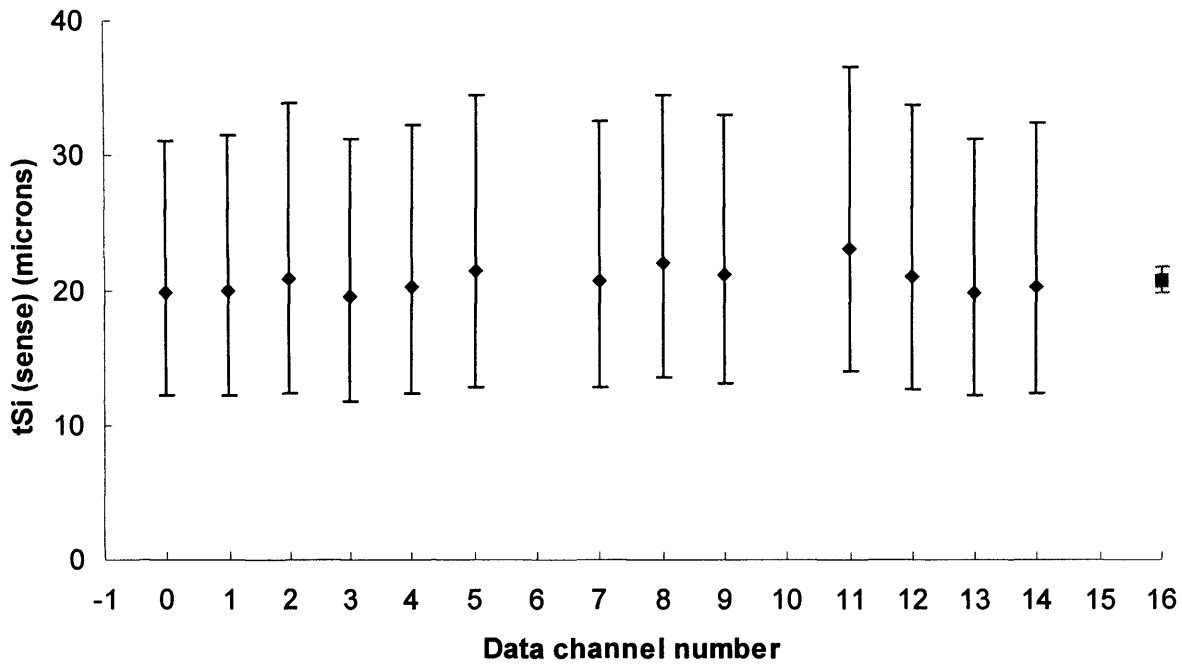
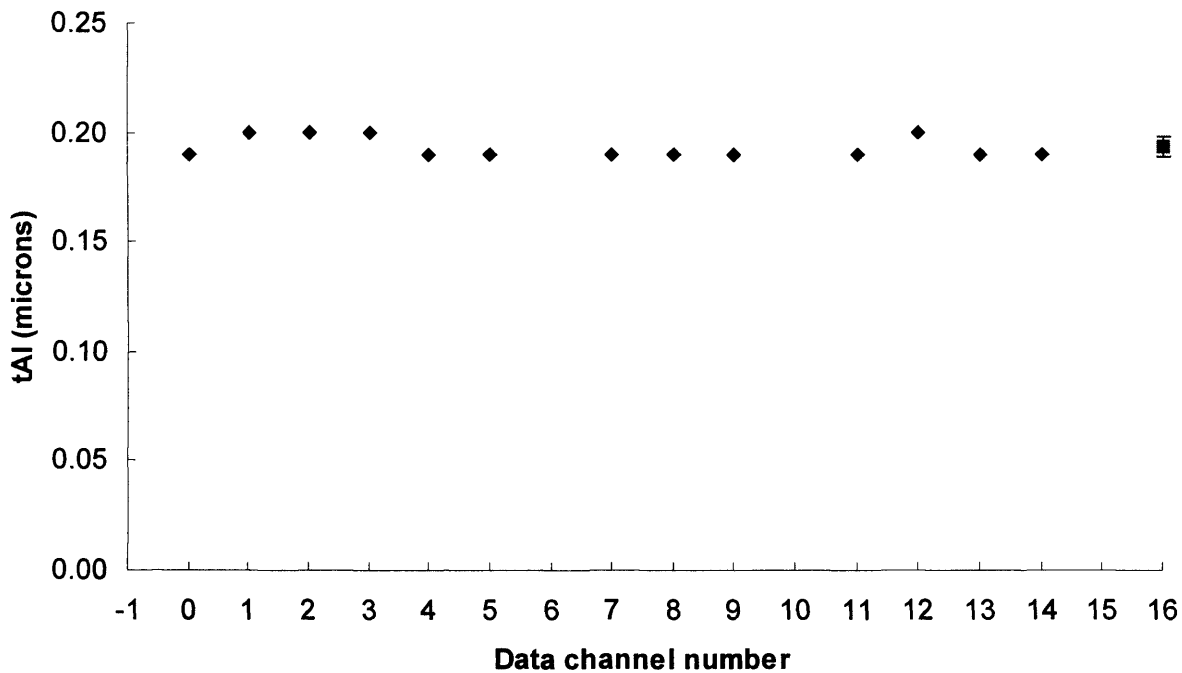
As predicted, detected widths of lines produced using the soft X-ray source are generally less than those of lines produced using the kevex source. This is especially apparent in figures 5.2 and 5.8. Two unexpected exceptions to this rule occur in figures 5.4 and 5.12, where one of the soft X-ray source lines is actually broader than suggested by the linear relationship. These anomalies remain unexplained.

The Peak Quantum Efficiency (PQE) model for APDs is a good description of the data in figures 5.1 to 5.13, the highest value of reduced chi squared being 1.21 (figure 5.8). As with the data presented in chapter 3, the lowest energy data point does not fit in with the others and has been excluded from the fitting process. Table 1 summarises all of the best fit PQE model parameters and their errors. The table also shows the average model parameters and their standard deviations. The same data is shown graphically in figures 5.14, 5.15 & 5.16. Channel 16 has been used to show the average and it's standard deviation.

**Table 1: Best fit PQE model parameters**

APD Channel	TAI ( $\mu\text{m}$ ) Best	TSi (dead) ( $\mu\text{m}$ )			TSi (sense) ( $\mu\text{m}$ )			Rchi <sup>2</sup>
		Best	+	-	Best	+	-	
0	0.19	2.3	0.7	0.6	20	11	8	0.12
1	0.20	2.1	0.7	0.6	20	12	8	0.16
2	0.20	1.4	0.7	0.5	21	13	8	0.53
3	0.20	1.4	0.7	0.6	20	12	8	0.35
4	0.19	2.0	0.8	0.7	20	12	8	0.13
5	0.20	3.1	0.9	0.8	21	13	8	0.11
7	0.19	1.8	0.6	0.6	21	12	8	0.19
8	0.19	2.2	0.7	0.6	22	13	8	1.21
9	0.19	2.5	0.7	0.6	21	12	8	0.77
11	0.19	2.1	0.7	0.6	23	14	9	0.44
12	0.20	1.7	0.7	0.6	21	13	8	0.21
13	0.19	2.0	0.7	0.6	20	11	8	0.11
14	0.19	2.5	0.7	0.6	20	12	8	0.60
<b>Average</b>	<b>0.193<math>\pm</math>0.005</b>	<b>2.1<math>\pm</math>0.5</b>			<b>21<math>\pm</math>1</b>			

**Figure 5.14: Best fit values of tSi(dead) for APDs in flight panel 1**

**Figure 5.15: Best fit values of  $t_{Si}(\text{sense})$  for APDs in flight panel 1****Figure 5.16: Best fit values of  $t_{Al}$  for APDs in flight panel 1**

It has been possible to determine positive and negative error ranges of  $t_{SiO2}(\text{dead})$  and  $t_{SiO2}(\text{sense})$  for all the APDs, though no error estimates are given for  $t_{Al}$  as this was constrained to lie between  $0.19\mu\text{m}$  and  $0.21\mu\text{m}$  as described in chapter 3. For both  $t_{SiO2}(\text{dead})$  and  $t_{SiO2}(\text{sense})$ , the average value is consistent with all but one of the measured values. This reflects the fact that

the spread of the data is much less than the error on any one data point, which suggests that production methods at RMD yield APDs with internal structures that are consistent beyond our ability to test them.

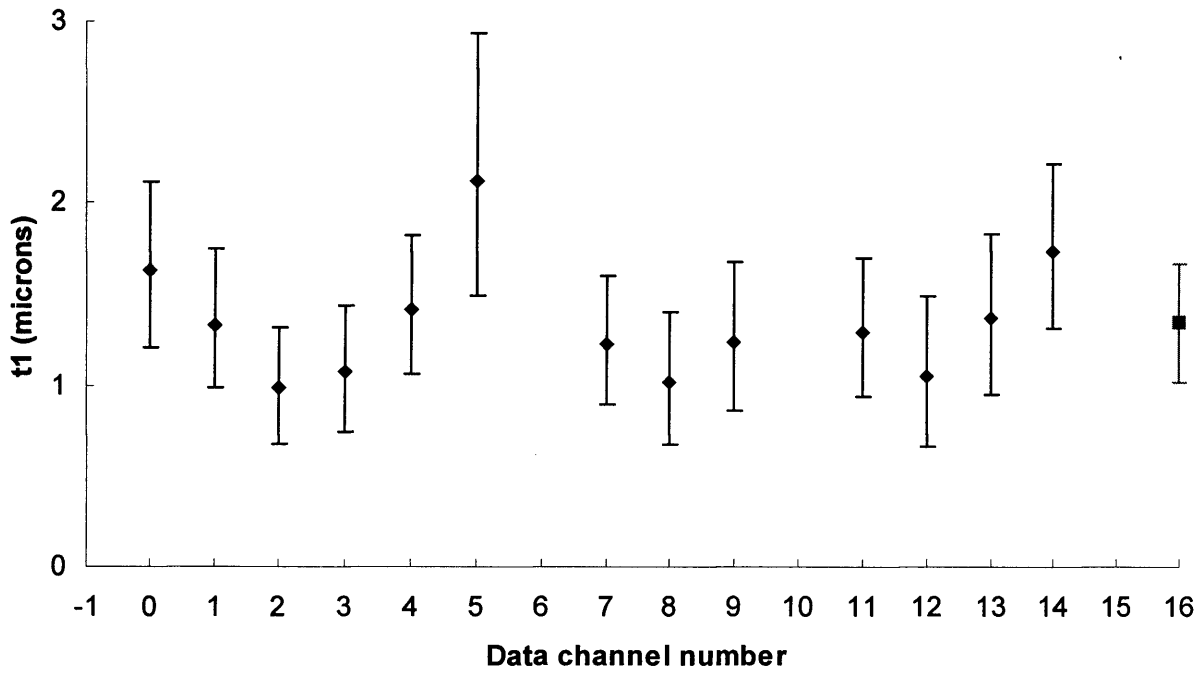
The measured thicknesses of the silicon dead layer are all of the order of a micron, as we expected (Farrell 1999). The thicknesses of the sensing layer ( $t_{Si(sense)}$ ) are also consistent with expectation, namely that they be less than 40 microns (Farrell 1999).

The PF model describes all of the PF data well; the highest value of reduced chi squared being 0.49 (figure 5.4). As with the PQE data, the lowest energy data point has been excluded from the fitting process. Table 2 summarises all of the best fit PF model parameters and their errors for the 13 APDs that were tested. The table also shows the average model parameters and their standard deviations. The same data is shown graphically in figures 5.17, 5.18 and 6.19. Again, channel 16 has been used to show the average and it's standard deviation.

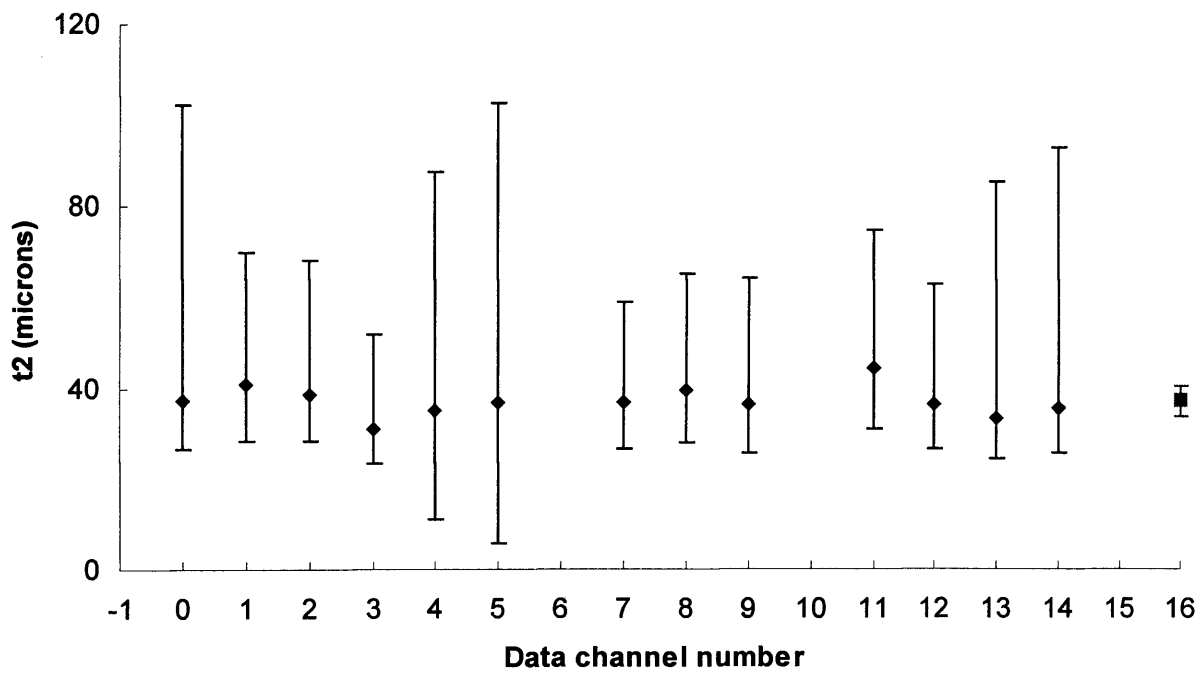
**Table 2: Best fit PF model parameters**

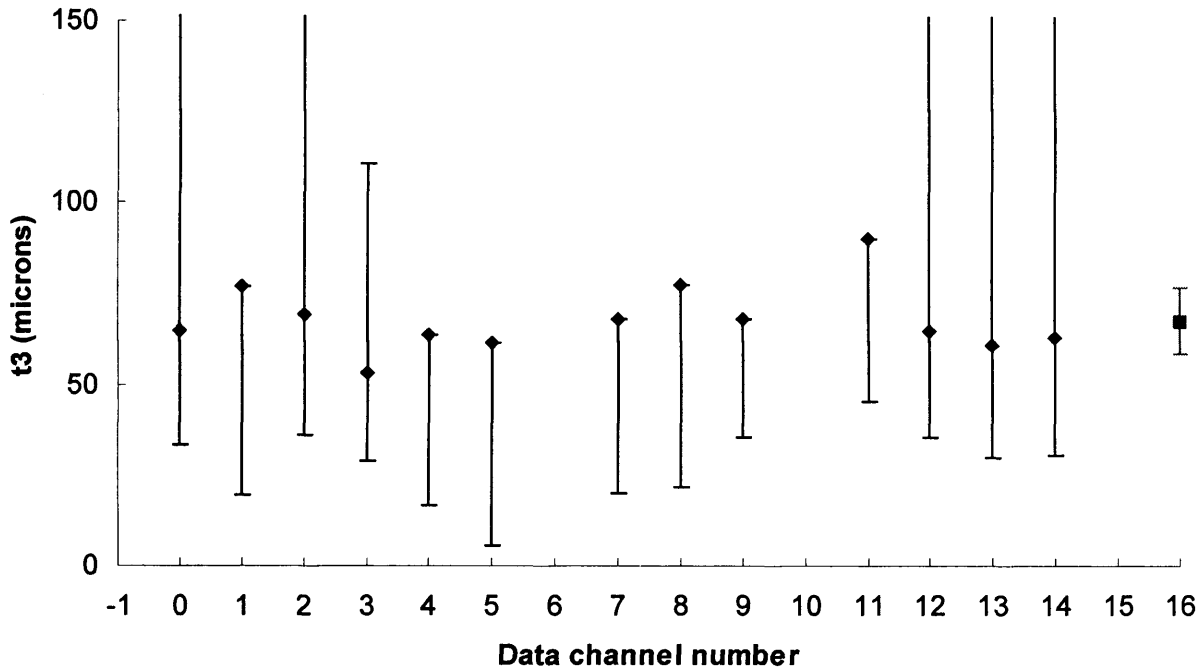
APD	T1( $\mu\text{m}$ )			T2( $\mu\text{m}$ )			T3( $\mu\text{m}$ )			Rchi <sup>2</sup>
Channel	Best	+	-	Best	+	-	Best	+	-	
0	1.6	0.5	0.4	40	70	10	60	210	30	0.21
1	1.3	0.4	0.4	40	30	10	80		60	0.11
2	1.0	0.3	0.3	40	30	10	70	190	30	0.38
3	1.1	0.4	0.3	30	20	7	50	60	20	0.49
4	1.4	0.4	0.4	30	50	20	60		50	0.42
5	2.1	0.8	0.6	40	70	30	60		60	0.04
7	1.2	0.4	0.3	40	20	10	70		50	0.32
8	1.0	0.4	0.3	40	30	10	80		50	0.17
9	1.2	0.4	0.4	40	30	10	70		30	0.09
11	1.3	0.4	0.4	40	30	10	90		40	0.33
12	1.1	0.4	0.4	40	30	10	60	140	30	0.15
13	1.4	0.5	0.4	30	50	10	60	140	30	0.22
14	1.7	0.5	0.4	40	60	10	60	140	30	0.15
Average		1.3 $\pm$ 0.3			37 $\pm$ 3			68 $\pm$ 9		

**Figure 5.17: Best fit values of  $t_1$  for APDs in flight panel 1**



**Figure 5.18: Best fit values of  $t_2$  for APDs in flight panel 1**



**Figure 5.19: Best fit values of  $t_3$  for APDs in flight panel 1**

In the case of PF model parameter  $t_3$ , it was not always possible to determine the positive error because the chi squared landscape was too flat (ie: chi squared is too insensitive to changes in  $t_3$ ).

For both  $t_2$  and  $t_3$ , the average value is consistent with all of the measured values and for parameter  $t_1$  the average value is consistent with the measured value for all devices except those in channels 2 and 5. This consistency is reliant in the large error ranges of the fitted parameters, which is a result of the insensitivity problem discussed in chapter 3. We can say, then, that the results show that these diodes are consistent in their properties to the extent that we may test.

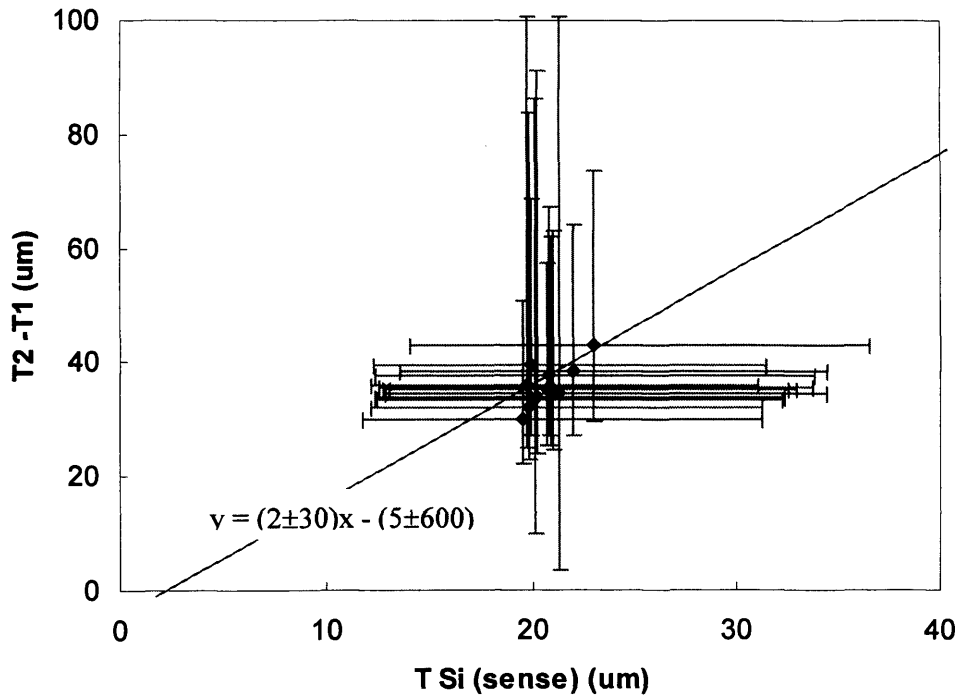
As discussed in chapter 3, we expect that  $t_1 < t_{Si(dead)}$  and this is indeed the case for all 13 APDs tested here. Furthermore, we expect that  $t_2 < 40\mu m$  and all of these data are consistent with this expectation. We also expect that  $t_2 - t_1 = t_{Si(sense)}$ . Figure 5.20 shows a plot of  $t_2 - t_1$  against  $t_{Si(sense)}$ . The error bars on these parameters are very great; a fact that arises as a result of the insensitivity problem described in sections 3.5 and 3.6. This problem could be addressed by recording APD spectra at many more energies. The large error bars make interpretation difficult. Even so, it is apparent that a straight line passing through the origin and having a gradient of one is not consistent with the majority of the data points. This contradiction of our

expectation probably reveals over-simplification in the PQE and PF models. A straight line has been fitted to the data and its equation is shown on the chart.

Finally, we expect that  $t_3 < 90$  microns and all the data is consistent with this expectation.

The value of all these results lies in the fact that the best fit model parameters can now be used in conjunction with the models of chapter 3 to predict the response of an APD to an arbitrary input X-ray spectrum.

**Fig 5.20: A test for correlation between TSi(sense) and (T2-T1)**





## Chapter 6

# SXR performance

Using the data in chapter five and the models in chapter three, it has been possible to produce a complete response matrix for SXR flight panel one, which has been used to investigate the likely performance of the SXR in an astrophysical context. This chapter introduces the response matrix and presents the analyses that have been performed.

### 6.1 Response matrices

When an X-ray spectrum,  $N(E)$  with  $N$  photons at energy  $E$ , is incident upon an X-ray detector, a pulse height spectrum,  $N(H)$ , is produced, with  $N$  counts of height  $H$ . In an ideal detector the two distributions are identical. In reality no detector is like this. The response of most detectors is such that even a perfectly monochromatic beam of X-rays will give rise to pulses of many heights due to noise, escape peaks or other artefacts of the detector. These effects can be accounted for by using a "response matrix" to predict the pulse height distribution produced by a particular X-ray spectrum. The photon spectrum is turned into a column vector  $\mathbf{E}$  of dimension  $n$ , where each element represents the number of incident photons between two distinct energies. The count spectrum is represented as another column vector  $\mathbf{C}$  of dimension  $m$ , where each element represents the number of pulses between two distinct heights.  $\mathbf{C}$  is given by the product  $\mathbf{R}\mathbf{E}$ , where  $\mathbf{R}$  has  $m$  rows and  $n$  columns and is the detector response matrix:

$$\mathbf{C} = \mathbf{R} \times \mathbf{E}$$

$$\begin{pmatrix} C_1 \\ C_2 \\ C_3 \\ C_4 \\ C_5 \\ \dots \\ C_m \end{pmatrix} = \begin{pmatrix} R_{11} & R_{12} & \dots & R_{1n} \\ R_{21} & & & \\ R_{31} & & & \\ R_{41} & & & \\ R_{51} & & & \\ \dots & & & \\ R_{m1} & & & R_{mn} \end{pmatrix} \times \begin{pmatrix} N(E_1) \\ N(E_2) \\ \dots \\ N(E_n) \end{pmatrix}$$

Eq. 7.1

Notice that the  $i^{\text{th}}$  column of  $\mathbf{R}$  represents the detector's response to photons of the energy of the  $i^{\text{th}}$  row of  $\mathbf{E}$ . Therefore, if we could record pulse height distributions resulting from all  $n$  energies, these distributions would make up the columns of  $\mathbf{R}$ . Obviously this is not practical. However, given the models presented in chapter three and the data presented in chapter five, we can predict the response of each APD in SXR flight panel number one to X-rays of any energy and in this way we have composed a response matrix for each device. A further response matrix has been composed whose parameters (eg:  $t_{\text{si(sense)}}$ ) were taken from the average of the devices in flight panel one. All of these matrices were produced as "fits" compatible response matrix files, using the Fortran library "fitsio".

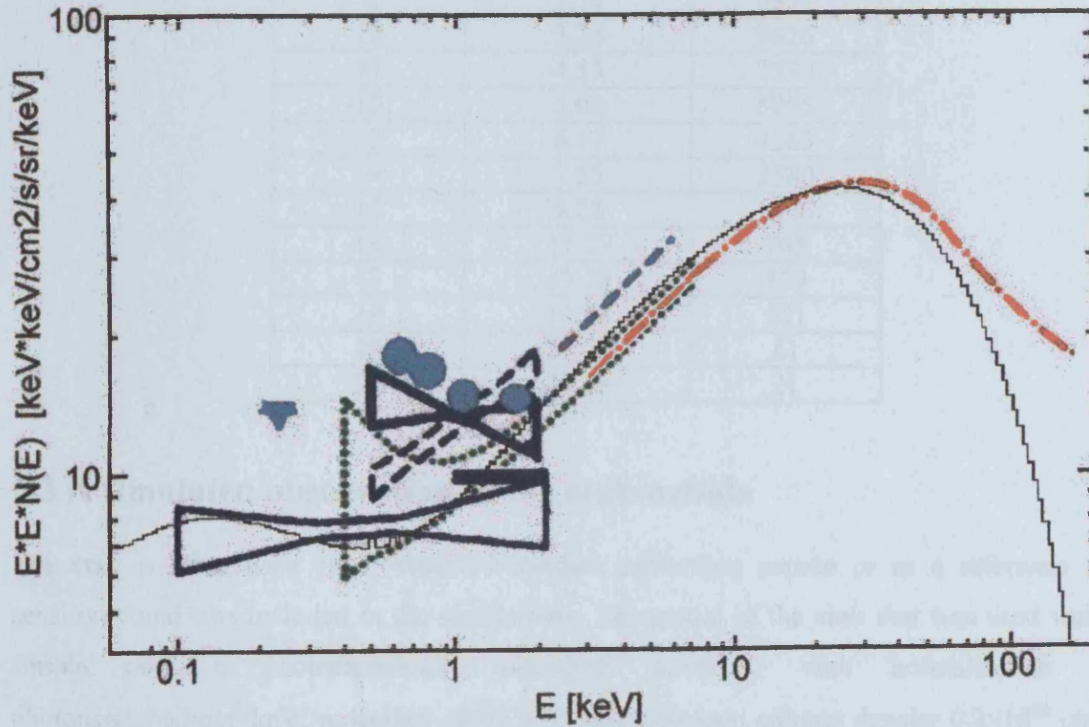
In order to represent the behaviour of a 'typical' SXR panel, a response matrix was produced consisting of the 13 functional APDs in flight panel one and three identical 'average' devices. This was achieved using the "addrmf" facility from the "ftools" software package, which adds fits compatible response matrix files. It is this composite response that has been used in the analyses throughout this chapter. All of the simulations and spectral fitting were performed using the analysis software "XSPEC".

## 6.2 Simulation of X-ray Background

The first simulation to be performed using the composite response matrix was a simulated observation of the cosmic X-ray background. The spectral model used to represent the X-ray background (XRB) was the same as that used in the analysis in chapter 4 (Hasinger 1996). Below 60 keV this model consists of only three components: a plasma ( $kT \approx 0.215$  keV), another plasma ( $kT \approx 0.086$  keV) and a Bremsstrahlung component ( $kT \approx 40$  keV). Figure 6.2 shows this model and compares it with the observational data Hasinger compiled.

The composite response matrix uses a geometric detection area of  $16 \times 1.69 = 27.04 \text{ cm}^2$ . In chapter 2 we saw that the grasp of an SXR panel is  $15.4 \text{ cm}^2 \text{ sr}$ . Therefore, the appropriate size of the viewing aperture for XRB calculations is  $15.4/27.04 = 0.57 \text{ sr}$ . Using this value for the aperture size, Hasinger's model for the XRB and the composite response matrix it was possible to use XSPEC to simulate a ten minute observation of the XRB. After the simulation, the data were re-binned according to a scheme by Dr Forrest in which the bin widths increase linearly with energy. The resulting data is shown in table 1.

**Figure 6.2: The X-ray Background model spectrum and observational data compiled by Hasinger. The black line shows the model (consisting of 2 plasmas and a Bremsstrahlung component). Green data points are from ASCA, dark blue from ROSAT. Light blue indicates observations by McCammon & Sanders (1990) and Gruber's analytical representation of hard X-ray background observations from balloon experiments is shown in red.**



The data in table 1 is not so interesting in and of itself as it is useful in forthcoming analyses of observations of other sources.

The total count rate in an SXR panel, then, is 166 counts per second. It is possible to perform a rough check of this value by comparing it with observations made by ESA's recently launched XMM-Newton spacecraft. Each EPIC camera aboard Newton has a field of view of  $4.7 \times 10^{-5}$  sr, a detecting area of  $2000 \text{ cm}^2$ , and an energy bandpass and detection efficiency very similar to CATSAT's SXR. Therefore, EPIC's grasp is approximately 166 times less than that of one SXR panel and should see approximately one count a second from the diffuse soft X-ray background. Sembay (2000) reports that this is indeed the case.

**Table 1: A simulated 10 minute observation of the XRB**

Bin Number	Centroid (keV)	Counts
1	0.56	4315
2	0.68	6577
3	0.83	6868
4	1.01	10404
5	1.24	9720
6	1.52	11180
7	1.85	7529
8	2.26	5772
9	2.77	6851
10	3.38	7626
11	4.13	7330
12	5.05	5955
13	6.17	4263
14	7.55	2580
15	9.22	1465
16	11.27	763
17	13.78	379
18	16.84	181
19	20.59	81
20	24.13	21

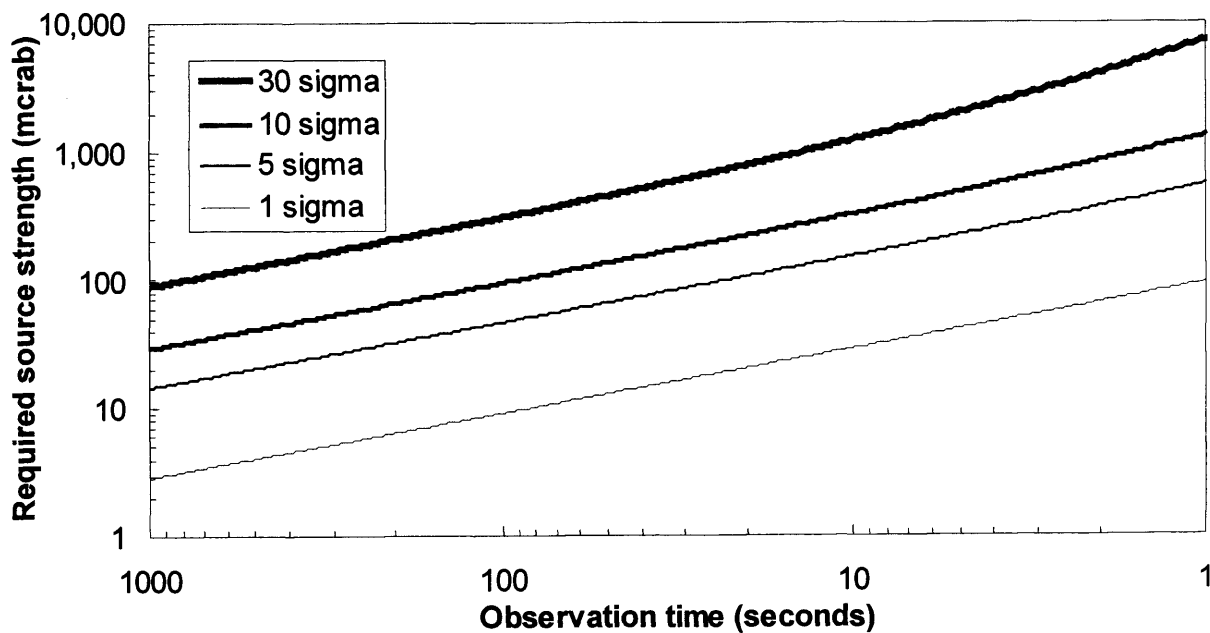
### 6.3 A simulated observation of the crab nebula

The crab is often used as a "standard candle" calibration source or as a reference for sensitivity and was included in the simulations. The model of the crab that was used was a simple one: a photoelectrically absorbed powerlaw with normalisation 10 photons/second/cm<sup>2</sup>/keV, powerlaw index 2.05 and hydrogen column density  $0.3 \times 10^{22}$  cm<sup>-2</sup>. The crab was assumed to lie directly in front of the SXR panel. XSPEC was used to simulate a 60 second observation of the crab nebula, after which the data was re-binned as before. The data is shown in table 2, which includes an extra column showing the signal to noise ratio of the data in that bin. The signal is defined as the number of source counts in that bin. The noise is defined as the square root of the sum of the number of source counts in that bin and the number of background counts in that bin (scaled from table 1). Using these same definitions and the total numbers of counts, the signal to noise ratio of the observation as a whole is 63, ie: given a one minute integration, the crab nebula represents a 63 sigma source.

**Table 2: A simulated 60 second observation of the crab nebula**

Bin Number	Centroid (keV)	Counts	S/N
1	0.56	238	9
2	0.68	410	13
3	0.83	517	15
4	1.01	964	22
5	1.24	1046	23
6	1.52	1264	26
7	1.85	827	21
8	2.26	577	17
9	2.77	626	17
10	3.38	630	17
11	4.13	542	15
12	5.05	392	12
13	6.17	251	10
14	7.55	136	7
15	9.22	69.5	5
16	11.27	33.1	3
17	13.78	15.3	2
18	16.84	6.8	1
19	20.59	2.9	1
20	24.13	0.75	0

In order to compare instrument sensitivities it is often useful to ask the question "How strong must a source with a crab-like spectrum be in order to produce a detection of a certain statistical significance in this detector in a certain time?".

**Figure 6.3: Required source strengths to produce detections of various significances as a function of time**

In figure 3 curves have been plotted that show the source strength that would be required to produce SXR observations of varying statistical significance as a function of observation time. These curves all assume normal incidence, but according to figure 2.5, a source can only be assumed to be normal for a maximum of approximately 4 minutes. Therefore, the limiting sensitivity of an SXR panel given a maximal observation of 240 seconds and a requirement of a 5 sigma detection is 30 milli-crabs. This figure is a benchmark; a useful figure in discussion of comparative sensitivity among different instruments in X-ray astrophysics.

## 6.4 Simulated observations of Gamma-ray Bursts

The third task for which the composite response was used was to investigate the likely number of gamma-ray bursts the SXR might observe each year above a five sigma level. Prior to CATSAT, the Japanese satellite GINGA had observed Gamma-ray Bursts in the energy range 2 - 20 keV. Data for the 22 brightest bursts GINGA observed, over its 4.5 year life, have been published (Strohmayer et al. 1998) and I have used these data in SXR performance simulation.

Assuming CATSAT's SXR instrument has a duty cycle  $\alpha_{SXR}$  whilst GINGA's Gamma-ray Burst Detector (GBD) had a duty cycle  $\alpha_{GBD}$  and the SXR has a field of view of  $7 \times fov_{panel}$  and the GBD had a field of view of  $fov_{GBD}$ . Then if  $n$  of the 22 GINGA bursts GINGA detected over its lifespan,  $l$ , would have constituted 5 sigma detections in the SXR, we should expect  $N$  5 sigma detections in the SXR per year:

$$N = \frac{\alpha_{SXR}}{\alpha_{GBD}} \times \frac{7 fov_{panel}}{fov_{GBD}} \times \frac{n}{l} \quad \text{5 sigma detections per year} \quad \text{Eq. 7.2}$$

Implicit within the value of  $n$  is a value for the geometric area of the detectors (27 cm<sup>2</sup>), whilst  $fov_{panel}$  explicitly defines the field of view of an SXR panel (0.803 sr, from chapter 2). We require that these be consistent with the calculated grasp of an SXR panel: 15.4 cm<sup>2</sup> sr. Two simple approaches present themselves: the geometric area can be reduced to a corrected area of 19.2 cm<sup>2</sup> while the field of view remains at 0.803 sr, or the field of view can be reduced to a corrected field of view of 0.57 sr while the area remains at 27 cm<sup>2</sup>. For completeness, we have adopted both of these approaches.

Table 3 shows the data from a simulation of the Gamma-ray Burst 870303. The observation lasted 5 seconds, the recorded duration of the burst in the GINGA dataset. The simulation assumed normal incidence and a geometric detecting area of 27 cm<sup>2</sup>. Two simulations have been performed: one without and one with an absorbing hydrogen column of density  $1.0 \times 10^{22}$

$\text{cm}^{-2}$ . This is as dense a column as is allowed by the fact that GINGA observed no column. Beneath the simulated data are four values of the total signal to noise ratio. The pair on the left correspond to the absorbing column of zero, while the pair on the right correspond to the absorbing column of  $1.0 \times 10^{22} \text{ cm}^{-2}$ . The upper two values (labelled SNR1) simply use the data as presented in the table to calculate signal to noise. The lower two (SNR2) correct the data for a geometric detecting area of  $19.2 \text{ cm}^2$  before computing the signal to noise ratio.

**Table 3: A simulated SXR observation of GRB 870303 lasting 5 seconds**

Bin	Centroid (keV)	$n_H = 0.0 \times 10^{22} \text{ cm}^{-2}$		$n_H = 1.0 \times 10^{22} \text{ cm}^{-2}$	
		Counts	S/N	Counts	S/N
1	0.56	13	2	6	1
2	0.68	21	2	10	1
3	0.83	24	3	10	1
4	1.01	42	4	16	2
5	1.24	49	4	21	2
6	1.52	72	6	37	3
7	1.85	65	6	42	4
8	2.26	68	6	52	5
9	2.77	98	8	82	7
10	3.38	133	9	119	9
11	4.13	154	11	144	10
12	5.05	146	10	140	10
13	6.17	118	10	115	9
14	7.55	76	8	75	8
15	9.22	44	6	43	6
16	11.27	23	4	23	4
17	13.78	11	3	11	3
18	16.84	6	2	6	2
19	20.59	3	1	3	1
20	24.13	1	1	1	1

SNR1	26		23
SNR2	21		18

The remaining 21 GINGA gamma-ray bursts have been used in a similar way and table 4 shows the four values of S/N from each.

**Table 4: Summary of results of GRB simulations for the 22 GINGA GRBs**

GRB	$n_H = 0.0 \times 10^{22} \text{ cm}^{-2}$		$n_H = 1.0 \times 10^{22} \text{ cm}^{-2}$	
	SNR1	SNR2	SNR1	SNR2
900126	65	53	58	48
870521	64	50	52	40
910429	53	41	39	30
881009	42	33	23	18
870707	29	22	22	17
870303	26	21	23	18
900901	26	19	20	15
900322A	24	18	20	15
900221	21	16	15	11
901001	21	16	16	12
890704	17	13	14	11
880205	13	10	10	7
880725	13	10	11	8
880830	12	9	9	7
890929	11	8	8	6
870414	9	7	8	6
900623	9	7	8	6
870902	8	6	6	5
900928	5	3	4	3
910717	5	3	4	3
910814	4	3	3	2
881130	3	2	2	2

Given that  $\alpha_{GBD} \approx 0.5$ ,  $\alpha_{SXR} \approx 0.6$ ,  $fov_{GBD} \approx \pi$  sr and  $l \approx 4.5$  years, we can use the data in table 4 and equation 7.2 to calculate  $N_{5\sigma}$ , the expected annual number of 5 sigma events, and  $N_{30\sigma}$ , the annual expected number of 30 sigma events. These results are shown in table 5:

**Table 5: Summary of predicted burst rates**

		$N_{5\sigma}$	$N_{30\sigma}$
$n_H = 0.0 \times 10^{22} \text{ cm}^{-2}$	SNR1	6.8	1.4
	SNR2	8.6	1.9
$n_H = 1.0 \times 10^{22} \text{ cm}^{-2}$	SNR1	6.1	1.0
	SNR2	8.6	1.4

So, in a period of one year we should expect between 6 and 9 five sigma detections and between 1 and 2 thirty sigma detections. These values should be regarded as upper limits since all values of SNR were calculated assuming normal incidence. A proper account of off-axis response could be made in the future using Monte-Carlo style simulation of SXR observations of randomly occurring GRBs.



The original proposal for CATSAT (Forrest et al. 1994) contained a broadly similar analysis of observed burst rates and determined that approximately 60 five sigma events could be expected per year. Clearly, this current work produces estimates that compare very poorly. The earlier work used a more complex Monte-Carlo simulation programme which no longer exists and the description in the proposal contains no hint of why the two estimates should differ so widely. However, there is an example spectrum given in the proposal: a photoelectrically absorbed powerlaw with hydrogen column density  $0.062 \times 10^{22} \text{ cm}^{-2}$ , powerlaw index 0.7 and normalisation factor  $28 \text{ photons cm}^{-2} \text{ s}^{-1} \text{ keV}^{-1}$ . The proposal goes on to say that this spectrum produced a count rate of  $6943 \text{ s}^{-1}$  in a detector with a bandpass of 0.5 to 10 keV, and an area of  $36 \text{ cm}^2$ , though the quantum efficiency is not given. I have used the given spectral parameters to re-produce this spectrum in XSPEC, which calculates the flux from 0.5 to 10 keV to be  $103 \text{ photons cm}^{-2} \text{ s}^{-1} \text{ keV}^{-1}$ . Assuming a detector area of  $36 \text{ cm}^2$  and a broad band quantum efficiency of 50%, this should produce a count rate of  $1854 \text{ s}^{-1}$ , a factor of 3.7 less than the count rate in the proposal. The reason for this discrepancy is not known and without the original programme code it will probably remain that way. However, there are interesting consequences if we assume this factor was carried through all of the analysis. For bright GRBs, the size distribution of GRBs follows a  $-3/2$  powerlaw, so a factor of 3.7 in burst flux corresponds to a factor of 7.25 in event frequency. This is sufficient to reduce the 60 events per year estimated in the proposal to only 8.3 events per year, a value consistent with my own estimates given in table 5.

## 6.5 Fitting models to simulated observations of Gamma-ray Bursts

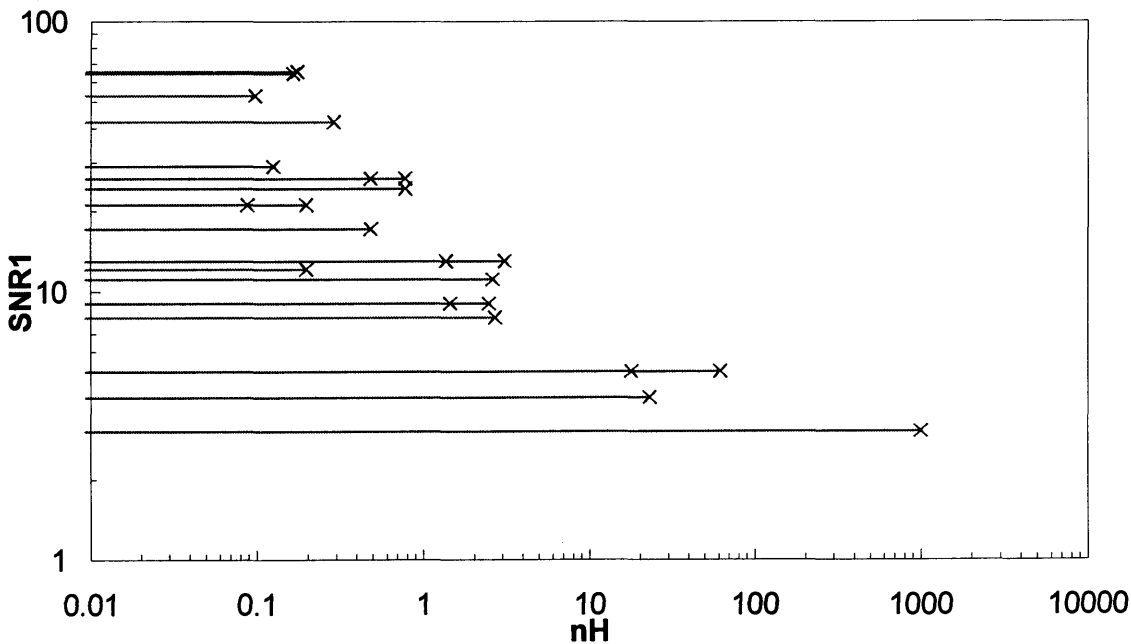
One of CATSAT's most important initial goals was to determine, to within an order of magnitude, the hydrogen column density between Earth and observed Gamma-ray Bursts. In order to evaluate the SXR's ability to provide suitable data to achieve this goal I have taken the following steps:

1. Select a GINGA gamma-ray burst for simulation
2. Simulate a 600 second observation by an SXR panel of Hasinger's soft X-ray background, using XSPEC and the composite response function.
3. Simulate an observation by an SXR panel of the background plus the GINGA burst using XSPEC and the composite response function. Assume an intervening column of density zero. Assume normal incidence. Observation duration is taken from GINGA data.

4. Read the simulated background observation into XSPEC and fit the background model to it.
5. Read in the simulated observation of the background plus the GINGA burst. Retain the background model produced by step four. Assume that the HXR and DGS will accurately constrain the burst normalisation  $A$  and the high energy powerlaw index  $\beta$ . If the energy at which the two powerlaws change over is above 20 keV, then further assume that the HXR and DGS will also accurately constrain the low energy powerlaw index  $\alpha$  and the break energy  $E_0$ . Fit the remaining parameters (either  $n_H$ , or  $n_H$ ,  $\alpha$  and  $E_0$ ) of the photoelectrically absorbed Band model to the observation.
6. After fitting, ask XSPEC to determine the 3 sigma (=99.73% confidence) interval for the density of the photoelectrically absorbing column.
7. Repeat for all remaining bursts.

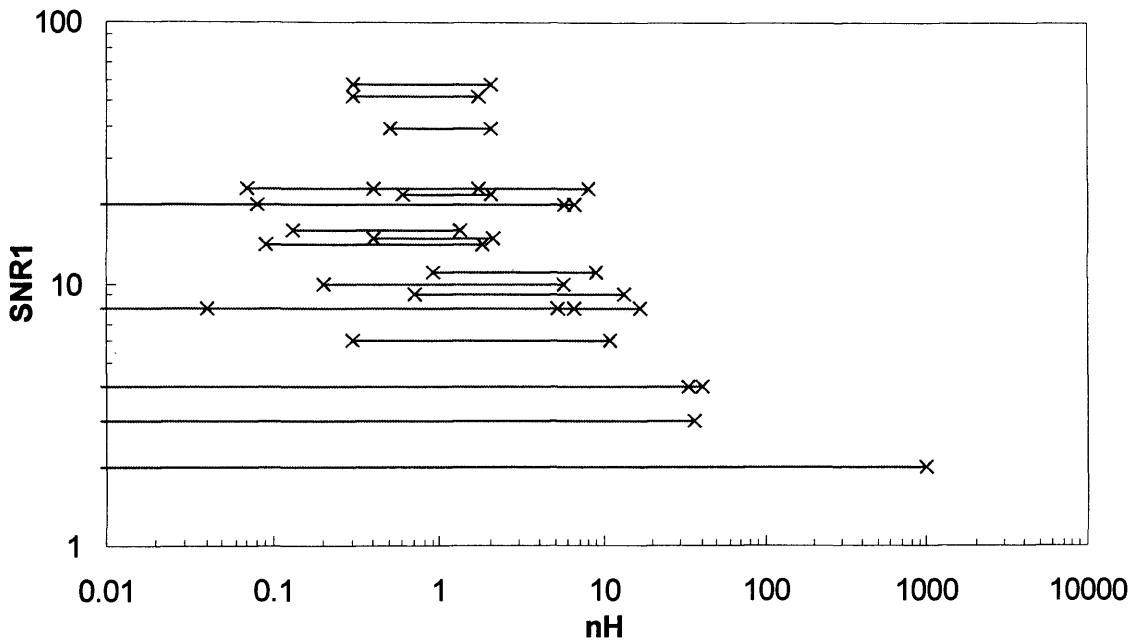
The results of this exercise are shown in figure 6.4. The 3 sigma confidence interval for  $n_H$  for each burst is shown as a horizontal line. The vertical position of the line shows the value of SNR1 for that burst taken from table 4. All of the confidence ranges extend downwards to the minimum allowable value of  $n_H$  of zero. The maximum allowable value of  $n_H$  was  $1000 \times 10^{22}$  cm<sup>-2</sup>. The chart shows that, in general, bursts with poorer SNR1 produced less well constrained values of  $n_H$ , as one would expect.

**Figure 6.4: Confidence ranges of fitted  $n_H$  for the GINGA bursts when input  $n_H$  was zero.**



For bursts having zero intervening column, we would like the confidence interval to exclude column densities of  $1 \times 10^{22} \text{ cm}^{-2}$  or greater. Of the 22 Gamma-ray Bursts used here, 12 produced sufficiently good data to constrain the fit in this way. Using equation 7.2, we can use this number to predict that if bursts **do** have no absorbing column, then of the approximately 7 bursts we expect to see above 5 sigma annually, approximately 4 would have a fitted column density confidence interval that excludes  $n_H > 1 \times 10^{22} \text{ cm}^{-2}$ . This analysis was then repeated with a value of  $n_H$  of  $1 \times 10^{22} \text{ cm}^{-2}$ . The results are shown in figure 6.5.

**Figure 6.5: Confidence ranges of fitted  $n_H$  for the GINGA bursts when input  $n_H$  was  $1 \times 10^{22} \text{ cm}^{-2}$ .**



Again, the general trend is that fainter bursts produce less constraining data. For bursts having an intervening column of density  $1 \times 10^{22} \text{ cm}^{-2}$ , we would like the confidence interval to lie entirely within the range  $0.3 \times 10^{22} \text{ cm}^{-2}$  to  $3 \times 10^{22} \text{ cm}^{-2}$ . Of the 22 Gamma-ray Bursts used here, 6 produced sufficiently good data to constrain the fit in this way. Using Equation 7.2, we can use this number to predict that if bursts **do** have an absorbing column of  $1 \times 10^{22} \text{ cm}^{-2}$ , then of the approximately 6 bursts we expect to see above 5 sigma annually, approximately 2 would have a fitted column density confidence interval entirely within the range  $0.3 \times 10^{22} \text{ cm}^{-2}$  to  $3 \times 10^{22} \text{ cm}^{-2}$ .

Notice that, for simplicity, both of these simulations ( $n_H = 0$  and  $n_H = 1 \times 10^{22} \text{ cm}^{-2}$ ) have used the "reduced aperture" method of correcting SXR grasp (as used previously in calculating SNR1), not the "reduced area" method (as used previously in calculating SNR2). Furthermore, previous assumptions about normal incidence have been carried through here and so the same caveat must still apply: *These values should be regarded as upper limits. A*

*proper account of off-axis response could be made in the future using Monte-Carlo style simulation of SXR observations of randomly occurring GRBs.*

## Chapter 7

# Conclusions

This thesis has set out to investigate the behaviour of Avalanche Photodiodes as detectors of soft X-rays in the range 0.5 to 10 keV and the likely performance of CATSAT's SXR based around this technology. Both of these goals have been achieved and the results of this work are summarised in this chapter.

### 7.1 New knowledge about APDs

Chapter three introduced the basic principles of the APD and then focussed on three poorly understood properties of these devices: peak quantum efficiency (PQE), the shelf in the pulse height distribution and the associated peak fraction (PF) and the asymmetry of peaks in the pulse height distribution. New data were presented which allowed the development of new, quantitative physical models for these phenomena. PF and PQE models yielded new information about the internal structure of APDs while work on asymmetry may also prove useful in developing a better APD:

- **The PQE model** was a development of the standard model for detection efficiency in silicon based X-ray detectors. The model uses 2 dead layers (one of aluminium and one of silicon) and one sensing layer (silicon). The mean depths of these layers in our ensemble of devices were found to be  $0.193 \pm 0.005 \text{ } \mu\text{m}$ ,  $2.1 \pm 0.5 \text{ } \mu\text{m}$  and  $21 \pm 1 \text{ } \mu\text{m}$  respectively, though the errors on individual measurements were much larger (see figures 5.14, 5.15 & 5.16). These errors could be reduced in the future by recording APD spectra at more energies, for instance at a synchrotron facility.

**Lessons for future detector development:** The depth of the aluminium dead layer was effectively fixed by our requirements for optical attenuation, however if the silicon dead layer could be made thinner then PQE could be improved. If it were removed altogether, then PQE at 1 keV could double.

- **The PF model** is new and postulates three new layers within the device: a partial collection layer, a full collection and multiplication layer and a partial multiplication layer. The average depths of the boundaries of these three layers were found in chapter 6 to be  $1.3 \pm 0.3 \mu\text{m}$ ,  $37 \pm 3 \mu\text{m}$  and  $68 \pm 9 \mu\text{m}$ , though the errors on individual measurements were much larger (see figs 6.17, 6.18 & 6.19). Again, better estimates of these parameters would result from more data points.

**Lessons for future detector development:** Efforts to reduce the dead layer thickness in the PQE model would go hand in hand with thinning of the partial collection layer in the PPF model, reducing the number of counts in the shelf in the pulse height distribution. This, too, is beneficial since the shelf does not contribute usefully to the data and only obscures lower energy channels. The shelf is particularly problematic when fitting continuum spectra. At high energies the source of the shelf is not the partial collection layer at the front of the device, but the partial multiplication layer: the avalanche region itself. If a device could be manufactured with a thinner avalanche region, but with the same total gain, it would benefit from higher PF at high energy.

- **Asymmetry data** presented in chapter three led to the conclusion that peak asymmetry in the pulse height distribution from APDs is a result of gross non-uniformities in the gain of an APD across its surface caused by inhomogeneities in the doping material. Furthermore, it is these non-uniformities which dominate the spectral resolution of most APDs, even those which appear to have symmetric peaks.

**Lessons for future detector development:** Improvement of doping homogeneity would lead to a simpler detector response and a doubling of energy resolution at 6.4 keV!

During the course of this programme, more RMD APDs have been used by a single group than ever before. This experience has led to one final, crucial recommendation for future APD development: The greatest improvement that could be made to APDs would be to improve their reliability. As described in chapter 4, at the time of screening many diodes had ceased to be useful as X-ray detectors owing to dramatically increased noise, despite the great care that has been taken over their handling and storage. Since screening, devices have continued to fail and at the time of writing about half of the total stock are useless. With launch still 2 years away, efforts have begun to determine whether or not the old stock of APDs can be replaced with a newer, more reliable product from RMD. Recently, others have reported reliability problems with large area bevelled edge APDs from another manufacturer (Baron 2000), but no possible explanation has been offered.

## 7.2 The likely performance of the SXR instrument

Using our new understanding of APDs, it has been possible to create response matrices to simulate SXR performance:

- In chapter 4 a simplified SXR response was used to demonstrate that the use of a single gaussian response rather than a double gaussian makes little or no difference to the result of fitting astrophysical models to SXR data. **Consequences for CATSAT science:** A single gaussian SXR response can now be used confidently, simplifying calibration and post-launch data analysis.
- In chapter 6 a fully detailed response matrix was used to simulate observations of the crab nebula. **Consequences for CATSAT science:** The SXR's sensitivity is now known to be 30 mcrabs, given a maximal on-source integration time of 4 minutes.
- In chapter 6 a fully detailed response matrix was used to produce simulated SXR count rates from the 22 Ginga GRBs. **Consequences for CATSAT science:** The SXR is now expected to make between 6 and 9 five-sigma GRB observations and between 1 and 2 thirty-sigma GRB observations annually. This compares poorly with the earlier estimate of 60 five-sigma observations per year predicted in the CATSAT proposal. After re-examination of both analyses in co-operation with one of the authors of the earlier work, I conclude that the more recent estimate is the correct one, though insufficient information about the earlier work remains to find the root cause of the count rate overestimation. This comes as a blow to CATSAT's stated goal of expanding the number of bursts recorded in the soft X-ray regime.
- In chapter 6 a fully detailed response matrix was used to fit astrophysical models to simulated observations of the Ginga GRBs. **Consequences for CATSAT science:** SXR data should be able to distinguish between zero column and  $10^{22} \text{ cm}^{-2}$  in approximately half of all 5-sigma observations. Such a small number of density determinations is disappointing, but may yet provide an indication of burster environment dustiness. This could help to distinguish between hypernova and neutron star merger progenitor models.

# Bibliography

Antonelli, L. A., F. Fiore, L. Amati, M. Feroci, E. Costa, F. Frontera, G. Gandolfi, P. Giommi and L. Piro (1999). "BeppoSax Discovery of the X-ray Afterglow of GRB 971227." Astronomy and Astrophysics Supplement Series **138**: 435.

Anzer, U. and G. Borner (1974). Preprint. Max Planck Institute for Astrophysics.

Apparo, K. (1973). Communication to Strong, I.

Arnaud, K. Astronomical data analysis software and systems V.

Band, D., J. Matteson, L. Ford, B. Schaefer, D. Palmer, B. Teegarden, T. Cline, M. Briggs, W. Paciesas, G. Pendleton, G. Fishman, C. Kouveliotou, C. Meegan, R. Wilson and P. Lestrade (1993). "BATSE observations of gamma-ray burst spectra. I - Spectral diversity." The Astrophysical Journal **413**: 281-292.

Baron, A. Q. R. (2000). "Detectors for Nuclear resonant scattering experiments." Hyperfine Interactions **125**: 29-42.

Bisnovatyi-Kogan, G., V. Imshennik, D. Nadezhin and V. Chechetkin (1974). Preprint. Institute of Applied Mathematics of Order of Lenin. Moscow. USSR.

Boella, G. and e. al. (1996). Astronomy and Astrophysics Supplement Series **122**: 327-340.



## Bibliography

Boella, G., R. C. Butler, G. C. Perola, L. Piro, L. Scarsi and J. A. M. Bleeker (1997). "BeppoSAX, the wide band mission for X-ray astronomy." Astronomy & Astrophysics Supplement Series **122**: 299-307.

Brecher, K. and P. Morrison (1974). Astrophys. J. Lett. **187**: L97.

Bunner, A. N. (1999). Research announcement for the Compton Gamma Ray Observatory guest investigator program, NASA.

Castro-Tirado, A. J. and J. Gorosable (1999). "Optical Observations of GRB Afterglows: GRB 970508 and GRB 980326 revisited." Astronomy and Astrophysics Supplement Series **138**: 449.

Chanmugam, G. (1974). Astrophys. J. Lett **193**: L75.

Citterio, O. and e. al. (1985). SPIE Proc. **597**: 102.

Cline, T. L. (1981). "Gamma-Ray Bursts." Annals of the New York Academy of Sciences: 314-329.

Cline, T. L. (1983). "Gamma-Ray Bursts: A 1983 Overview." AIP Conference Proceedings **115**: 333-342.

Colgate, S. (1974). Astrophys. J. **187**: 333.

Colgate, S. A. (1968). Canadian J. Phys. **46**: S476.

Conradi, J. (1972). "The distribution of gains in uniformly multiplying avalanche photodiodes: experimental." IEEE Trans. Elec. Dev. **19**(6): 713-718.

Conti, G. and e. al. (1994). SPIE Proc **2279**: 101.

Coppi, B. and A. Treves (1973). Preprint Massachusetts Institute of Technology.

## Bibliography

Costa, E. (1999). "X-ray Afterglow of Gamma-Ray Bursts with BeppoSax." Astronomy and Astrophysics Supplement Series **138**: 425.

Costa, E., F. Frontera, D. Dal Fiume, L. Amati, M. N. Cinti, P. Collina, M. Feroci, L. Nicastro, M. Orlandini, E. Palazzi, M. Rapisarda and G. Zavattini (1998). "The Gamma-Ray Bursts monitor onboard SAX." Advances in Space Research **22**(7): 1129-1132.

Entine, G., G. Reiff, M. Squillante, H. B. Serreze and S. Lis (1983). "Scintillation detectors using large area silicon avalanche photodiodes." IEEE Trans. Nuc. Sci. **30**(1): 431-435.

Farrell, R. (1999). Private Communication.

Farrell, R., F. Olschner, E. Frederick, L. McConchie, K. VanDerPuye, M. R. Squillante and G. Entine (1990). "Large area silicon avalanche photodiodes for scintillation detectors." NIM **A228**: 137-139.

Farrell, R., R. Redus, J. S. Gordon and P. Gothoskar (1995). "High gain APD array for photon detection." Proc SPIE **2550**: 266-273.

Farrell, R., K. VanDerPuye, L. Cirignano, M. R. Squillante and G. Entine (1994). "Radiation detection performance of very high gain avalanche photodiodes." NIM **A353**: 176-179.

Farrell, R., K. VanDerPuye, G. Entine and M. R. Squillante (1991). "High resolution, low energy avalanche photodiode X-ray detectors." IEEE Trans. Nuc. Sci. **38**(2): 144-147.

Fishman, G. J. (1995). "Gamma-ray Bursts: An Overview." Publications of the Astronomical Society of the Pacific **107**: 1145-1151.

Fishman, G. J. (1996). "Gamma-Ray Bursts: Observational Overview." IAU Symposia **165**: 467-476.

Fishman, G. J. and C. A. Meegan (1995). "Gamma-ray Bursts." Annu. Rev. Astron. Astrophys **33**: 415-458.

Forrest, D. J. and e. al. (1994). CATSAT: A Proposal Submitted to USRA's Student Explorer Demonstration Initiative, University of New Hampshire Institute for the Study of Earth, Oceans and Space: 30.

## Bibliography

Forrest, D. (1998). Private communication.

Forrest, G. (1995). An application of avalanche photodiodes; detection of soft X-rays for the cooperative astrophysics and technology satellite (CATSAT). Electrical Engineering. Durham, University of New Hampshire: 99.

Fortescue, P. and J. Stark, Eds. (1995). Spacecraft Systems Engineering, Wiley.

Fraser, G. (1989). X-ray detectors in astronomy. Cambridge, Cambridge University Press.

Frontera and e. al. (1996). Astronomy and astrophysics Supplement Series **122**: 357-369.

Frontera, F., L. Amati, A. Castro-Tirado, E. Costa, D. Dal Fiume, M. Feroci, J. Heise, N. Masetti, J. M. Muller, L. Nicastro, M. Orlandini, E. Palazzi, E. Pian, L. Piro, M. Tavani and J. i. t. Zand (1999). "Spectral Evolution of Gamma-Ray Bursts with BeppoSax and Correlation with X-ray Afterglow Properties." Astronomy and Astrophysics Supplement Series **138**: 399-400.

Galama, T. J., R. A. M. J. Wijers, P. M. Vreeswijk, P. J. Groot, J. Van Paradijs, C. Kouveliotou, M. Robinson, M. Bremer, R. G. Strom and N. Tanvir (1999). "Physical Parameters of GRB 970508 from its afterglow synchrotron emission." Astronomy and Astrophysics Supplement Series **138**: 451.

Gorosabel, J., A. J. Castro-Tirado, H. Pederson, J. Greiner, D. Thompson, M. Guerrero, A. Oscoz, N. Sabalisch, E. Villaver and L. Lund (1999). "Optical and Near-Infrared Observations of the BRB 970616 Error Box." Astronomy and Astrophysics Supplement Series **138**: 455.

Grindlay, J. and G. Fazio (1974). Astrophys. J. Lett. **187**: L93.

Guarnieri, A., A. Castro-Tirado, C. Bartolini, M. Lolli, N. Masetti, A. Piccioni, F. Zavatti, J. Gorosabel, Y. Aguilar, R. Kohley, G. M. Beskin, M. R. Zapatero-Osorio, R. Rebolo, R. Corradi, M. Guerrero, S. Kemp, J. Greiner, M. Deitrich, F. J. Zickraf, E. Costa, M. Feroci, F. Frontera, L. Piro, L. Nicastro and E. Palazzi (1999). "An Optical Counterpart to GRB 971227 ?" Astronomy and Astrophysics Supplement Series **138**: 457.

Hanlon, L., L. Metcalfe, M. Delaney, R. Laureijs, B. McBreen, N. Smith, B. Altieri, A. Castro-Tirado, E. Costa, M. Feroci, F. Frontera, T. Galama, J. Gorosabel, P. Groot, J. Heise, C. Kouveliotou, E. Palazzi, J. Van Paradijs, L. Piro and M. Kessler (1999). "Observations of GRBs With the Infrared Space Observatory." Astronomy and Astrophysics Supplement Series **138**: 459.

## Bibliography

- Harding, A. K. (1991). "The Physics of Gamma-ray Bursts." Physics Reports **206(6)**: 327-391.
- Hartmann, D. H. (1994). "Taking Stock of Gamma-ray Bursts." Science **263**: 47-49.
- Hartmann, D. H. (1996). "Theoretical models for Gamma-Ray Bursts." Astronomy and Astrophysics Supplement Series **120**: 31-41.
- Hartmann, D. H. and S. E. Woosley (1995). "Models for Classical Gamma-Ray Bursts." Advances in Space Research **15(5)**: 143-152.
- Harwit, M. and E. Salpeter (1973). Astrophys. J. Lett. **186**: L37.
- Hasinger, G. (1996). "The extragalactic X-ray and gamma-ray background." Astronomy and Astrophysics Supplement **120**: 607-614.
- Higdon, J. C. and R. E. Lingenfelter (1990). "Gamma-Ray Bursts." Annu. Rev. Astron. Astrophys. **28**: 401-436.
- Hjorth, J., H. Pederson, A. O. Jaunson and M. I. Anderson (1999). "GRB Afterglow Studies at the Nordic Optical Telescope." Astronomy and Astrophysics Supplement Series **138**: 461.
- Horack, J. M. (1991). Development of the Burst and Transient Source Experiment (BATSE). NASA Reference Publication 1268, NASA.
- Hoyle, F. and D. Clayton (1974). Preprint Rice University.
- Hurley, K. (1980). Observational Properties of Gamma-ray Bursts. Non-Solar Gamma-Rays. R. Cowsik and R. D. Wills, Pergamon Press: 123-139.
- Hurley, K. (1983). "Gamma-Ray Bursts." AIP Conference Proceedings **101**: 21-35.
- Hurley, K. (1989). Cosmic Gamma-ray Bursts. Cosmic Gamma-rays, Neutrinos and Related Astrophysics. M. Shapiro and E. Wefel. Boston, Kluwer: 337-379.

## Bibliography

Hurley, K. (1989). "Cosmic Gamma-ray Bursts (An Overview of Recent Results)." Annals of the New York Academy of Sciences: 442-459.

Hurley, K. (1993). "A Review of Recent Results on Cosmic Gamma-ray Bursts." Adv. Space Res. **13**(12): 679-685.

Hurley, K. (1999). "Solved and Unsolved Mysteries in Cosmic Gamma-Ray Bursts." Astronomische Nachrichten **320**(4-5): 269-272.

Jager, R., W. A. Mels, A. C. Brinkman, M. Y. Galama, H. Goulooze, J. Heise, P. Lowes, J. M. Muller, A. Naber, A. Rook, R. Schuurhof, J. J. Schuurmans and G. Wiersma (1997). "The Wide Field Cameras onboard the BeppoSAX X-ray Astronomy Satellite." Astronomy and Astrophysics Supplement Series **125**: 557-572.

Klebesadel, R. W., I. B. Strong and R. A. Olson (1973). "Observations of Gamma-Ray Bursts of cosmic origin." The Astrophysical Journal **182**: L85-L88.

Lamb, D., F. Lamb and D. Pines (1973). Nature Phys. Sci. **246**: 52.

Lamb, D. Q. (1984). "Physics of Gamma-ray Bursts." Annals of the New York Academ of Sciences: 237-281.

Lamb, D. Q. (1988). Theories of Gamma-Ray Burst Spectra. Nuclear Spectrsoscopy of Astrophysical Sources. N. Gehrels and G. H. Share. New York, AIP: 265-284.

Locker, R. J. and G. C. Huth (1966). "A new ionizing radiation detection concept which employs semiconductor avalanche amplification and the tunnel diode element." App. Phys. Lett. **9**(6): 227-230.

Masetti, N., E. Pian, E. Palazzi, L. Amati, T. J. Galama, L. Nicastro, P. M. Vreeswijk, F. Frontera and J. Van Paradijs (1999). "Broad-Band Spectral Evolution of GRB Afterglows." Astronomy and Astrophysics Supplement Series **138**: 453.

McIntyre, R. J. (1966). "Multiplication noise in uniform avalanche diodes." IEEE Trans. Elec. Dev. **13**(1): 164-168.

## Bibliography

McIntyre, R. J. (1972). "The distribution of gains in uniformly multiplying avalanche photodiodes: theory." IEEE Trans. Elec. Dev. **19**(6): 703-712.

Meszaros, P. (2000). "Gamma-Ray Bursts and Bursters." Nuclear Physics B (Proc. Suppl.) **80**: 63-77.

Meszaros, P. and M. J. Rees (1993). "Relativistic Fireballs and Their Impact on External Matter - Models for Cosmological Gamma-Ray Bursts." Astrophysical Journal **405**(1): 278-284.

Mitrofanov, I. G. (1995). "What We Knew, What We Know and What We Will Know about Cosmic Gamma-ray Bursts." Space Science Reviews **74**(3-4): 417-426.

Murakami, T., M. Fuji, K. Hayashida, M. Itoh, J. Nishimura, T. Yamagami, J. P. Conner, W. D. Evans, E. E. Fenimore, R. W. Klebesadel, A. Yoshida, I. Kondo and N. Kawai (1988). "Evidence for cyclotron absorption from spectral features in gamma-ray bursts seen with Ginga." Nature **335**: 234-235.

Murakami, T., F. Masami, K. Hayashida, M. Itoh, J. Nishimura, T. Yamagami, A. Yoshida, J. P. Conner, W. D. Evans, E. E. Fenimore, R. W. Klebesadel, K. M. Spencer, H. Murakami, N. Kawai, I. Kondo and M. Katoh (1989). "The Gamma-Ray Burst Detector System on Board Ginga." Publ. Astron. Soc. Japan **41**: 405-426.

Narayan, R., B. Paczynski and T. Piran (1992). "Gamma-Ray Bursts as the Death Throes of Massive Binary Stars." Astrophysical Journal **395**(2): L83-L86.

Narlikar, J., K. Appa Rao and N. Dadhich (1974). Nature **251**: 590.

Nicastro, L., L. Amati, L. A. Antonelli, E. Costa, G. Cusumano, M. Feroci, F. Frontera, E. Palazzi, E. Pian and L. Prio (1999). "The X-ray Afterglow of GRB 980519." Astronomy and Astrophysics Supplement Series **138**: 437.

Owens, A. and B. Schaefer (1993). "Solving the Gamma-ray Burster Problem." Comments Astrophys. **17**(2&3): 119-124.

Owens, A., B. E. Schaefer and S. Sembay (1995). "Deriving Gamma-ray Burster Distances from Soft X-ray Measurements." Astrophysical Journal **447**(1): 279-288.

## Bibliography

Owens, A., S. Sembay and B. E. Schaefer (1995). "Deriving the GRB distance scale." Astrophysics and Space Science **231**(1-2): 449-452.

Pacini, F. and M. Ruderman (1974). Nature **251**: 399.

Paczynski, B. (1993). "Gamma-ray Bursts." Annals of the New York Academy of Sciences: 321-330.

Parmar, A. e. a. (1996). Astronomy and Astrophysics Supplement Series **122**: 309-326.

Piro, L., E. Costa, M. Feroci, G. Stratta, F. Frontera, L. Amati, D. Dal Fiume, L. A. Antonelli, J. Heise, J. I. t. Zand, A. Owens, A. N. Parmar, G. Cusumanu, M. Vietri and G. C. Perola (1999). "Iron Line Signiatures in X-ray Afterglows of GRB by BeppoSax." Astronomy and Astrophysics Supplement Series **138**: 431.

Pringle, J. and X. Fabian (1974). from Shaham, J.

Ramaty, R. and J. Cohen (1973). . Conference on Transient Cosmic Gamma and X-ray Sources, Los Alamos, N.M.

Redus, R. and R. Farrell (1996). "Gain and noise in very high gain avalanche photodiodes: theory and experiment." SPIE **2859**: 288-297.

Rees, M. J. (1999). "Some Comments on Triggers, Energetics and Beaming." Astronomy and Astrophysics Supplement Series **138**: 491-497.

Rees, M. J. (2000). "A Review of Gamma-Ray Bursts." Nuclear Physics A **663 & 664**: 42c-55c.

Rees, M. J. and P. Meszaros (1992). "Relativistic Fireballs - Energy - Conversion and Time-Scales." Monthly Notices of the Royal Astronomical Society **258**(2): 41-43.

Reiff, G., M. R. Squillante, H. B. Serreze and G. Entine (1983). "Large area silicon avalanche photodiodes: photomultiplier tube alternate." MRS Symposium proceedings **16**: 131-140.

## Bibliography

Ruderman, M. (1975). "Theories of Gamma-ray Bursts." Annals of the New York Academy of Sciences **262**: 164-180.

Ruffini, R. (1975). Annals of the New York Academy of Sciences **262**.

Sembay, S. (2000). Private Communication.

Sofia, S. and H. Van Horn (1974). Preprint.

Stekker, F. and K. Frost (1973). Nature Phys. Sci. **245**: 70.

Strohmayer, T. E. and E. E. Fenimore (1998). "X-ray spectral characteristics of GINGA Gamma-Ray Bursts." The Astrophysical Journal **500**: 873-887.

Strong, I., R. Klebesadel and R. Olson Preprint. Los Alamos Observatory.

Squillante, M. R., R. Farrell, J. C. Lund, F. Sinclair, G. Entine and K. R. Keller (1986). "Avalanche diode low energy X-ray and nuclear particle detector." IEEE Trans. Nuc. Sci. **33**(1): 336-339.

Squillante, M. R., G. Reiff and G. Entine (1985). "Recent advances in large area avalanche photodiodes." IEEE Trans. Nuc. Sci. **32**(1): 563-566.

Taylor, G. B., A. J. Beasley, D. A. Frail, S. R. Kulkarni and J. E. Reynolds (1999). "VLBI Observations of GRB Afterglows." Astronomy and Astrophysics Supplement Series **138**: 445.

Teegarden, B. J. (1998). "Spectroscopy of Gamma-Ray Bursts: An Overview." Advances in Space Research **22**(7): 1083-1092.

Vedrenne, G. (1981). "Cosmic Gamma-ray Bursts." Phil. Trans. R. Soc. Lond. A **301**: 645-658.

Vedrenne, G. and G. Chambon (1983). "Cosmic Gamma-Ray Bursts." Space Science Reviews **36**(3): 319-335.



## Bibliography

- Verter, F. (1982). "Cosmic Gamma-ray Bursts." Physics Reports **81**(4): 293-349.
- Vestrand, W. T., D. J. Forrest, K. A. Levenson, C. Whitford, D. Fletcher-Holmes, A. Wells and A. Owens (1999). "CATSAT: A small satellite for studying Gama-Ray Bursts." AIP Conference Proceedings **499**: 156-165.
- Vreeswijk, P. M., T. J. Galama, A. N. Owens, T. oosterbroek, T. Geballe, J. Van Paradijs, C. Kouveliotou, N. Tanvir, E. Pian, E. Palazzi, F. Frontera and N. Masetti (1999). "The X-ray, Optical and Infrared Counterpart to GRB 980703." Astronomy and Astrophysics Supplement Series **138**: 447.
- Woosley, S. E. (1984). "The Theory of Gamma-ray Bursts." AIP conference proceedings **115**: 485-511.
- Woosley, S. E. (1993). "Gamma-Ray Bursts from Stellar Mass Accretion Disks Around Black-Holes." Astrophysical Journal **405**(1): 273-277.
- Woosley, S. E. (1995). "Gamma-ray Bursts - What are they?" Annals of the New York Academy of Sciences **759**: 446-449.
- Yoshida, A., T. Murakami, M. Itoh, J. Nishimura, T. Tsuchiya, E. Fenimore, R. Klebesadel, W. D. Evans, I. Kondo and N. Kawai (1989). "Soft X-Ray Emission from Gamma-Ray Bursts Observed with Ginga." Publ. Astron. Soc. Japan **41**: 509-518.
- Zwicky, F. (1974). Astrophys. Space Sci. **28**: 111.

## Appendix A

# **Calibration Procedures for CATSAT SXR Panels**



# Calibration procedures for CATSAT SXR panels

David F-H  
March 2000

This document describes several important procedures used in the calibration of CATSAT's SXR panels. It does not cover the assembly & fitting of SXR panels as CHW & DJW carry out these tasks. Furthermore, basic operation of the JET-X test facility is not described here as this is already covered elsewhere.

## APD groupings

The final APD groupings are given in the table below.

**Table 1**

Flight 1	Flight 2	Flight 3	Flight 4	Flight 5	Flight 6	Flight 7
96	90	55	NEW 138	47	92	35
117	127	120	NEW 133	28	9	76
1524-7	1524-6	58	NEW 139	89	126	77
114	121	13	87	30	46	48
11	33	12	119	31	74	49
81	29	NEW 132	42	107	56	10
116	79	17	27	105	7	15
57	51	63	67	5	40	1524-8
71	94	36	102	19	43	24
1	21	100	80	39	45	73
69	72	66	18	8	125	68
34	91	111	106	20	75	70
103	82	16	113	118	122	41
112	104	59	3	86	32	37
		38	22			NEW 135
		110	64			NEW 134

## Routine maintenance

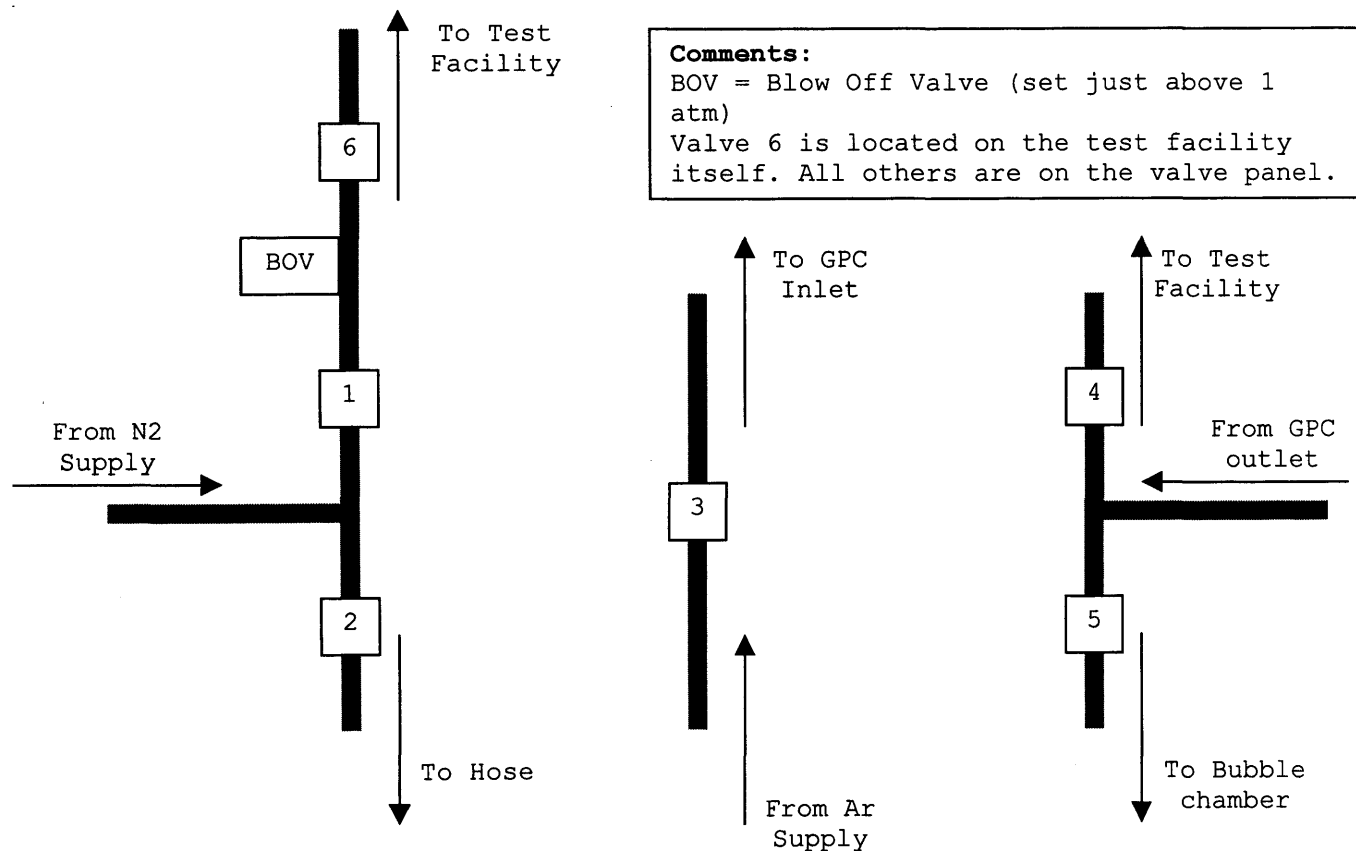
APDs being stored in the 2 glove boxes are kept under dry Nitrogen. The humidity levels in these 2 boxes can be monitored with the bench hygrometer in AIT. It is necessary to check the reserves of the 2 Nitrogen bottles in AIT daily, and replace them as soon as they are empty. On a Friday it is necessary to ensure that reserves sufficient to last through the weekend.

When an APD is turned on, its operational characteristics may take up to 24 hrs to settle. For this reason it is necessary for diodes to be continually biased day and night during the calibration period. This in turn imposes a requirement for the diodes to be kept at their operational temperature of  $-40^{\circ}\text{C}$ . This is achieved by using a Liquid Nitrogen pump and a timer. The timer has been set to pump for approximately 70 seconds every three hours commencing at noon. At this rate the dewar requires refilling every 24 hours. This should be performed about 10 minutes before a re-fill, which should be monitored and supplemented manually if necessary. After the re-fill the LN2 level should be a couple of centimetres below the brim of the bucket.

Since the APDs are continually under bias, they and their electronics are susceptible to damage should the pressure increase. This possibility has been addressed by incorporating a High Voltage Interlock (HVI) which automatically shuts off the HV supply should the cryostat pressure rise. The HV will not come back on again without human intervention even if the pressure subsequently falls. The "trip" point of this device is difficult to set, but now appears to be at a reasonable level.

In general, the procedures for pumping & back filling the system are the same as those for EPIC. There is an added complication owing to the presence of a Gas filled Proportional Counter (GPC) in the facility, whose internal pressure must not be lower than the pressure that surrounds it. If this rule is not strictly observed, the GPC window, which is difficult to manufacture and calibrate, will be broken. In order to meet this requirement, a system of valves has been added to the facility for use during pump down and back filling. Figure 1, below, shows their arrangement.

Figure 1



When the cryostat is not on the test facility and the Cryostat end of the test facility is at 1 atm, valves 1, 2, 3, 4 & 6 should be closed and valve 5 should be open. The cryostat can be fitted and the chamber pumped down without any further changes.

Once operational pressure has been reached ( $<4 \times 10^{-5}$  mbar), valve 3 can be opened and shut to operate the GPC. **Always check that valve 5 is open before opening valve 3.** The gas flow through the GPC can be monitored using the bubble chamber.

When the time comes to let the cryostat back up to 1 atm and the gate valve is shut, valves 3 and 5 must be closed and then valve 4 must be **slowly** opened. This connects the interior of the GPC to the cryostat so that there should be no pressure acting on the window during let up. The pressure will rise as the Ar gas from the GPC empties into the cryostat. Next open valve 6 then valve 1 to begin the back filling. When the pressure inside the cryostat exceeds 1 atm, the blow off valve will open to relieve the pressure. Valve 1 should now be closed. The cryostat may then be removed. After the cryostat is off, close valve 6 and valve 4 and open valve 5. This returns the valves to their original state. Valve 3 may be opened and closed to observe gas flow through the bubble chamber and confirm the health of the GPC window. **Always check that valve 5 is open before opening valve 3.**

If in doubt remember the golden rules: **The pressure inside the GPC must not be less than that which surrounds it as the GPC window is only supported on the outside. Always check that valve 5 is open before opening valve 3.**

Valve 2 is used to operate the Nitrogen hose for general lab purposes and should not be open if valve 1 is open.

# Aluminising

J Pearson has written up the procedure for APD aluminising. Further to his document, the following information is necessary:

1. Using the agreed geometrical arrangement, 1450 Angstroms on the crystal monitor is equivalent to 2000 Angstroms on the APD.
2. In order to heat the APDs to the desired 60°C, the heater should be set to 15% power and turned off when the thermistor resistance reaches 30 k $\Omega$  (this takes approx. 35 minutes). The temperature should then "coast" the rest of the way to 60°C (20 k $\Omega$ ) at which time GGD and deposition may take place.



## Turning on the diodes

When the cryostat has been mounted onto the test facility and all of the electrical connections have been made, the system can be pumped down. This should generally be left to take place overnight. When the cryostat has been evacuated, the cooling may commence which may take up to 2 hours.

Once the system is at  $-40^{\circ}\text{C}$  and the pressure is less than  $4 \times 10^{-5}$  mbar, APD turn on may begin. The proper sequence of events follows:

1. Turn on the DC power supply to the electronics chain. Start the Calibration software on the lab PC. Ensure that the high voltage setting at the top of the main window is in the off position. Ensure that all of the voltages in the high voltage control window are set to zero and that no HV channels are enabled. Ensure that no data channels are enabled in the "sensors" window. Turn on the high voltage supply on the bench and increase bias to 2000 V. Enable all channels in the high voltage window and turn on the high voltage setting at the top of the main screen.
2. Turn on the first data channel in the "sensors" window and set the threshold to  $\approx 100$  channels.
3. Turn on the display of data from the newly activated channel in the main window using the buttons at the top of the screen and start collecting data. Slowly reduce the software threshold until the low energy noise tail can be seen.
4. Move to the High Voltage control window and increase the voltage to the diode in use to 200 volts. This should cause the noise in the diode to drop. Lower the software threshold until the noise is visible again. If the noise in the diode undergoes a dramatic

increase, reduce the voltage to zero, make a note in the log and call DFH.

5. Repeat step 4, increasing the bias to 1000, 1200 and finally 1400 volts. If the noise in the diode undergoes a dramatic increase during any of these changes, reduce the voltage to the previous value, make a note in the log and move on to the next diode.
6. If all is well when the bias has reached 1400 volts, stop data acquisition and clear the data before deselecting the current diode in the "sensors" window.
7. Repeat steps 2 through 6 till all of the diodes in the panel have been biased. Any diodes that could not be operated at the full 1400 volts should now be tried again.
8. Leave the diodes to settle for an hour or so.
9. Turn on the Kevex X-ray source and set the voltage to 14.5 kV and the current to 95  $\mu$ A. Select the Ti target on the target wheel.
10. Move through the diodes as before, adjusting their voltages to centre the Ti X-ray peak on channel 180. It will be necessary to use the rotator on the rear of the cryostat to ensure that the X-ray beam illuminates the diode being examined. Make a note of the final biases in the log. Select all diodes at once and adjust the software threshold so the noise tail is comparable with the X-ray peak. Make a note of this threshold in the log.
11. The diodes must be allowed to settle for another 2 hours. Repeat step 10. The diodes are now ready for use.

Each day before testing begins step 10 should be repeated to ensure gain stability in the APDs.

## Recording of Kevex lines

1. Ensure valve 5 is open. Turn on gas flow into GPC by opening valve  
3. Regulate flow to around 1 bubble per second. Wait for 15 minutes then turn on the High Voltage. It should not be necessary for the HV to be adjusted.
2. Turn on the Kevex X-ray source. Set the voltage to 14.5 kV and the current to 95  $\mu$ A. Select desired X-ray line using target wheel.  
Table 2 shows the lines that are available.

**Table 2**

Target	Energy (keV)	Wheel angle
Mg	1.253	252°
Al	1.487	72°
Si	1.740	324°
Ti	4.511	288°
Fe	6.404	216°
Cu	8.048	180°

3. Connect the GPC motor cable to the GPC hosing. Insert the GPC into the beam. Remove the GPC motor cable from the GPC housing (this minimises noise). Record a few hundred X-ray counts from the GPC using the PCA software. Set a ROI around the X-ray Peak(s) (remember to include the escape peak where appropriate) and calculate the time that would be required to produce 100 000 counts in the GPC. Write this value in the log and compare it with that in table 3 below.

**Table 3**

Target	Approx. GPC integration time (min)
Mg	278
Al	73
Si	49
Ti	27
Fe	42
Cu	93

4. Integrate 100 000 counts in the GPC. Set a ROI around the X-ray Peaks(s) and calculate the count rate in the detector and error. Note this value in the log. Save this data file under the name "GPCnn.SPM", where nn is the source name (eg: Fe, Mg etc...). Note the file name and other details in the log. Only one GPC integration is needed per Kevex line. Re-connect the GPC motor cable, withdraw the GPC from the beam and disconnect the motor cable.
5. The Kevex beam illuminates an entire quadrant of the SXR panel at a time, making it necessary to perform only four integrations per X-ray line. Select the first quadrant to calibrate using the rotator on the rear of the cryostat. Select the corresponding data channels in the CATSAT calibration software using the buttons at the top of the screen.
6. Record a few hundred X-ray counts from the quadrant of APDs. Set a ROI around the X-ray Peak. Examine the output of each of the four channels individually to confirm that they all have approximately the same number of counts. Calculate the time that would be required to produce 100 000 counts in a single diode. Write this value in the log and compare it with that in table 4 below.

**Table 4**

Target	Approx. APD integration time (min)
Mg	73
Al	20
Si	16
Ti	10
Fe	13
Cu	28

7. Integrate 100 000 counts in each of the four illuminated APDs simultaneously. Save the data to an Excel file, filling in all of the required details in the software. File names should be simple

and should reflect the panel being used, eg: "flight2file1.xls". Sheet names should be composed from the target being used and the channels being illuminated eg: "Fe 0 - 3". File names, sheet names, integration times etc... should all be noted in the log.

8. Use the rotator on the rear of the cryostat to illuminate the next quadrant of the panel and then select the corresponding data channels in software.
9. Repeat steps 7 & 8 until data has been gathered from all four quadrants of the panel. Notice that while data from one quadrant is being recorded, data from the previous panel can be analysed as described below.
10. Turn off the HV for the GPC and close valve 3.

## Analysis of Kevex lines

1. Launch Microsoft Excel on the analysis PC. Open the recently recorded data file. Move to the worksheet containing the new data. This will show one column of data from each active diode.
2. Move to the column representing the first **illuminated** diode. **Copy** the data from that column. Open the analysis workbook appropriate that diode.
3. Move to the worksheet of the same name as the X-ray target just used. **Paste** the new data into the column labelled "Counts".
4. Fill in the Integration time in the top left corner.
5. Click on the "Analyse" button. When each round of "solving" is complete the user will be asked to accept or reject the results. Unless the computer indicates that an error has taken place, accept the result. If an error does occur, call DFH.
6. Move to the sheet entitled "Analysis". Find the column "GPC rate". Move down this column to the row representing the appropriate X-ray energy. Fill this cell in with the GPC rate calculated earlier. Also fill in the cell to the right with the error calculated earlier.
7. Move back to the data workbook. Sum the total counts from ALL active data channels. Write this sum in the log. Divide this sum by the integration time and write this figure (the "total rate") down in the log book also. Take the square root of this sum, divide the result by the integration time and write this figure (the "total rate error") down in the log book also. Move back to the analysis work book.

8. Find the column "Total rate". Move down this column to the row representing the appropriate X-ray energy. Fill this cell in with the total rate just calculated. Also fill in the cell to the right with the total rate error. Close the analysis workbook, saving changes.
9. Repeat steps 2 - 8 for each subsequent illuminated diode until all four have been analysed.

## Recording of Soft X-ray lines

1. Check that the cryostat is located at +13.2 mm vertically and 0 mm horizontally.
2. Ensure valve 5 is open. Turn on gas flow into GPC by opening valve
3. Regulate flow to around 1 bubble per second. Wait for 15 minutes then turn on the High Voltage. It should not be necessary for the HV to be adjusted.
3. Set crystal, monochromator arm and crystal offset as appropriate for desired source (see table 5).

Table 5

Target	Energy (keV)	Crystal	Arm angle	Crystal offset
F	0.677	PbSt	338.9°	5.94 $\mu\text{m}$
Na	1.041	RAP	303.3°	5.31 $\mu\text{m}$
Cl	2.622	RAP	338.9°	5.38 $\mu\text{m}$

4. Turn on the Soft X-ray source. Set the current to 5.5 mA and the voltage to 4 kV.
5. Connect the GPC motor cable to the GPC hosing. Insert the GPC into the beam. Remove the GPC motor cable from the GPC housing (this minimises noise).
6. Record a few hundred X-ray counts from the GPC using the PCA software. Set a ROI around the X-ray Peak and make a note of the count rate at this value of crystal offset.
7. Repeat step 6 for 10 different crystal offsets spaced 0.02  $\mu\text{m}$  apart over a range of offsets centred on the initial value. Use the resulting data to decide whether this range includes the peak flux. If it does, move the crystal back to the peak setting. If it does not then continue scanning the crystal offset.



8. Once the crystal correction has been set, the voltage should be adjusted to the maximum possible before significant beam contamination occurs. Table 6 shows usual values.

**Table 6**

Target	Voltage (kV)
F	1.2
Na	2.25
Cl	4.25

9. Record a few hundred X-ray counts from the GPC at these new settings. Calculate the time that would be required to produce 100 000 counts in the GPC. Write this value in the log and compare it with that in table 7 below.

**Table 7**

Target	Approx. GPC integration time (min)
F	200
Na	106
Cl	10

10. Integrate 100 000 counts in the GPC. Set a ROI around the X-ray Peaks(s) and calculate the count rate in the detector and error. Note this value in the log. Save this data file under the name "GPCnn.SPM", where nn is the source name (eg: F, Na etc...). Note the file name and other details in the log. Only one GPC integration is needed per Soft X-ray line. Re-connect the GPC motor cable, withdraw the GPC from the beam and disconnect the motor cable.
11. The Soft X-ray beam illuminates a vertical strip on the SXR quadrant. Two APDs at a time can be placed in this beam. This is achieved by translating the cryostat horizontally by + or - 9 mm. Table 8, below, shows all combinations of rotator positions and horizontal translations.

**Table 8**

Rotator position	Horizontal translation	Illuminated diodes
"8 - 11"	+9 mm	8 & 11
"8 - 11"	-9 mm	9 & 10
"12 - 15"	-9 mm	14 & 15
"12 - 15"	+9 mm	12 & 13
"0 - 3"	+9 mm	0 & 3
"0 - 3"	-9 mm	1 & 2
"4 - 7"	-9 mm	6 & 7
"4 - 7"	+9 mm	4 & 5

12. Select the first quadrant to calibrate using the rotator on the rear of the cryostat. Translate the cryostat to select one diode pair. Select the corresponding data channels in the CATSAT calibration software using the buttons at the top of the screen.
13. Record a few hundred X-ray counts from the pair of APDs. Set a ROI around the X-ray Peak. Examine the output of each channel individually to confirm that they have approximately the same number of counts. Calculate the time that would be required to produce 100 000 counts in a single diode. Write this value in the log and compare it with that in table 9 below.

**Table 9**

Target	Approx. APD integration time (min)
F	29
Na	30
Cl	4

14. Integrate 100 000 counts in each of the illuminated APDs simultaneously. Save the data to an Excel file, filling in all of the required details in the software. File names should be simple and should reflect the panel being used, eg: "flight2file1.xls". Sheet names should be composed from the target being used and the channels being illuminated eg: "F 0 & 3". File names, sheet names, integration times etc... should all be noted in the log.

15. Translate the cryostat to illuminate the remaining pair of diodes in the current quadrant and select the corresponding data channels in software. Repeat step 14 for the new diode pair.
16. Use the rotator on the rear of the cryostat to illuminate the next quadrant of the panel.
17. Repeat steps 14 - 16 until data has been gathered from all eight diode pairs of the panel. Notice that while data from one pair is being recorded, data from the previous panel can be analysed. Analysis is performed in the same way as described earlier for Kevex data.
18. Turn off the HV for the GPC and close valve 3.

## Optical filter checks

The following procedure provides data to check the effectiveness of the Al light filters.

1. Turn on the software pulser and Enable all the sensor channels.
2. Record the pulser counts for 2 minutes.
3. Examine the spectra from each sensor channel in turn, noting pulser peak widths in the log.
4. Increase the software threshold to channel 100.
5. Turn on the LED power supply and increase the bias to 6.75 V.
6. Disable all sensor channels except those in the currently illuminated quadrant.
7. Record the pulser counts for 2 minutes.
8. Examine the spectra from each sensor channel in turn, noting pulser peak widths in the log. Disable all sensor channels
9. Use the rotator to change the illuminated quadrant. Enable the newly illuminated sensor channels.
10. Repeat steps 7 - 9 until all four quadrants have been examined.

Notice that the quadrant illuminated by the LED is not the same as the quadrant in the X-ray beam. Table 10 shows which diodes are in front of the LED for different rotator settings.

Table 10

Rotator Setting	APDs in front of LED
"8 - 11"	4 - 7
"12 - 15"	8 - 11
"0 - 3"	12 - 15
"4 - 7"	0 - 3

## Turning off the diodes

When testing is finished the High Voltage may be turned off using the control at the top of the main screen. The bench HV supply may then be reduced to 0 volts and then turned off. The Calibration software should be closed and then the power supply for the electronics chain should be switched off.